Geochemical Perspectives Letters

© 2019 The Authors
Published by the European Association of Geochemistry

Formation of Archean continental crust constrained by boron isotopes

M.A. Smit[1*], A. Scherstén[2], T. Næraa[2], R.B. Emo[1,3], E.E. Scherer[4], P. Sprung[5], W. Bleeker[6], K. Mezger[7], A. Maltese[7], Y. Cai[8], E.T. Rasbury[9], M.J. Whitehouse[10]

OPEN ACCESS

doi: 10.7185/geochemlet.1930

Abstract

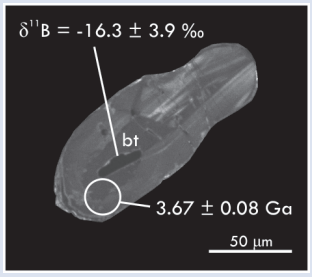

The continental crust grew and matured compositionally during the Palaeo- to Neoarchean through the addition of juvenile tonalite-trondhjemite-granodiorite (TTG) crust. This change has been linked to the start of global plate tectonics, following the general interpretation that TTGs represent ancient analogues of arc magmas. To test this, we analysed B concentrations and isotope compositions in 3.8-2.8 Ga TTGs from different Archean terranes. The $^{11}B/^{10}B$ values and B concentrations of the TTGs, and their correlation with Zr/Hf, indicate differentiation from a common B-poor mafic source that did not undergo addition of B from seawater or seawater-altered rocks. The TTGs thus do not resemble magmatic rocks from active margins, which clearly reflect such B addition to their source. The B- and ^{11}B-poor nature of TTGs indicates that modern style subduction may not have been a dominant process in the formation of juvenile continental crust before 2.8 Ga.

Received 11 June 2019 | Accepted 18 October 2019 | Published 14 November 2019

Introduction

Plate tectonics is a global process in which partially hydrated and dense oceanic lithosphere is recycled in long lived subduction zones. Although prevalent throughout the Phanerozoic, it is unclear whether, or to what extent, this process operated during the Archean (4.0-2.5 Ga) when mantle heat flow was higher, and the lithosphere was perhaps less differentiated (Brown, 2014; Kamber, 2015). Critical to this debate is the interpretation of tonalite-trondhjemite-granodiorite (TTG) complexes, which make up 90% of the preserved Archean juvenile continental crust (Martin *et al.*, 2005; Moyen and Martin, 2012). These low-K, high-Gd_N/Yb_N, I-type granitoids reflect melting of hydrous basaltic sources with residual hornblende and/or garnet (*e.g.*, Arth and Hanson, 1975; Rapp *et al.*, 1991). Interpretations regarding the geodynamic setting of TTG formation are diverse and numerous (Moyen and Martin, 2012). Several of these consider TTGs as slab melts from primitive flat slab subduction zones with a high geothermal gradient and no contribution from the mantle wedge (Smithies, 2000; Laurent *et al.*, 2014). Others models suggest that TTGs represent melts from thickened mafic crust produced during episodes of density-driven crustal overturning, delamination, underplating or plume activity (Smithies, 2000; Bédard, 2006; van Kranendonk *et al.*, 2007; Kamber, 2015; Johnson *et al.*, 2017). Stagnant lid models (*e.g.*, Debaille *et al.*, 2013) provide hybrids to these 'subduction' and 'intraplate' models (Moyen and Martin, 2012), involving plume-induced melting, as well as flux melting of the mantle during sporadic, local plate burial. Although the models differ at various levels of detail, they differ fundamentally regarding the nature of the mafic source: either it comprised deeply subducted crustal material from the Earth's surface, or it represented the lower and never-before-surfaced sections of a thickened or underplated crust.

Zircon Hf and O isotope data suggest that Archean juvenile continental crust formed by melting of enriched mafic crust extracted from a still primitive mantle, and that sediment recycling and crustal thickening occurred since the Mesoarchean (*e.g.*, Kemp *et al.*, 2010; Næraa *et al.*, 2012; Reimink *et al.*, 2016; Roberts and Santosh, 2018). The same is indicated by Si-O isotope data for Archean detrital zircon (Trail *et al.*, 2018).

1. Department of Earth, Ocean and Atmospheric Sciences, University of British Columbia, 2020-2207 Main Mall, Vancouver V6T 1Z4, Canada
2. Department of Geology, Lund University, Sölvegatan 12, SE- 223 62 Lund, Sweden
3. Department of Earth, Environmental and Biological Sciences, Queensland University of Technology, 2 George Street, Brisbane QLD4000, Australia
4. Institut für Mineralogie, Westfälische Wilhelms-Universität, Corrensstraße 24, D-48149 Münster, Germany
5. Paul Scherrer Institut, Forschungsstrasse 111, CH-5232 Villigen, Switzerland
6. Geological Survey of Canada, 601 Booth Street, Ottawa K1A 0E8, Canada
7. Institut für Geologie, Baltzerstrasse 1+3, CH-3012 Bern, Switzerland
8. Lamont-Doherty Earth Observatory, Columbia University, 61 Route 9W, Palisades, NY 10964, USA
9. Department of Geosciences, 255 Earth and Space Sciences Building, Stony Brook University, Stony Brook, NY 11794-2100, USA
10. Department of Geosciences, Swedish Museum of Natural History, Box 50007, SE-104 05 Stockholm, Sweden
* Corresponding author (email: msmit@eoas.ubc.ca)

These interpretations fit the observation that high $^{18}O/^{16}O$ granitoids produced by melting of surface-altered rocks are restricted to post-Archean time when recycling of such material, possibly by subduction, became prevalent (Valley *et al.*, 2005). Some Archean TTGs show elevated $^{30}Si/^{28}Si$ and $^{18}O/^{16}O$ values, which were interpreted to indicate chert and, by inference, subducted sediments in the source (Deng *et al.*, 2019). The integral Si-O isotope record of Hadean zircon and Archean TTGs indicates source contributions from a variety of supra-crustal rocks, including chemical sediments, serpentinised and silicified basalts (Trail *et al.*, 2018; André *et al.*, 2019). Whether anatexis of such material requires deep burial by subduction is unclear. Moreover, Si and O may not both represent the source and its components. The elevated $^{18}O/^{16}O$ values that — together with elevated $^{30}Si/^{28}Si$ values — were taken to represent the chert component actually partly exceed those typically observed for Archean TTGs; these could reflect secondary ^{18}O-enrichment *via* low temperature alteration (Valley *et al.*, 2005). The Sr anomalies (Sr/Sr*) of the analysed TTGs correlate strongly inversely with $^{18}O/^{16}O$ and may thus likewise be disturbed. Strikingly, the compositions of the samples with highest Sr/Sr* values match those modelled for low degree garnet-stable partial melting of a tholeiitic source that is *not* contaminated by chert or other components (Deng *et al.*, 2019). Although Si-O data provide a unique opportunity to discern supra-crustal contributions to TTG sources (Trail *et al.*, 2018), their interpretation to discern the geodynamic setting of TTG formation is still controversial.

Boron analysis provides an alternative approach to characterising the TTG source. The global B cycle and B isotope systematics are well characterised and appear uniform across geologic time (Supplementary Information, Introduction 1). Most importantly, seawater shows a very strong long term enrichment in the heavy isotope ^{11}B, which is reflected in the B chemistry of subducted slabs and magmatic rocks from active margins (Ryan and Chauvel, 2014; de Hoog and Savov, 2018). The latter is because B is partitioned into melts or fluids that are expelled from the subducting slab and feed the arc source. Due to the enrichment of B and ^{11}B in their source, most magmatic rocks from active margins — including adakites and modern I-type granitoids from continental arcs (Fig. 2) — typically exhibit higher $\delta^{11}B$ values than the average continental crust ($\delta^{11}B$ = -9.4 ± 0.4‰), or mid-oceanic ridge basalts (MORB) and the depleted MORB mantle (DMM; $\delta^{11}B$ = -7.1 ± 0.9‰; Marschall *et al.*, 2017; Marschall, 2018; $\delta^{11}B = 1000 \times [(^{11}B/^{10}B)_{sample}/(^{11}B/^{10}B)_{SRM\text{-}951} - 1]$). Only in rare situations of very steep or very hot subduction do magmatic rocks occasionally include $\delta^{11}B$ values that are similar to, or even lower than, that of DMM. Intense dehydration in these locations cause slab B budgets to be so low that the B signature of the arc source becomes dominated by melting of the mantle wedge (*e.g.*, de Hoog and Savov, 2018).

The B Signature of Archean TTGs

Boron concentrations and isotope compositions were determined for: 1) 3.78 Ga tonalite gneisses from the Isua Greenstone Belt, West Greenland; 2) ≥3.6 Ga tonalite and trondhjemite gneisses from the Acasta Gneiss; 3) 3.58 Ga tonalite gneisses from the Bastar Craton, India; 4) 2.87-2.79 Ga tonalite and trondhjemite gneisses from the Tartôq Greenstone Belt in Southwest Greenland. Whole rock materials were analysed, except for the Acasta TTG samples, which are poly-metamorphosed and exhibit altered matrices. To investigate the initial B composition of these rocks, *in situ* B analysis was done on pristine biotite inclusions inside igneous zircon (rationale in Supplementary Information, Introduction 2; geological descriptions in Supplementary Information, Introduction 3).

The samples show a range of trace element compositions (Table S-7) and comprise low and high Gd_N/Yb_N TTGs (Acasta, Tartôq), or high Gd_N/Yb_N TTGs only (Isua, Bastar; Fig. 1). Boron concentrations are 1.2-3.4 ppm — similar to those observed in other pristine Archean TTGs (Supplementary Information, Introduction 1). The B concentration correlates with Zr/Hf (R^2 = 0.82; Fig. 2a), but not with B/Nb, B/La, B/Zr, Gd_N/Yb_N or Nb/Ta. The $\delta^{11}B$ values of bulk TTG are -15.2 to -2.5‰ (Fig. 3, Table S-5). The $\delta^{11}B$ values correlate negatively with B concentration (R^2 = 0.73; Fig. 2a) and Zr/Hf (R^2 = 0.75; Fig. 2b). The meta-tonalite sample 508281 shows a similar B concentration as pristine samples, yet yielded $\delta^{11}B$ values that are at least 5‰ higher. The $\delta^{11}B$ values of biotite inclusions in Acasta zircon are -5.4‰ or lower, indicating negative $\delta^{11}B$ values for the protolith, even when assuming the largest biotite-melt fractionation factor (Supplementary

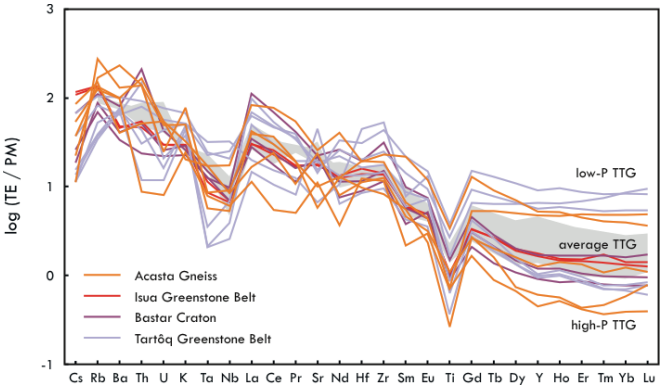

Figure 1 Trace element concentrations for the TTG samples and average TTG (Moyen and Martin, 2012). All data are normalised to primitive mantle (PM; data in Table S-7).

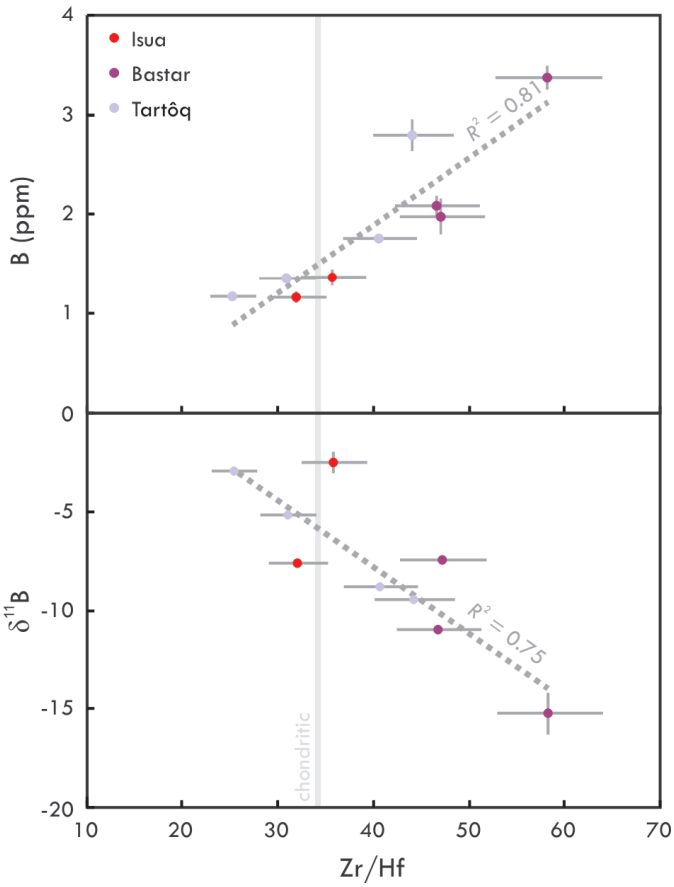

Figure 2 **(a)** B and **(b)** $\delta^{11}B$ versus Zr/Hf with the correlation coefficients for the given regressions.

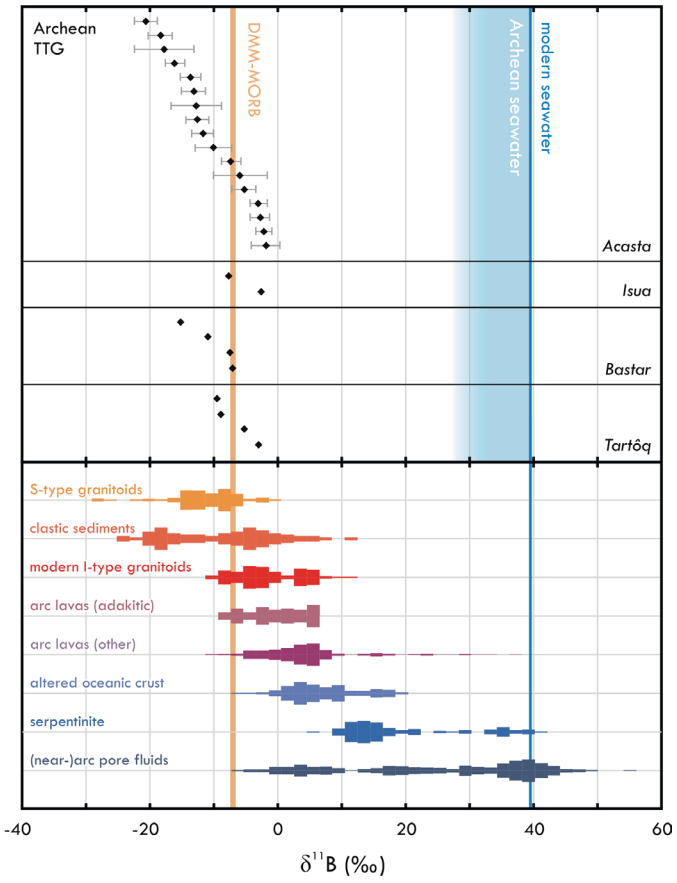

Figure 3 Boron isotope data for the analysed samples and terrestrial reservoirs (histograms). Error bars for whole rock analyses are smaller than the symbols. Acasta data represents bulk rock $\delta^{11}B$ modelled from biotite data (Supplementary Information, Analytical Methods and Data). The values for reference reservoirs are in Table S-1.

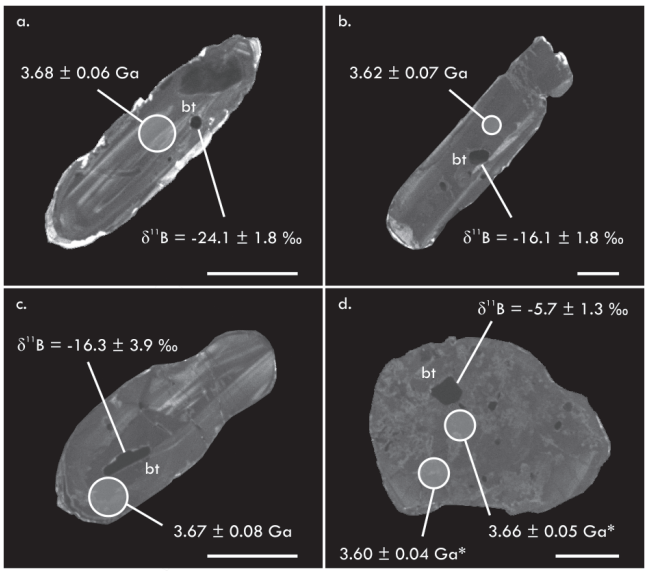

Figure 4 Cathodoluminescence images of zircon from the Acasta Gneiss Complex samples showing analysed biotite inclusions. The $\delta^{11}B$ values of biotite (in‰) and the $^{207}Pb/^{206}Pb$ age of the surrounding zircon (minimum inclusion age) are shown. Analytical spots are to scale; asterisk marks >10% discordance; scale bars are 50 µm. Data are in Table S-9.

Information, Analytical Methods and Data). The lowest values among this range were obtained from pristine zircon domains (Fig. 4a-c), whereas values above -10‰ were obtained for inclusions from zircon with disturbed U-Pb systematics and signs of alteration. The latter inclusions resemble biotite in the altered matrix in terms of B (Fig. 4d, Table S-5). The dispersion in biotite $\delta^{11}B$ values for single samples may thus reflect late fluid-rock interaction. The dispersion in biotite $\delta^{11}B$ values for single samples may thus reflect late fluid-rock interaction and the high values among the $\delta^{11}B$ range may represent ^{11}B enrichment from this process.

Discussion

Changes in the Zr/Hf value of tonalitic melt typically result from the crystallisation of ferromagnesian minerals (Linnen and Keppler, 2002) — biotite + amphibole ± plagioclase in this case, with or without garnet (Supplementary Information, Discussion) — which likewise would enrich the melt in highly incompatible B. The effects of such magmatic differentiation are clearly reflected in the B-Zr/Hf correlation (Fig. 2a). At chondritic Zr/Hf, TTGs are predicted to have 1-2 ppm B and a $\delta^{11}B$ value of *ca.* -7‰, which resembles melts from the DMM (1.2-1.3 ppm, -7.1 ± 0.9‰; Marschall *et al.*, 2017). The $\delta^{11}B$-Zr/Hf correlation may be linked to this through the role of H_2O. Crystallisation of basaltic and andesitic magmas is associated with the exsolution of H_2O and other volatiles (Sisson and Layne, 1993). Aqueous fluids in equilibrium with silicate melt preferentially incorporate ^{11}B, such that the more fractionated and hydrous magmas are, the lower $\delta^{11}B$ values of the crystallising magmas become (Hervig *et al.*, 2002). The B-Zr/Hf correlation in TTGs from different terranes and with different composition (Fig. 2) shows that their mafic sources — both garnet-present and garnet-absent—had a similar initial B-$\delta^{11}B$-Zr/Hf signature, and evolved without the addition of externally derived B.

The low B concentrations and $\delta^{11}B$ values, and their correlation with Zr/Hf, identify Archean TTGs as the differentiated magmatic products of a common mafic source that contained no detectable B from seawater or seawater-altered rocks. The TTGs differ from modern I-type granitoids from active margins; these are variably enriched in B and ^{11}B, independent of the degree of crystal fractionation (de Hoog and Savov, 2018), and do not show fractionation down to the low $\delta^{11}B$ values observed here (Fig. 2). As the relevant B reservoirs appear uniform through time (Supplementary Information, Introduction 1), such a signature would be expected for any Archean arc as well — possibly even more so, considering that a contribution from the mantle wedge appears lacking (Martin *et al.*, 2005). A subduction origin for TTGs cannot be *a priori* excluded. However, this would require that slabs were dehydrated such that they lost all B from seawater-altered materials prior to melting. Such dehydration is not seen even in the warmest of modern arcs and appears inconsistent with the hydrous nature of the TTG source (Moyen and Martin, 2012). More importantly, high geothermal gradients during the Archean would favour slab melting over slab dehydration (Martin, 1986; Moyen and Martin, 2012), indicating that B and H_2O would have been expelled from slabs concomitantly, not sequentially. This considered, the data appear more consistent with the TTG formation *via* 'intraplate' processes (Moyen and Martin, 2012) — *e.g.*, crustal thickening, volcanic resurfacing, overturning, delamination, and stagnant lid or 'squishy lid' tectonics (Bédard, 2006; van Kranendonk *et al.*, 2007; Hoffmann *et al.*, 2011; Debaille *et al.*, 2013; Kamber, 2015; Johnson *et al.*, 2017; Rozel *et al.*, 2017) — in which deep hydrated mafic crust with a DMM-like $\delta^{11}B$ value melted under the influence of a high or unstable geotherm. The absence of an elevated

$\delta^{11}B$ signature from any supracrustal rocks, which Si-O data indicate were present in the source (André *et al*., 2019; Deng *et al*., 2019), could signify B loss from these rocks during residence at depth on timescales that far exceed that of subduction. With subduction processes not clearly reflected in the B data, it would appear that these did not contribute substantially to Archean juvenile crustal growth before 2.8 Ga. If Archean juvenile crustal growth and the start of modern style plate tectonics are at all related, it would appear that the former was the cause, rather than the consequence, of the latter.

Acknowledgements

We thank G.E. Harlow, C. Martin and T. Zack for providing reference materials, and K. Lindén (NRM), L. Kato and V. Lai (UBC) for technical support. The manuscript substantially benefited from constructive reviews by R. Halama and one anonymous reviewer, and by C.J. Hawkesworth, M. Brown, B. Kamber, and H.R. Marschall on a previous version. We thank M. Boyet for editorial handling. This is contribution #619 of the NordSIMS facility, a Swedish-Icelandic research infrastructure. The research was supported by NSERC (Discovery Grant RGPIN-2015-04080 to MAS), CFI and BC-KDF (Grant 229814 to MAS), NSF (MRI Grant EAR-0959524 to ETR), and VR (Grant 2014-06375). KM and AM acknowledge support through SNF (Grant 17452).

Additional Information

Supplementary Information accompanies this letter at http://www.geochemicalperspectivesletters.org/article1930.

This work is distributed under the Creative Commons Attribution Non-Commercial No-Derivatives 4.0 License, which permits unrestricted distribution provided the original author and source are credited. The material may not be adapted (remixed, transformed or built upon) or used for commercial purposes without written permission from the author. Additional information is available at http://www.geochemicalperspectivesletters.org/copyright-and-permissions.

Cite this letter as: Smit, M.A., Scherstén, A., Næraa, T., Emo, R.B., Scherer, E.E., Sprung, P., Bleeker, W., Mezger, K., Maltese, A., Cai, Y., Rasbury, E.T., Whitehouse, M.J. (2019) Formation of Archean continental crust constrained by boron isotopes. *Geochem. Persp. Let.* 12, 23-26.

References

André, L., Abraham, K., Hofmann, A., Monin, L., Kleinhanns, I.C., Foley, S. (2019) Early continental crust generated by reworking of basalts variably silicified by seawater. *Nature Geoscience* 12, 769-773.

Arth, J.G., Hanson, G.N. (1975) Geochemistry and origin of the early Precambrian crust of northeastern Minnesota. *Geochimica et Cosmochimica Acta* 39, 325-362.

Bédard, J.H. (2006) A catalytic delamination-driven model for coupled genesis of Archaean crust and sub-continental lithospheric mantle. *Geochimica et Cosmochimica Acta* 70, 1188-1214.

Brown, M. (2014) The contribution of metamorphic petrology to understanding lithosphere evolution and geodynamics. *Geoscience Frontiers* 5, 553-569.

Debaille, V., O'Neill, C., Brandon, A.D., Naenecour, P., Yin, Q.-Z., Matielli, N., Treiman, A.H. (2013) Stagnant-lid tectonics in early Earth revealed by ^{142}Nd variations in late Archean rocks. *Earth and Planetary Science Letters* 373, 83-92.

de Hoog, J.C.M., Savov, I.P. (2018) Boron isotopes as a tracer of subduction zone processes. In: Marschall, H.R., Foster, G.L. (Eds.) *Boron Isotopes – The Fifth Element, Advances in Isotope Geochemistry 6*. Springer, Heidelberg, 217-247.

Deng, Z., Chaussidon, M., Guitreau, M., Puchtel, I.S., Dauphas, N., Moynier, F. (2019) An oceanic subduction origin for Archaean granitoids revealed by silicon isotopes. *Nature Geoscience* 12, 774-778.

Hervig, R.L., Moore, G.M., Williams, L.B., Peacock, S.M., Holloway, J.R., Roggensack, K., (2002) Isotopic and elemental partitioning of boron between hydrous fluid and silicate melt. *American Mineralogist* 87, 769-774.

Hoffmann, J.E., Münker, C., Næraa, T., Rosing, M.T., Herwartz, D., Garbe-Schönberg, D., Svahnberg, S. (2011) Mechanisms of Archean crust formation inferred from high-precision HFSE systematics in TTGs. *Geochimica et Cosmochimica Acta* 75, 4157-4178.

Johnson, T.E., Brown, M., Gardiner, N.J., Kirkland, C.L., Smithies, R.H. (2017) Earth's first stable continents did not form by subduction. *Nature* 543, 239-242.

Kamber, B.S. (2015) The evolving nature of terrestrial crust from the Hadean, through the Archaean, into the Proterozoic. *Precambrian Research* 258, 48-82.

Kemp, A.I.S., Wilde, S.A., Hawkesworth, C.J., Coath, C.D., Nemchin, A.A., Pidgeon, R.T., Vervoort, J.D., DuFrane, S.A. (2010) Hadean crustal evolution revisited: New constraints from Pb–Hf isotope systematics of the Jack Hills zircons. *Earth and Planetary Science Letters* 296, 45-56.

Laurent, O., Martin, H., Moyen, J.-F., Doucelance, R. (2014) The diversity and evolution of late-Archean granitoids: Evidence for the onset of "modern-style" plate tectonics between 3.0 and 2.5 Ga. *Lithos* 205, 208-235.

Linnen, R.L., Keppler, H. (2002) Melt composition control of Zr/Hf fractionation in magmatic processes. *Geochimica et Cosmochimica Acta* 66, 3293-3301.

Marschall, H.R., Wanless, V.D., Shimizu, N., Pogge von Strandmann, P.A.E., Elliott, T., Monteleone, B.D. (2017) The boron and lithium isotopic composition of mid-ocean ridge basalts and the mantle. *Geochimica et Cosmochimica Acta* 207, 102–138.

Marschall, H.R. (2018) Boron isotopes in the ocean floor realm and the mantle. In: Marschall, H.R., Foster, G.L. (Eds.) *Boron Isotopes – The Fifth Element, Advances in Isotope Geochemistry 6*. Springer, Heidelberg, 189-215.

Martin, H. (1986) Effect of steeper Archean geothermal gradient on geochemistry of subduction zone magmas. *Geology* 14, 753–756,

Martin, H., Smithies, R.H., Rapp, R.P., Moyen, J.-F., Champion, D. (2005) An overview of adakite, tonalite trondhjemite granodiorite (TTG), and sanukitoid: relationships and some implications for crustal evolution. *Lithos* 79, 1-24.

Moyen, J.-F., Martin, H. (2012) Forty years of TTG research. *Lithos* 148, 312-336.

Næraa, T., Scherstén, A., Rosing, M.T., Kemp, A.I.S., Hoffmann, J.E., Kokfelt, T.F., Whitehouse, M.J. (2012) Hafnium isotope evidence for a transition in the dynamics of continental growth 3.2 Gyr ago. *Nature* 485, 627-630.

Rapp, R.P., Watson, E.B., Miller, C. (1991) Partial melting of amphibolite/eclogite and the origin of Archean trondhjemites and tonalities. *Precambrian Research* 51, 1-25.

Reimink, J.R., Davies, J.H.F.L., Chacko, T., Stern, R.A., Heaman, L.M., Sarkar, C., Schaltegger, U., Creaser, R.A., Pearson, D.G. (2016) No evidence for Hadean continental crust within Earth's oldest evolved rock unit. *Nature Geoscience* 9, 777-780.

Roberts, N.M.W., Santosh, M. (2018) Capturing the Mesoarchean emergence of continental Crust in the Coorg Block, Southern India. *Geophysical Research Letters* 45, 7444-7453.

Rozel, A.B., Golabek, G.J., Jain, C., Tackley, P.J., Gerya, T. (2017) Continental crust formation on early Earth controlled by intrusive magmatism. *Nature* 545, 332-335.

Ryan, J.G., Chauvel, C. (2014) The subduction-zone filter and the impact of recycled materials on the evolution of the mantle. In: Holland, H.D., Turekian, K.K. (Eds.) *Treatise on Geochemistry 3: The Mantle and Core*. Elsevier, Amsterdam, 479-508.

Sisson, T.W., Layne, G.D. (1993) H_2O in basalt and basaltic andesite glass inclusions from four subduction-related volcanoes. *Earth and Planetary Science Letters* 117, 619-635.

Smithies, R.H. (2000) The Archaean tonalite–trondhjemite–granodiorite (TTG) series is not an analogue of Cenozoic adakite. *Earth and Planetary Science Letters* 182, 115-125.

Trail, D., Boehnke, P., Savage, P., Liu, M.-C., Miller, M.L., Bindeman, I. (2018) Origin and significance of Si and O isotope heterogeneities in Phanerozoic, Archean, and Hadean zircon. *Proceedings of the National Academy of Sciences* 115, 10287-10292.

Valley, J.W., Lackey, J.S., Cavosie, A.J., Clechenko, C.C., Spicuzza, M.J., Basei, M.A.S., Bindeman, I.N., Ferreira, V.P., Sial, A.N., King, E.M., Peck, W.H., Sinha, A.K., Wei, C.S. (2005) 4.4 billion years of crustal maturation: oxygen isotope ratios of magmatic zircon. *Contributions to Mineralogy and Petrology* 150, 561-580.

van Kranendonk, M.J., Smithies, R.H., Hickman, A.H., Champion, D.C. (2007) Secular tectonic evolution of Archean continental crust: interplay between horizontal and vertical processes in the formation of the Pilbara Craton, Australia. *Terra Nova* 19, 1-38.

Geochemical Perspectives Letters

© 2019 The Authors
Published by the European Association of Geochemistry

Formation of Archean continental crust constrained by boron isotopes

M.A. Smit, A. Scherstén, T. Næraa, R.B. Emo, E.E. Scherer, P. Sprung, W. Bleeker, K. Mezger, A. Maltese, Y. Cai, E.T. Rasbury, M.J. Whitehouse

Supplementary Information

The Supplementary Information includes:

- Supplementary Introduction 1 to 3
- Supplementary Analytical Methods and Data
- Supplementary Discussion
- Figures S-1 to S-7
- Tables S-1 to S-9
- Supplementary Information References

Supplementary Introduction 1: B systematics of modern reservoirs and Archean TTGs

The modern global B cycle

Boron is highly incompatible in silicate melts and is relatively fluid-mobile compared to other elements with similar incompatibility (*e.g.*, Nb, Pr). Elemental ratios of B over such elements are hence 'fluid indicators' that are commonly used to discern fluid additions to magmatic sources particularly in island arc settings (*e.g.*, Ryan and Langmuir, 1993; Mohan *et al.*, 2008). Boron isotopes undergo equilibrium fractionation during fluid-melt and fluid-rock interaction. In both cases, the heavy ^{11}B isotope is preferentially incorporated into the fluid phase (Hervig *et al.*, 2002). Exsolution of a fluid from silicate melts, and interaction between these phases, may leave the melt depleted in ^{11}B. In addition, B in silicate melts appears to prefer ^{10}B, possibly due to its tetrahedral coordination. These effects may cause a deviation of a few per mill between the $\delta^{11}B$ values of melt and the minerals that crystallise from this melt during cooling and fluid exsolution (Hervig *et al.*, 2002). At sub-solidus conditions, equilibrium isotope fractionation between fluids and solids, such as tourmaline, micas and clay minerals, is much stronger. As a result of these elemental and isotope fractionation effects, there are differences in the characteristic B signature of major terrestrial reservoirs (Fig. S-1). Although there is substantial overlap between these reservoirs, there are distinct differences between magmatic sources that have been fluxed by exotic 11B enriched fluids, *e.g.*, surface waters or highly fractionated metamorphic fluids, versus sources that have not. This allows the B system to provide a useful tracer for distinguishing between sources components in specific magmatic systems (*e.g.*, Marschall *et al.*, 2017; Marschall, 2018). A brief summary of the B characteristics of important terrestrial reservoirs, based on major reviews on global B systematics (*e.g.*, Marschall, 2018; Trumbull & Slack, 2018; de Hoog and Savov, 2018), is provided below.

Boron in seawater has a residence time of about 20 million years and is isotopically very heavy (+39.5 ± 0.1 ‰; Marschall, 2018). The high $\delta^{11}B$ value reflects the heavy isotope composition of continental run-off as well as the equilibrium fractionation of B isotopes during seafloor weathering and hydrothermal alteration. Seawater appears to have been uniformly enriched in ^{11}B throughout geologic time. Estimates of the $\delta^{11}B$ value of Archean seawater are highly uncertain, yet are all identical to the modern-day value

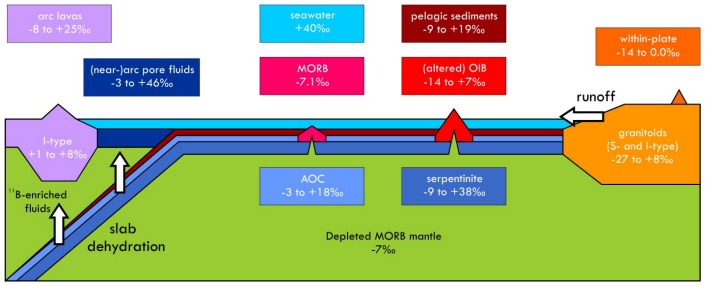

Figure S-1 Schematic representation of the B isotope signatures (in $\delta^{11}B$) of various terrestrial reservoirs. Data provided In Table S-1.

within their large uncertainty (Marschall, 2018). Their mean values are generally slightly lower, but this could be because the data are subject to downward-skewing from sample bias (de Hoog and Savov, 2018) and may represent transient states, or local oceanic basins rather than the global ocean (de Hoog and Savov, 2018). Although data are still very limited, Archean chert from the Pilbara (*c.* 3.5 Ga) exhibits B concentrations that are similar to those of modern chert, which would indicate that B concentrations in Archean seawater were at least similar to that of today (Lemarchand *et al.*, 2009).

The depleted mid-ocean ridge basalt (MORB) typically show B concentrations of 1.2-1.3 ppm and $\delta^{11}B$ values identical to depleted MORB mantle (DMM; −7.1 ± 0.9 ‰, Marschall *et al.*, 2017). Similar values are observed in ocean-island basalts (OIB), which show dispersion due to shallow assimilation of the magmas during ascent (Marschall, 2018) and possible interaction with seawater. Archean basalts and komatiites exhibit $\delta^{11}B$ values that are indistinguishable from those of present-day MORB-DMM (Sobolev *et al.*, 2016), indicating that the B isotope signature of MORB-DMM has been uniform throughout geologic time. Relative to pristine DMM, the serpentinised oceanic mantle is rich in B (10-100 ppm) and exhibits $\delta^{11}B$ values as high as that of seawater (Marschall, 2018). Pelagic clay, chert and carbonate sediments are likewise enriched in B (49-163 ppm) and ^{11}B (-9 to +19 ‰; Marschall, 2018). The $\delta^{11}B$ value are generally substantially higher than those of terrigenous sediments in which clastic material from the continental crust dominates the B budget (-24 to +6 ‰; Table S-1). In aggregate, the altered oceanic lithosphere is reservoir rich in B and ^{11}B due to the long-term interaction with seawater.

The bulk continental crust is strongly B-enriched compared to DMM (11 ppm on average; Marschall *et al.*, 2017) and is chemically stratified, with the upper continental crust (UCC) having high concentrations (43 ppm; Kasemann *et al.*, 2000) and the refractory lower continental crust (LCC) being mostly B-depleted (2 ± 1 ppm; Leeman *et al.*, 1992). The bulk continental crust (BCC) is isotopically slightly lighter than DMM (-9.4 ± 0.4 ‰; Marschall *et al.*, 2017), possibly due to long-term weathering and formation of

Table S-1 Boron isotope database. I-type granite data from Trumbull and Slack (2018). Data for other reservoirs is provided separately. *D* and P_{50} are the Kolmogorov-Smirnov statistic and overlap factor, respectively (Eqs. 3 and 4). *A full version of the boron isotope database can be downloaded from* https://www.geochemicalperspectivesletters.org/documents/GPL1930_TS-1.xlsx

Reservoir	Count	Population description (outlier-filtered; 2σ)					Comparison between TTG and *x*	
		Min	Q_1	Q_2	Q_3	Max	*D*	P_{50}
Altered Oceanic Crust	118	-2.5	2.6	5.5	9.9	17.5	0.97	-0.95
Arc lavas (adakite)	36	-8.2	-2.6	0.6	3.8	5.9	0.86	-0.41
Arc lavas (other)	372	-7.3	-0.6	3.4	5.7	23.5	0.69	-0.61
Clastic sediments	64	-23.8	-17.6	-7.8	-3.4	6.7	0.32	1.00
Metamorphosed sediments	112	-16.5	-11.3	-7.2	-3.8	4.0	0.27	0.50
Pegmatite-aplite	94	-19.1	-13.7	-11.7	-9.8	-4.9	0.34	0.40
A-type granite	32	-23.2	-14.3	-12.9	-7.9	20.9	0.28	0.67
I-type granite	80	-9.9	-4.3	-2.8	4.1	10.5	0.55	0.25
S-type granite	312	-26.5	-14.8	-11.8	-8.5	-2.5	0.55	0.66
Granitic rocks (general)	438	-26.0	-14.6	-11.8	-8.7	-2.1	0.24	0.61
(Near-)arc pore fluids	317	-2.5	12.0	28.7	38.2	45.5	0.25	-1.93
Meteorite	32	-8.1	-5.1	-2.5	2.8	12.9	0.97	-0.15
MORB	31	-8.1	-5.7	-4.5	-1.3	7.3	0.70	-0.08
Ocean island basalt	144	-14.0	-7.5	-4.3	-3.1	6.5	0.61	0.10
Serpentite (pristine)	101	9.1	12.1	14.7	26.0	39.3	0.53	-1.94
Serpentite (subducted)	108	-11.6	-3.4	10.7	20.6	28.0	1.00	-0.33
Within-plate basalt (continental)	73	-13.85	-7.30	-5.01	-3.53	0.00	-8.37	-5.93

^{11}B-poor clay minerals in the terrestrial environment. A specific estimate of the δ^{11}B value of the refractory lower crust is not available. Still, because isotope fractionation during the melting of the deep crust is largely insignificant (Trumbull and Slack 2018), it is to be expected that the average δ^{11}B value of the LCC is similar if not equal to that of the BCC (-9.4 ± 0.4 ‰; Marschall *et al.*, 2017). Boron isotope compositions differ slightly yet consistently between different types of granites. I-type granites, which represent juvenile magmas produced in continental arcs and Cordilleran-type active margins, are isotopically heavy (-10 to +12 ‰; Trumbull and Slack, 2018). In contrast, S-type granites and pegmatitic rocks produced by partial melting of continental rocks rich in clay minerals and mica are generally isotopically light (-27 to -3 ‰; Table S-1; Trumbull and Slack, 2018). Isotope fractionation during the melting to produce these rocks is not substantial; the differences in isotope values of these various granitoids largely reflect the differences in the signatures of their sources (Trumbull and Slack 2018). The consistent and resolvable differences between S- and I-type granites demonstrate the ability of B isotope analysis to discriminate between granitoids rocks formed in active margins and those produced by melting of evolved crust away from such margins.

The B systematics of subduction zones and arc magmas

The B chemistry of arc magmas and subducting slabs in intrinsically linked through the mass flux that is generated by the slab as dehydrates and melts. A detailed and comprehensive review of the B chemistry of slabs at various stages of subduction and arc magmas, in all their natural variety, is provided by de Hoog and Savov (2018). A brief summary of the B characteristics of arcs is provided here to delineate similarities and differences relative to other crustal rock reservoirs. Arc lavas are typically strongly B enriched and show high B/Nb, B/La and B/Zr values as a result the addition of B-rich slab-derived fluids to the magmatic source (Ryan and Langmuir, 1993). The δ^{11}B values of arc lavas are typically positive and thus substantially higher than those observed for granitoids, regardless of their type. The B- and ^{11}B-rich signatures seen in most arcs reflect the influence of the altered oceanic lithosphere (both crust and mantle; *e.g.*, Konrad-Schmolke and Halama, 2014; Konrad-Schmolke *et al.*, 2016) or the serpentinised mantle wedge (*e.g.*, Tonarini *et al.*, 2011). Slab-derived fluids tap from B- and ^{11}B-enriched oceanic lithologies within the slab and are additionally enriched in these species as a result of the equilibrium chemical and isotope fractionation that occurs during dehydration (*e.g.*, Konrad-Schmolke and Halama, 2014; de Hoog and Savov, 2018).

The large majority of arc lavas has δ^{11}B values of 0 ‰ or higher. Still, negative values are also observed. The δ^{11}B values in arc lavas decrease with increasing arc-trench distance and decreasing slab dip, independent of sub-arc slab depth or slab thermal structure. Both parameters are associated with increasing slab dehydration, which deprives the slabs of B. Slab residua are less ^{11}B enriched due to dehydration. This effect may not be apparent for sediments, for which unmetamorphosed and highly metamorphosed and dehydrated equivalents yield a similar range in δ^{11}B values (Table S-1). For serpentinites, this effect is nevertheless very clear. Subducted serpentinites show a much larger range in δ^{11}B values and include much lower δ^{11}B values than are observed among serpentinite samples taken from the ocean floor (Fig. 4; Table S-1). This effect could contribute to the lowering in δ^{11}B values with increasing subduction. Still, the vast majority of magmatic rocks from active margins have δ^{11}B values above that of DMM, which indicates that dehydrated slab residua are too B-poor to significantly influence the δ^{11}B signature of any fluids that the slab may generate. Only in extreme cases are δ^{11}B values of lavas only moderately elevated above MORB-DMM values. Examples are found in continental arcs where sub-arc slab temperatures are high: 1) 'hot' subduction zones such as Central Cascadia, where the slab is very young (<20 Myr old), thin and dehydrated early (-9.2 to -1.4 ‰); 2) arc termination points where slabs are enveloped in hot asthenosphere (*e.g.*, North Kamchatka: -3.7 to +5.9 ‰), and 3) some cases of very steep subduction, such as that reflected by arc-related dykes in the Permian Beishan Orogen (-7.7 to -4.4 ‰; values in Table S-1). The δ^{11}B values of rocks in these settings are similar to those of I-type granites (Fig. 3). This is consistent with the general interpretation of such granites as continental arc intrusives.

The only arc-related materials that yielded δ^{11}B values below -10 ‰ are primitive ultramafic melt inclusions found in olivine from primitive basaltic andesites at Mt. Shasta, northern California (-21.6 to -0.9 ‰, Rose *et al.*, 2001). Two of the 9 analysed inclusions yielded δ^{11}B values below -10 ‰—true outliers, even among Shasta andesites (Le Voyer *et al.*, 2010). The B concentrations of these inclusions (*c.* 1 ppm) are likewise anomalously low for arc lavas. The only Cascade lavas that were found to be that poor in B are lavas from the back-arc region in southern Washington, where slab-derived contributions are minimised and δ^{11}B values approach that of DMM (-7 to -9 ‰, *e.g.*, Leeman *et al.*, 2004). The low δ^{11}B values and B concentrations of the primitive Shasta melt inclusions were interpreted to reflect contributions from slab remnants that were almost entirely dehydrated and, as a result, extremely depleted in B and ^{11}B. The Cl/F values of these inclusions are consistent with this component being sediment-derived (Le Voyer *et al.*, 2010). It is important to note that, with H_2O concentrations up to 8 wt %, the Shasta basaltic andesites are unusually hydrous (Grove *et al.*, 2002). The melt inclusions actually show an even higher concentration of fluid-mobile elements than the host andesite, indicating that the parental melt may have been even more hydrous than the latter. Ultimately these signatures are ascribed to a mixture between hydrous fluids and silicate melts that hybridised in the mantle and caused flux melting just below the continental Moho to produce the melt captured by the inclusions (Grove *et al.*, 2002). This model explains most observations for these rocks. However, fitting the B data into this model is difficult if these are considered to reflect primary source compositions. The extremely

fractionated slab fragments that are argued to have caused the low $\delta^{11}B$ values of the melt would need to have been thoroughly dehydrated for such values to occur (Rose *et al.*, 2001); melting would need to be required for the B of these fragments to become mobilised. The large amount of aqueous fluids in the system would need to have been derived elsewhere—specifically from a source that was still very rich in H_2O and, by extension, not fractionated in terms of B isotope composition. These fluids would be required not to have contributed substantially to the B budget of the melt inclusions, as the slab fragments would then be required to have had $\delta^{11}B$ values lower than that of even the most fractionated of sediments observed on Earth. The fluids nevertheless contain at least twice as much B as the melt inclusions (2-3 ppm; Le Voyer *et al.*, 2010), which makes this scenario implausible. To further complicate this model, major element compositions of the andesites do not reflect a component of melting from slab material, refractory or otherwise (Rose *et al.*, 2001; Grove *et al.*, 2002).

The primitive mantle-derived andesites at Mt. Shasta clearly provide a case that, in terms of B systematics, is exceptional and not yet fully explained. Two alternative possibilities can be provided to explain the data, both of which are not yet considered in the literature. Firstly, it is important to note that Mt. Shasta represents an unusual location in Cascadia; it lies in the direct path of the subducting Bianco Fault Zone, which separates the Juan de Fuca and Gorda Plates. It could be conceivable that, fluids that are produced late in these slabs and would, in normal cases, remain slab-bound, are able to escape to the mantle source via this zone of weakness. This may particularly apply to serpentinites, which warm up later (*e.g.*, Syracuse *et al.*, 2010; Walowski *et al.*, 2015) and are known to locally develop negative $\delta^{11}B$ values at such advanced stage of subduction (-12 to + 15 ‰; Martin *et al.*, 2016). As the lowest $\delta^{11}B$ values of the Shasta inclusions are lower still, an explanation may be sought in fluid-melt interaction.

Fluid-melt isotope fractionation can be large (Kowalski *et al.*, 2018); even at very high temperature the exsolution and loss of fluids from hydrous melt can cause extensive loss of ^{11}B and, because $K_d^{\text{fluid-melt}}(B)$ is close, if not equal, to 1 in basaltic systems (Hervig *et al.*, 2002), this process may not be associated with a resolvable B depletion. It may be proposed that the low $\delta^{11}B$ values of some of the Shasta melt inclusions do not represent a particularly ^{11}B-depleted source component, but instead capture variably extreme degrees of fluid loss during melt ascent; a process that is already reflected in the fluid-mobile element signatures of the material (Le Voyer *et al.*, 2010). If this actually applies, the original B data (Rose *et al.*, 2001), as well as the data that has been produced since (Le Voyer *et al.*, 2010), could be explained entirely via mixtures between DMM and fluids derived from AOC—a much simpler and more plausible explanation than that provided above. Regardless, it is clear that the Mt. Shasta domain of Cascadia does not represent a 'normal' subduction setting and that the primitive melt inclusions found in the basaltic Shasta andesites reflect a complicated B signature that is anomalous among Shasta lavas, otherwise absent among Cascadia, and entirely unrepresentative of adakitic or other arc lavas worldwide.

The B signature of Archean granitoids—what we know so far

Although models for TTG petrogenesis involve a wide variety of settings and driving geodynamic mechanisms, these I-type granitoids are typically argued to derive from one of two sources: 1) the deep sections of thermally unstable mafic crust, or 2) mafic material that was altered at the surface and transported down by subduction or otherwise. In the case of a 'subduction' origin, TTGs may show a B signature similar to that of modern I-type granitoids and lavas from warm continental arcs. This is because 1) melting in such settings, or in very primitive versions thereof, is a possibly petrogenetic mechanism for TTG formation (Martin *et al.*, 2005; Moyen and Martin, 2012) and 2) the $\delta^{11}B$ values of two major components involved—oceanic lithosphere altered by seawater and MORB-DMM—were similar in the Archean as they are today. Links between TTGs and adakites have been made on the basis of major- and trace-element chemistry (*e.g.*, Martin *et al.*, 2005), as well as O isotopes (Bindemann *et al.*, 2005), although this link is questioned (Smithies, 2000) and melting of MORB-like or otherwise mafic sources in settings other than active margins could equally explain the data (*e.g.*, Moyen and Martin, 2012; Johnson *et al.*, 2017). One aspect in which either would certainly be different is that, unlike with adakites, TTGs do not reflect a component of a mantle wedge (Smithies, 2005). Whether this would have any effect on B systematics is highly questionable, because of the very low B concentrations and MORB-like $\delta^{11}B$ of the mantle. In the alternative models, which explain Archean TTG formation by deep garnet-stable melting of mafic crust, would predict a MORB-like B signature with low B concentrations (1.2-1.3 ppm; Marschall *et al.*, 2017) and $\delta^{11}B$ values similar to that of DMM (−7.1 ± 0.9 ‰, after Marschall *et al.*, 2017).

Boron isotope studies in Archean rocks have largely focused on tourmaline, specifically detrital tourmaline in Archean sediments (*e.g.*, Chaussidon and Appel, 1997). Very few B studies have been done on bulk Archean TTGs to investigate their petrogenetic setting. Archean granitoids rocks from various cratons were shown to exhibit low B concentrations and B/Nb values, which are similar to those of the LCC, or show very high B concentrations that exceed those typically observed in the modern UCC (Mohan *et al.*, 2008). The B-rich TTGs were interpreted to represent a distinct TTG subtype that, unlike other TTGs, did form in primitive subduction settings. This interpretation is nevertheless not entirely certain, because the nature and setting of these rocks, and the interpretation of their high concentrations of B and other fluid-mobile elements (Li, Be, and As) as tracing slab-derived fluids is not unique. The high concentrations were observed only in rocks from the Abitibi Greenstone Belt in Ontario and in the Eastern

Dharwar Craton, India—specifically from highly metallogenic regions in these terranes, which host abundant, (sub-)economical volcanogenic massive sulfide and gold mineralization (Mohan *et al.*, 2008; Piercey *et al.*, 2008). The samples for which B data were obtained are not typical TTG lithologies, but instead largely comprise quartz-feldspar porphyry rocks and intermediate volcanic rocks from volumetrically minor intrusions that are directly associated with volcanogenic massive sulfide mineralization, porphyry-style alteration and Cu-Mo-Au deposition. Although yet unconstrained for the Dharwar samples, the Abitibi samples show elevated Cu concentrations up to 2,500 ppm (Piercey *et al.*, 2008). Samples from the other TTG terranes (Western Dharwar, Wyoming Cratons, and the Amîtsoq and Itsaq Gneisses) lack elevated B concentrations, and B/Be and B/Nb values (Mohan *et al.*, 2008); they contain 2 ppm B on average, which is identical to the concentrations observed for TTGs in this study. It would appear from B studies done so far that global Archean TTGs are indistinguishable from the refractory lower crust in terms of B concentrations. In contrast, B-rich mineralised rocks such as those sampled in East Dharwar and the Abitibi Greenstone Belt represent shallow localised magmas rather than a separate globally significant TTG subtype.

Supplementary Introduction 2: Sampling and analytical strategies

The samples analysed in this study are: 1) 3.78 Ga tonalite gneisses from the Isua Greenstone Belt, Itsaq Gneiss Complex, West Greenland; 2) ≥3.6 Ga tonalite and trondhjemite gneisses from the Acasta Gneiss; 3) 3.58 Ga tonalite gneisses from the Bastar Craton, Central India; 4) 2.87-2.79 Ga tonalite and trondhjemite gneisses from the Tartôq Greenstone Belt, Southwest Greenland. A description of the geological setting and age signatures of each of these suites of samples is provided as Supplementary Introduction 3. The samples provide no visible evidence for low-grade overprinting or hydrothermal alteration and their zircon grains yielded only single U-Pb age populations.

To allow further temporal and spatial coverage, >3.6 Ga tonalite and trondhjemite gneisses from the Acasta Gneiss, Canada, were subjected to B analysis. These specific samples are known to be polymetamorphic (e.g., Stern and Bleeker, 1998). To estimate the $\delta^{11}B$ value of the igneous protolith of these rocks, B isotope analysis was done in situ on biotite inclusions in seemingly primary Eoarchean zircon. Such zircon occurs as single grains with one growth zone or as cores in more complex zircon grains with core and rim structures. The analysed biotite inclusions typically show euhedral crystal shapes and are not associated with alteration or secondary phases, indicating they are primary and at least as old as their zircon host, and contain B of the igneous protolith. The work flow for this overall analytical protocol is summarised in figure S-2, and analytical methods and data for each of the applied methods is provided in Supplementary Analytical Methods and Data.

The samples analysed in bulk were chosen for their pristine nature. Nevertheless, any sub-solidus alteration may be minor and cryptic (Putnis and John, 2010), and can never be a priori excluded on the basis of textural analysis alone. In metasomatised continental crust, such alteration typically leads to elevated $\delta^{11}B$ values (Bast *et al.*, 2014). To investigate this effect for TTGs, we also analysed: 1) a meta-tonalite (sample *508281*) from the Tartôq Greenstone Belt, which records pervasive greenschist-facies overprinting and 2) biotite from the matrix of the most strongly altered samples of the Acasta Gneiss. Meta-tonalite *508281* yielded a $\delta^{11}B$ value 5.1 ± 0.3 ‰ higher than pristine Tartôq tonalite. Biotite grains from the partially altered matrix of the Acasta Gneiss

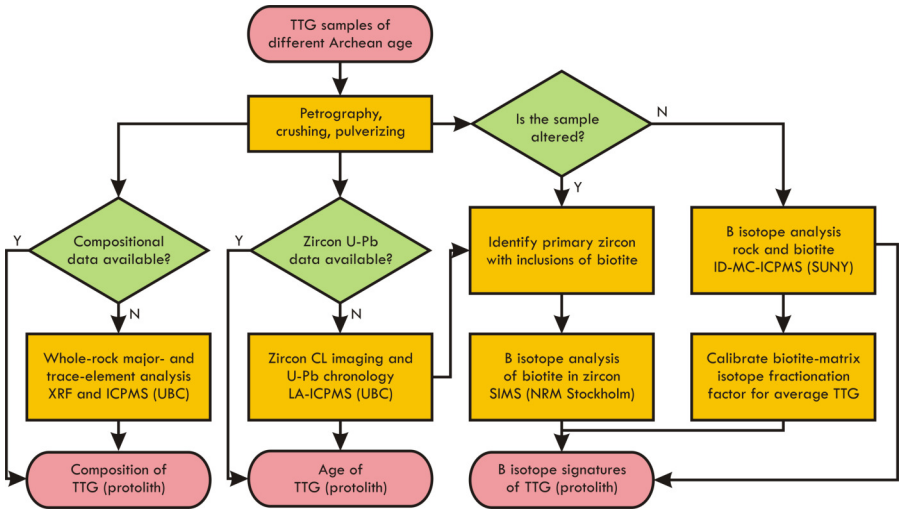

Figure S-2 Flow chart demonstrating the analytical workflow applied in this study.

have four-times-higher B concentrations and up to 15 ‰ higher $\delta^{11}B$ values than biotite inclusions in zircon from the same sample (Table S-4). Likewise, biotite inclusions with lowest $\delta^{11}B$ values are hosted in zircon domains that seem pristine (*e.g.*, Fig. 4c), whereas biotite grains yielding -10 ‰ or higher occur in zircon that shows disturbed U-Pb systematics and signs of alteration (Fig. 4d; Table S-4). It is clear what kind of effect sub-solidus alteration would have on B datasets. In contrast to the Acasta Gneiss dataset, this effect may not play a significant role in the data from the TTGs analysed in bulk; correlations between $\delta^{11}B$ and fluid-tracer indices (*e.g.*, B/Nb, B/Zr, B/Yb or B/La) are not observed and, instead, the samples preserve correlated $\delta^{11}B$ and Zr/Hf—a correlation that any alteration would obliterate. For the Acasta biotite inclusions it can conservatively be concluded that their $\delta^{11}B$ values, and the modelled whole-rock $\delta^{11}B$ value obtained from these by applying a biotite-rock isotope fractionation factor (see Supplementary Analytical Methods and Data), provide maximum estimates of the protolith $\delta^{11}B$ value.

Supplementary Introduction 3: Geological description and age of the TTG samples

Isua Greenstone Belt (IGB)

The IGB is part of the Eoarchean Itsaq (Amitsôq) Gneiss Complex in West Greenland, and represents a large crustal terrane with Eoarchean protoliths. The terrane comprises ancient mafic and ultramafic rocks, chemical and clastic sediments, and rocks of the TTG suite, which were variably overprinted at various times during the Archean. The IGB preserves panels of 3.75- to 3.6 Ga rocks, which are among the oldest in the region (Nutman *et al.*, 1996; Whitehouse *et al.*, 1999; Kamber *et al.*, 2003; Amelin *et al.*, 2011). Interpretations diverge regarding the origin of the IGB and the Itsaq Gneiss Complex as a whole. Whole-rock Sr and Nd isotope data suggest that much of the complex is juvenile and formed in an active margin setting (Moorbath *et al.*, 1973; Bennett *et al.*, 1993; Nutman *et al.*, 2007). Zircon U-Pb and Hf isotope data for IGB TTG rocks suggest, however, that they evolved from an older, possibly Hadean, source (Næraa er al., 2012). A comprehensive model involving crust generation and differentiation through volcanic resurfacing and density driven overturning has been proposed as an alternative to explain the complex history of the Itsaq Gneiss Complex (Kamber *et al.*, 2005). For the purpose of this study, two samples were selected from the IGB; both are 3.78 Ga granoblastic tonalite gneiss samples documented previously (Næraa *et al.*, 2012), which show typical TTG-like REE signatures with low Yb_N (Fig. S-3). The samples were chosen because of their exceptional preservation of primary mineral assemblages; the rocks contain no evidence for sub-solidus alteration, neither in their petrological, nor in their geochronologic record. Single age populations were obtained at 3,780 ± 6 (*070026*) and 3,781 ± 6 Ga (*070027*), constraining the protolith age (Næraa *et al.*, 2012).

Table S-2 Summary of samples analysed in this study.

Sample	Rock type	$^{207}Pb/^{206}Pb$ age (Ma)	Latitude	Longitude	Main minerals	Accessories
*Isua Greenstone Belt**						
070026	Tonalite	3,780 ± 6	65°05.178 N	50°10.632 W	pl, kfs, qtz, bt	ep, ms, ap, zrn
070027	Tonalite	3,781 ± 6	65°05.160 N	50°10.548 W	pl, kfs, qtz, bt	ms, ap, zrn
Acasta Gneiss Complex						
AMS001	Tonalite gneiss	3,589 ± 53	65°10.118 N	115°33.551 W	pl, qtz, bt, grt	zrn, ap
AMS027	Trondhjemite gneiss	3,721 ± 22	65°09.893 N	115°36.083 W	pl, kfs, qtz, bt, ms	zrn, ap
AMS030A-A†	Trondhjemite gneiss	3,694 ± 33	65°10.177 N	115°35.278 W	pl, kfs, qtz, bt, ms	zrn, ap
AMS030C†	Trondhjemite gneiss	3,599 ± 37	65°10.177 N	115°35.278 W	pl, kfs, bt, qtz	zrn, ttn
AMS031A	Tonalite gneiss	3,654 ± 18	65°10.177 N	115°35.278 W	pl, bt, hbl, qtz	ap, ttn, ilm, zrn
AMS039	Granodiorite gneiss	3,766 ± 38	65°09.770 N	115°32.847 W	pl, qtz, bt, hbl	zrn, ap
Bastar Craton‡						
AMA-01c	Granodiorite gneiss	3,503 ± 9	20°04.970 N	80°41.020 E	pl, kfs, qtz, bt, ms	zrn, ap
AMA-03c	Granodiorite gneiss	3,470 ± 17	20°04.220 N	80°40.020 E	pl, kfs, qtz, bt, ms	zrn, ap
AMA-04	Granodiorite gneiss	3,582 ± 43	20°06.680 N	80°41.480 E	pl, kfs, qtz, bt, ms	zrn, ap
Tartôq Greenstone Belt						
518001	Tonalite gneiss	2,835 ± 15	61°49.065 N	49°16.487 W	pl, qtz, kfs, bt, hbl	zrn, ap
518006	Tonalite gneiss	2,875 ± 20	61°49.224 N	49°15.919 W	pl, qtz, kfs, bt, ms	zrn, ap
518008	Tonalite gneiss	2,789 ± 36	61°48.328 N	49°17.354 W	pl, qtz, kfs, bt, ms	zrn, ap
468623	Tonalite gneiss	2,842 ± 24	64°11.082 N	50°16.376 W	pl, qtz, kfs, bt, grt	zrn, ap
508281§	Tonalite gneiss	2,809 ± 20	62°08.415 N	49°31.765 W	pl, qtz, kfs, bt, ms, ep	zrn, ap

*Næraa *et al.*, 2012.
†Layers that yielded a 4.0-Ga U-Pb age component (Fig. S-4) and a ^{147}Sm-^{143}Nd whole-rock date of similar age (Sprung *et al.*, 2016).
‡Maltese *et al.*, 2017
§Overprinted at greenschist-facies conditions.

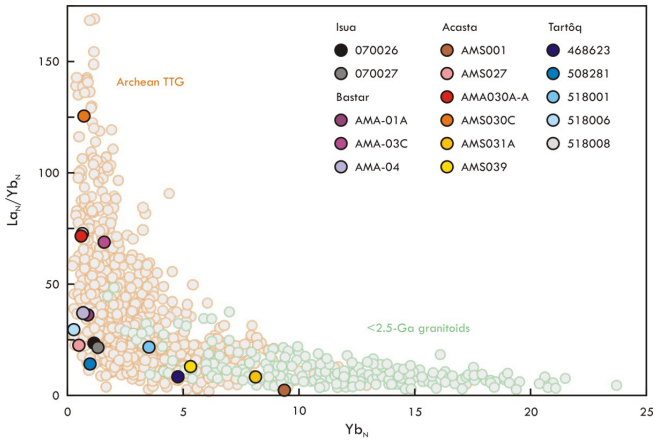

Figure S-3 Trace-element classification diagram for plutonic rocks (after Moyen and Martin, 2012). All samples show La_N/Yb_N and Yb_N values that are common among Archean TTG. Data provided as Supplementary Table S-7.

Acasta Gneiss Complex (AGC)

The AGC is exposed in the western segment of the Archean Slave Craton, Northwest Territories, Canada (Bowring *et al.*, 1989). The terrane contains some of the oldest relics of ancient crust on Earth. It largely comprises coarsely banded gneisses of gabbroic, to TTG and granitic composition, and has been interpreted as the oldest remaining remnant of the proto-cratonic core of the Slave craton. Uranium-lead dating of zircon in various AGC lithologies provided a range of results indicating a long and complex history (4.2-3.3 Ga; Bowring *et al.*, 1989; Stern and Bleeker, 1998; Bowring *et al.*, 1999; Iizuka *et al.*, 2006; Reimink *et al.*, 2014). Among the spectrum of ages, 3.72 to 3.60 Ga ages are most common and are taken to represent crystallization of the dominant igneous protoliths. Older ages of 4.2-4.0 Ga are obtained from lower strain enclaves of typically mafic composition (Iizuka *et al.*, 2006; Reimink *et al.*, 2014). A similar result was obtained from a ^{147}Sm-^{143}Nd isochron for the samples that were analysed for B isotopes in this study (*AMS030A-A*, *AMS030C*, and *AMS031A*; Sprung *et al.*, 2016). Tonalite *AMS001* and *AMS031A*, trondhjemite *AMS027* and *AMS030A-A*, and granodiorite *AMS039* were additionally chosen for this study, because they preserve relatively pristine high-grade mineral assemblages (Table S-2). Samples *AMS030A-A* and *AMS030C* are two layers in the same rock. All samples show REE systematics typical of TTG rocks (Fig. S-3). Zircon in the samples shows oscillatory, sector-zoned or patchy zoning in cathodoluminescence (CL) images.

Zircon grains from the AGC exhibit very complex U-Pb systematics, as is typical of TTG-type rocks from this complex (Stern and Bleeker, 1998), with clear evidence for substantial discordance (Fig. S-4). To evaluate the age components present among the complex systematics, the following protocol was followed: 1) for samples showing a single population (partly discordant), the age was estimated from the upper intercept with the concordia curve (*AMS031*, *AMS039*); 2) for samples inheritance with multiple populations, probability density plots were constructed using all $^{207}Pb/^{206}Pb$ data. The data were split into separate populations and upper intercepts were determined. If significantly different, these intercepts were taken to represent individual components (*AMS001*); 3) for remaining samples, the clustering data that were >90 % concordant were used to calculate weighted-mean ages. These were calculated from the $^{207}Pb/^{206}Pb$ ages, which for such high degrees of concordance best approximate possible upper intercepts. For the remaining data that were >90 % concordant, the range of $^{207}Pb/^{206}Pb$ ages were provided (Fig. S-4).

Some grains in *AMS030A-A* and *AMS030C* yielded concordant results between 3.97 to 3.89 Ga, which are identical to a ^{147}Sm-^{143}Nd isochron age obtained for these samples (Sprung *et al.*, 2016). This component is also reflected in a series of discordant analyses, most notably in *AMS001* (n > 10). These ages demonstrate that some of the protolith of these TTG samples is similarly old as the 4.0 Ga rocks that were found among mafic enclaves in the eastern AGC (Reimink *et al.*, 2014). The main age population in these and other AGC samples is between 3.72 and 3.60 Ga (Fig. S-4). Zircon yielding such ages and showing <10 % discordance typically shows pronounced oscillatory or sector zoning, indicating a magmatic origin. For rocks having an older protolith, such zircon would thus represent a major stage of anatexis, re-melting or melt injection. Younger components are observed between 3.59 or 2.86 Ga, as well as a series of discordant results that reflect Pb loss. In contrast to pre-3.6 Ga zircon, younger zircon typically shows a spongy appearance. It is likely that these zones represent sub-solidus re-equilibration of zircon, possibly as a result of hydrothermal alteration and metamorphic overprinting.

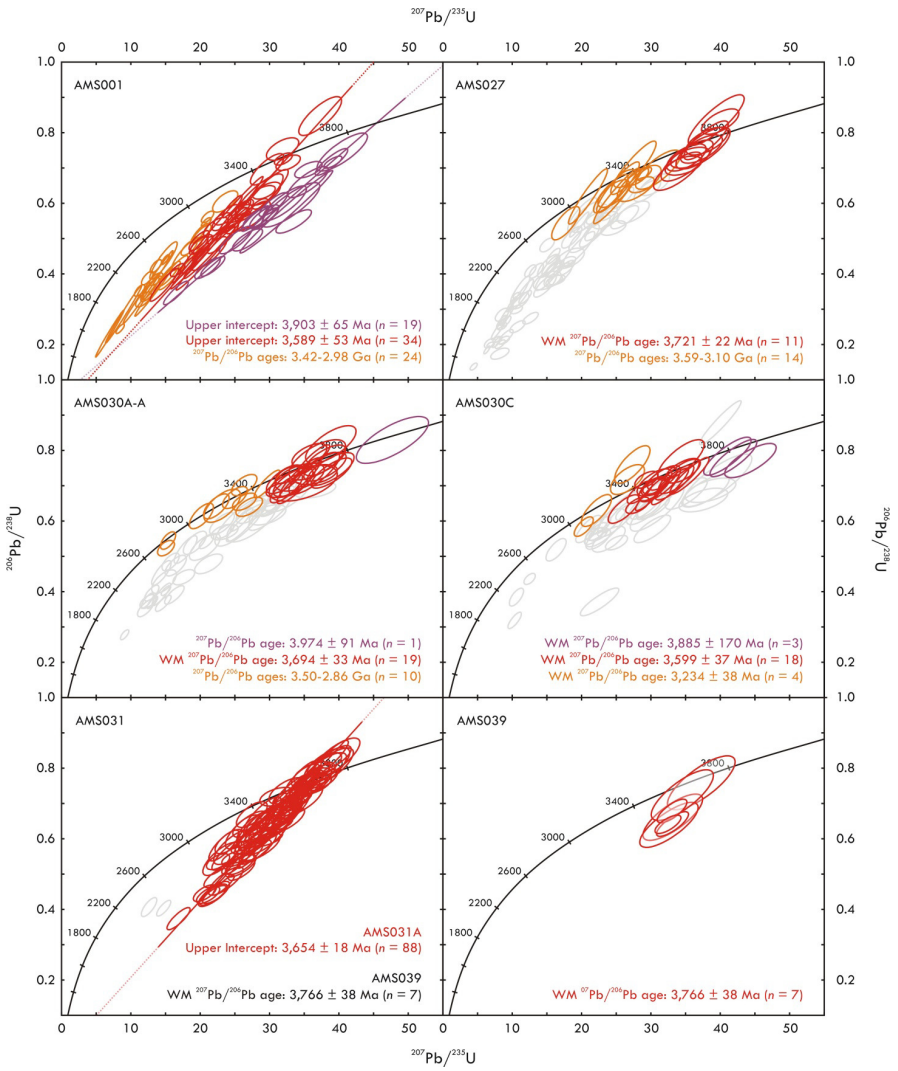

Figure S-4 Concordia diagrams showing U-Pb data for the Acasta Gneiss Complex samples.

Bastar Craton (BC)

The BC represents one of the oldest terranes of India. The terrane lies in Central India and exposes a variety of 3.5 to 3.0 Ga rocks, including TTG and granite gneiss, felsic and mafic intrusive rocks, banded iron formation, and clastic (meta-)sediments. The BC underwent a complex history of terrane amalgamation, magmatism and metamorphism lasting well into the Neoarchean (Ramakrishnan, 1990; Naqvi, 2005; Sharma, 2009). The oldest fragments of continental crust found in the BC are represented by 3.58 Ga gneisses and granitoids (Sarkar *et al.*, 1993; Ghosh, 2004; Rajesh *et al.*, 2009). These rocks represent a major addition of juvenile crust in the region (Maltese *et al.*, 2017) and may share a genetic link with rocks of similar age and composition found in other Archean cratons in India (Ghosh, 2004). In this study, we focussed on three samples of tonalitic to granodioritic composition (Table S-2). The samples represent some of the most pristine TTG found in the region. The rocks show well-preserved TTG-like REE signatures (Fig. S-3). Zircon U-Pb dating of these samples (Maltese *et al.*, 2017) yielded concordia ages of 3,503 ± 9 (*AMA01*), 3,470 ± 17 (*AMA03*), and 3,582 ± 43 Ma (*AMA04*), which are identical to those of other juvenile rocks.

Tartôq Greenstone Belt (TGB)

The TGB is a supracrustal belt within the Kvanefjord Block (Windley et al., 2009). The TGB comprises an amalgamation of tectonic panels consisting of metamorphosed basalt, gabbro, peridotite, and sediments, which were intruded by 3.0 Ga TTG complexes and folded into the Archean orthogneisses and TTG complexes of the North Atlantic Craton (Nutman and Kalsbeek, 1994; Kisters et al., 2012; Szilas et al., 2013). The geochemical composition of mafic and ultramafic rocks indicates that these represent fragments of

oceanic crust that formed in a back-arc setting. Intrusion of the TTG-type rocks occurred when these fragments developed into a subduction-accretion complex (Kisters et al., 2012; Szilas et al., 2013; Polat et al., 2015). Felsic mylonites within the TGB, which are compositionally similar to granodiorites of the TTG suite, are interpreted as products of basalt melting within the inferred accretionary prism (Polat et al., 2016).

Five TTG samples were taken from the areas of the Fredrikshåb Isblink glacier (*468623*), Tartôq (*508281*) and Kvanefjord-Neria (*518001*, *518006*, and *518008*; Table S-2; Fig. S-3). The Fredrikshåb Isblink and Kvanefjord-Neria samples represent some of the best-preserved TTG rocks in the area. The Tartôq sample is from a section of the greenstone belt where greenschist facies overprinting is pervasive. This is reflected in sample *508281*, which contains abundant epidote, albite and muscovite. Zircon in TGB samples shows pristine oscillatory or sector zoning, or faint to no zoning in CL images. Zircon grains were subjected to U-Pb analysis as part of this study. The zircon grains from the TGB yielded U-Pb data that were consistent and largely concordant (Fig. S-5). The following concordia ages were obtained: 2,842 ± 24 (*468623*), 2,875 ± 20 (*508281*), 2,835 ± 15 (*518001*), 2,809 ± 20 (*518006*), and 2,789 ± 36 Ma (*518008*). All the results are all identical within error and constrain the age of the protolith precisely at the very end of the Mesoarchean.

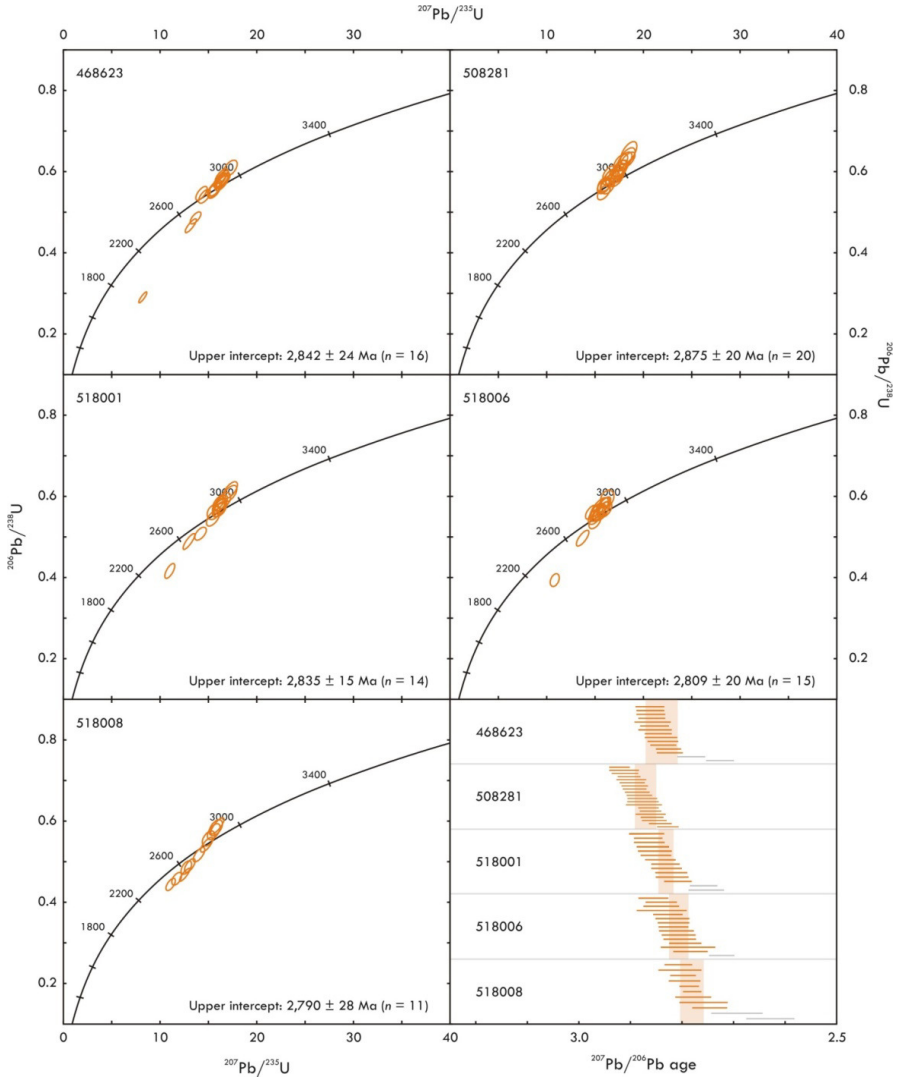

Figure S-4 Concordia diagrams and summary diagram showing U-Pb age data for the TGB samples. Orange bars in compilation show weighted mean of $^{207}Pb/^{206}Pb$ ages with discordant outliers in grey.

Supplementary Discussion: Boron data comparison and implications for TTG petrogenesis

Geochemical modelling of TTG B-Zr-Hf

The co-variation of B and Zr/Hf (Fig. 2a) was investigated through chemical modelling of TTGs melts using minerals that are common in TTG systems (amphibole, clinopyroxene, plagioclase and garnet). The calculations were done for equilibrium (Eq. 1) and fractionation (Eq. 2) crystallization. In the equations, the concentration of a species in the evolving melt (C_l) relative to the melt starting composition (C_l^0) is calculated as a function of the fraction of melt remaining (F) and the coefficient of solid-melt partitioning (K_d). The calculations were done assuming a source with chondritic Zr/Hf (34.2 ± 0.3; Weyer *et al.*, 2002) and 1.5 ppm B and using partition coefficients for basaltic systems as listed in Table S-3. The results are shown in Figure S-6.

$$\frac{C_l}{C_l^0} = F^{(K_d-1)} \qquad \text{(Eq. 1)}$$

$$\frac{C_l}{C_l^0} = \frac{1}{F\,(K_d\text{-}1) + K_d} \qquad \text{(Eq. 2)}$$

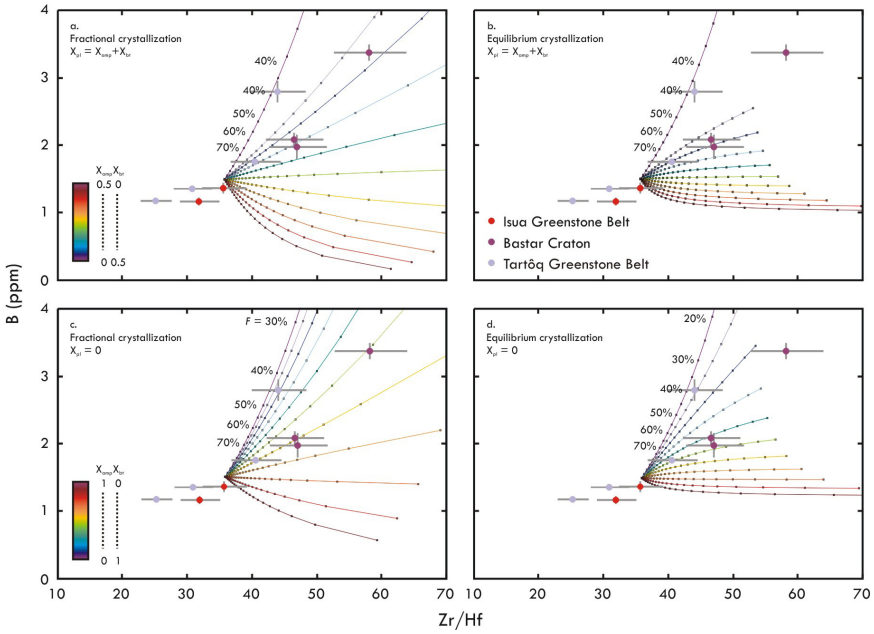

Figure S-6 Chemical trends in melt undergoing fractional crystallization (a, c) and equilibrium crystallization (b, d) of assemblages containing (a, b) various amounts of amphibole and biotite at fixed plagioclase content (equal to amphibole and biotite) or (c, d) amphibole and biotite only. X_{amp}, X_{bt}, and X_{pl} are the relative fraction of each mineral. A starting composition with 1.5 ppm B and chondritic Zr/Hf is assumed, but trends would be the same for different starting B and Zr/Hf. Numbers indicate the fraction of melt remaining.

Equilibrium and fractional crystallization of mixtures between biotite and amphibole, possibly in the presence of plagioclase, can produce the chemical fractionation trends as observed for the analysed TTGs (Fig. S-6). The data with B and Zr/Hf higher than the starting composition (1.5 ppm B and chronditic Zr/Hf) resemble the modelled melt, while those with lower values may represent cumulates left behind by this melt. Amphibole crystallization affects Zr/Hf most strongly, because Kd(Zr) and Kd(Hf) are relatively high, and quite different. Clinopyroxene crystallization causes a similar yet far smaller Zr/Hf fractionation due its lower K_d(Zr) and the fact that K_d(Hf), K_d(Zr)/K_d(Hf) is closer-to-unity. Thus pyroxene fractionation could explain the trends observed as well, but only if co-crystallizing with biotite, which is not expected during a normal crystallization series and it would not be able to increase SiO_2 enough to reach the compositions actually observed. Plagioclase crystallization affects only B concentrations and thus cannot alone explain the observed trends. If present as a liquidus phase, plagioclase suppresses B enrichment in the melt and thus reduces the degree of biotite crystallization needed to explain the observed trend (Fig. S-6a,b versus S-6c,d). Garnet is one of the few ferromagnesian minerals that do not fractionate Zr/Hf (Linnen and Keppler, 2002). The mineral also exhibits a very low K_d(B). As such, small amounts of garnet present as a liquidus phase will not affect the chemical trends caused by crystallization of amphibole or clinopyroxene. This could explain why a B-Zr/Hf trend is observed for samples that have high- and as well as low Gd_N/Yb_N (Figs 1, 2).

Table S-3 Partition coefficients used for geochemical modelling of TTG B-Zr-Hf. Values used in bold.

Sample Name	K_d(B)	Reference	K_d(Zr)	Reference	K_d(Hf)	Reference
Clinopyroxene	0.036	Hart and Dunn (1993)	0.195*	Johnson and Kinzler (1989)	0.305*	Dunn (1987)
	0.036	Klemme *et al.* (2002)	0.120	Kelemen and Dunn (1992)	0.340*	Johnson and Kinzler (1989)
	0.190	Elkins *et al.* (2008)	0.123	Hart and Dunn (1993)	0.233	McKenzie and O'Nions (1991)
			0.395*	Forsythe *et al.* (1994)	0.256	Hart and Dunn (1993)
			0.195	Hauri *et al.* (1994)	0.223	Hauri *et al.* (1994)
			0.128	Johnson (1994)	0.230	Johnson (1994)
			0.210	Jenner (1994)	0.200	Johnson (1998)
			0.119	Johnson (1998)	0.130	Elkins *et al.* (2008)
			0.280	Vannucci *et al.* (1998)		
			0.090	Elkins *et al.* (2008)		
average	*0.087*		*0.183*		*0.240*	
Amphibole	0.028	Tiepolo *et al.* (2007)†	0.500	Bacon and Druitt (1988)	0.430*	Luhr and Carmichael (1980)
			0.250*	Green *et al.* (1993)	0.500	Dostal *et al.* (1980)
			0.350	Sisson (1994)	0.540	Bacon and Druitt (1988)
			0.230	Brenan *et al.* (1995)	0.450	Brenan *et al.* (1995)
			0.470	Klein *et al.* (1997)	0.690*	Klein *et al.* (1997
			0.360*	Oberti *et al.* (2000)	0.665*	Oberti *et al.* (2000)
average	*0.231*		*0.360*		*0.522*	
Plagioclase	0.478	Bindeman *et al.* (1998)	0.010	Ronov and Yaroshevskiy (1976)	0.017	Okamoto (1979)
	0.166	Bindeman and Davis (2000)	0.007*	Bindeman *et al.* (1998)	0.020	Dostal *et al.* (1983)
	0.122	Bindeman and Davis (2000)	0.008*	Bindeman and Davis (2000)	0.010	McKenzie and O'Nions (1991)
			0.006*	Aignertores *et al.* (2007)	0.090*	Aignertores *et al.* (2007)
average	*0.255*		*0.007*		*0.016*	
Biotite	1.212‡	This study	0.017	Latourette *et al.* (1995)	0.190	Latourette *et al.* (1995)
			0.023	Foley *et al.* (1996)	0.230	Villemant (1988)
			0.140	Villemant (1988)	0.146	Fujimaki *et al.* (1994)
			0.136	Fujimaki *et al.* (1984)		
	1.212		*0.079*		*0.189*	
Garnet	0.014	Klemme *et al.* (2002)	0.800	Ronov and Yaroshevskiy (1976)	0.200	Kato *et al.* (1988)
			0.150	Kato *et al.* (1988)	0.230	McKenzie and O'Nions (1991)
			0.500*	Green *et al.* (1989)	1.220	Hauri *et al.* (1994)
			0.900	Kelemen and Dunn (1992)	0.240	Johnson (1994)
			2.120	Hauri *et al.* (1994)	0.727*	Salters and Longhi (1999)
			0.570*	Jenner *et al.* (1994)		
			0.270	Johnson (1994)		
			0.270	Johnson (1998)		
			0.688*	Salters and Longhi (1999)		
average	*0.014*		*0.784*		*0.523*	

*Average of estimates
†Summary of 22 experiments
‡Determined on the basis of B concentration data biotite and whole rock of the Isua tonalites by isotope dilution (Table S-5).

Comparison B isotope data between TTG and other terrestrial rocks

To evaluate the significance of the B data for the TTG petrogenesis, the data are compared to those observed in the global rock record. This comparison is first made using $\delta^{11}B$ values, for which there are far more estimates than B concentration. Comparison between TTG (data for the Acasta Gneiss obtained from biotite data by applying and F of 1.0036 ± 0.0006; Supplementary Information) and characterised terrestrial reservoirs was done by assessing overlap and distributions of data populations. Population overlap was quantified through the parameter P_{50}, which represents the degree of overlap between the central 50 % of the data for two populations of continuous data. The parameter is defined through Equation 3, where IQR represents the inter-quartile range (Q_3-Q_1) of population i (TTG) and the test population j, and X_n and X_1 are the maximum and minimum of these populations, respectively. Values below 0 indicate that there is no IQR overlap ($Q_{3,i} < Q_{1,j}$).

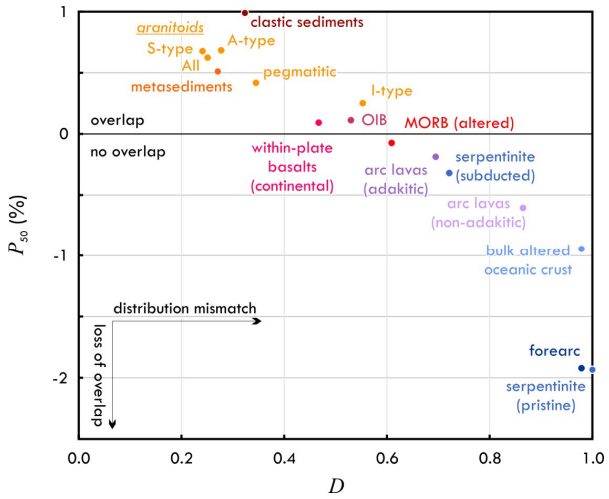

Figure S-7 Statistical population analysis for the comparison of $\delta^{11}B$ values between TTG and the reference reservoirs. P_{50} is the overlap parameter quantifying the degree of overlap between $\delta^{11}B$ values of the reference reservoir and TTG, and D is the Kolmogorov-Smirnov statistic, which provides a measure of the dissimilarity in data distribution between these. Detailed definitions of these parameters are provided in the methods section.

Populations were furthermore tested for similarity using the Kolmogorov-Smirnov (K-S) test. This is nonparametric and enables a quantitative assessment of the degree of equality between empirical distribution functions of continuous datasets. The test is based on the value of the K-S statistic D. The value of D is calculated using Equation 4, where $F_m(x)$ and $G_n(x)$ are the empirical distribution functions from the TTG (size n) and reference dataset (size m), respectively. Values of 0 and 1 for D indicate complete similarity and dissimilarity in terms of extremes and probability distribution, respectively. The results are shown in Figure S-7. The number of $\delta^{11}B$ values documented per study or location was not equal. To avoid population-size-dependent bias, we assessed the effect of population size by comparing the median of a reference reservoir to the mean of medians of individual datasets for that reservoir. These values do not differ by more than 2 ‰ for the igneous rocks investigated here (Table S-1). Differences in population sizes for different datasets thus do not significantly affect the population description.

$$P_{50} = \frac{IQR_i + IQR_j - (X_{n,Q_{3,ij}} - X_{1,Q_{1,ij}})}{IQR_i} \qquad \text{(Eq. 3)}$$

$$D = \sqrt{\left(\frac{mn}{m+n}\right)} \sup_x |F_m(x) - G_n(x)| \qquad \text{(Eq. 4)}$$

The comparative population analysis on global $\delta^{11}B$ data shows that TTGs resemble none of the igneous rock types that are produced in active or Cordilleran margin. The $\delta^{11}B$ values of the TTGs are substantially and systematically lower than those of I-type granitoids, as well as adakites, let alone non-adakitic arc lavas that may reflect a stronger component of slab-derived fluids rather than melts. The differences are clear in terms of their central value, range and population distribution. This applies even when disregarding the possibility that some of the Acasta protolith $\delta^{11}B$ values may be overestimated (see Supplementary Introduction 2). More insight is obtained from the available B concentration data (Table S-1). In the vast majority of cases, B concentrations of adakite are at least twice as high as observed here. Furthermore, all adakite data available so far show a positive rather than a negative correlation between $\delta^{11}B$ value and B concentration. These considerations support the inference made on the basis of major-element compositions (Smithies, 2005) that TTG and adakite, and by extension 'normal' arc magmas, do not reflect the same petrogenetic processes and setting.

Supplementary Analytical Methods and Data

Boron isotope analysis

In situ analysis of biotite

In situ B isotope analysis of biotite inclusions preserved in zircon from the Acasta samples was done by secondary ion mass spectrometry (SIMS). The selection of biotite inclusions for B isotope analysis was done on the basis of requirements for both the biotite inclusion and its zircon host. Biotite inclusions were selected for analysis only 1) if they showed euhedral or otherwise well-

developed crystal shape and were not associated with any cracks, and 2) if their zircon host grain or grain domain shows primary oscillatory or sector zoning indicative of a magmatic origin and yielded U-Pb dates that were <10 % discordant and had $^{207}Pb/^{206}Pb$ dates older than 3.6 Ga. Examples of inclusions in such zircon are provided in Figure 3 of the main text. In addition, matrix biotite grains from the altered matrix of samples *AMS001* and *AMS030A-A* were analysed to test the effects of alteration on B isotope systematics. For the other samples, B isotope were analysed in bulk rock or biotite separates (Isua) using multi-collector inductively coupled plasma mass spectrometry (MC-ICPMS).

The B isotope analysis of biotite inclusions in zircon was done by secondary ion mass spectrometry (SIMS) at the NordSIMS laboratory, Swedish Museum of Natural History, Stockholm, using a CAMECA *IMS-1280* large-geometry SIMS instrument. The analytical protocols closely followed those described previously (Deegan *et al.*, 2016). An aperture-illuminated, 6-nA O^{2-} primary beam with incident energy of 23 kV was used to sputter ions from selected slightly elliptical (~20 μm-long) areas of the gold-coated sample. Before each analysis, the primary beam was rastered over a square area of 25 × 25 μm^2 around the spot for 150 seconds to remove the gold coating and minimise surface contamination. Contamination was further discriminated against by use of a field of view on the sample (as determined by the field aperture and transfer magnification settings) of ~30 μm, i.e. smaller than the pre-sputtered area. Following the pre-sputter, the 10 kV secondary ion beam was centred in the field aperture, its energy optimised in the 45 eV energy window, and the mass calibration adjusted using the $^{11}B^+$ signal. Secondary ions were measured over 60 cycles through the mass stations 9.33 (background, 2 s integration), $^{10}B+$ (8 s), $^{11}B^+$ (4 s) and $^{30}Si^{2+}$ (matrix, 2 s), using a low-noise (<0.005 cps) ion-counting electron multiplier. The assigned mass resolution ($m/\Delta m$) of 3003 was sufficient to eliminate the isobaric interference of $^{10}B^1H^+$ on $^{11}B^+$.

The phengite reference material *MVJ84-29-1* ($\delta^{11}B$ = -9.0 ± 0.9 ‰; [B] = 87 ppm; Harlow 1994; Martin *et al.*, 2015), obtained from phengite-albite rocks in the Motagua Valley, SE Guatemala, was used. Analyses of this material were interspersed at regular intervals during the analytical session, along with analyses of the NIST *SRM 610* glass reference material, which was used to monitor ratio drift. To assess orientation effects, grains of *MVJ84-29-1* phengite were mounted with the c-axis parallel and perpendicular to the polished surface. We obtained $\delta^{11}B$ values of -9.8 ± 0.8 ‰ and -8.2 ± 0.8 ‰ for repeated c-parallel and -perpendicular analyses, respectively. Because the crystallographic orientation of biotite inclusions in zircon could not be determined, the observed $\delta^{11}B$ difference between crystallographic orientations was propagated in quadrature as additional uncertainty for all analyses. Phengite *Phe80-03* (-14.8 ± 2.8 ‰; Pabst *et al.*, 2012) was analysed during the course of our analytical session to assess accuracy. A weighted mean $\delta^{11}B$ value of -16.6 ± 2.9 ‰ (n = 15) was obtained, which indicates accuracy within external reproducibility (Table S-4). All B data for biotite inclusions is provided in Table S-5.

Table S-4 Boron isotope data for secondary reference material *Phe80-03* analysed by SIMS.

Sample Name	$\delta^{11}B$ (‰)	2σ
Phe80-03 (phengite; -14.8 ± 2.8 ‰; Martin et al., 2015)		
Phe80-03 (1)	- 15.7	1.9
Phe80-03 (2)	- 16.4	1.6
Phe80-03 (3)	- 17.8	1.3
Phe80-03 (4)	- 16.7	1.5
Phe80-03 (5)	- 15.8	1.8
Phe80-03 (6)	- 14.3	1.4
Phe80-03 (7)	- 16.8	1.5
Phe80-03 (8)	- 13.6	1.4
Phe80-03 (9)	- 16.8	1.6
Phe80-03 (10)	- 18.7	1.3
Phe80-03 (11)	- 17.9	1.7
Phe80-03 (12)	- 17.0	1.6
Phe80-03 (13)	- 15.8	2.2
Phe80-03 (14)	- 18.1	1.5
Phe80-03 (15)	- 18.0	1.4
Average (2 s.d.)	- 16.6 (2.9)	

Bulk analysis of biotite and rock

Biotite separates were prepared from crushed Isua samples *070026* and *070027*. The grains were separated by magnetic separation and hand-picking under a binocular microscope. Aliquots of approximately 100 mg of biotite and whole rock powder (Aliquot *C*) were sintered at 490°C in glassy carbon crucibles in a muffle furnace together with Na_2O_2 powder at Lamont-Doherty Earth Observatory (Kleinhanns *et al.*, 2002; Cai *et al.*, in prep.). The sintered cakes were cooled down and reacted with de-ionised H_2O to

Table S-5 Boron isotope analyses for biotite and whole rocks for TTG samples.

Sample Name	$\delta^{11}B$ (‰)	2σ	[B] (ppm)[†]	Altered (y/n)[‡]	Host-zircon age Concordance (%)[4]
Biotite (SIMS, NordSIMS Stockholm)					
Acasta Gneiss Complex					
Biotite inclusions in zircon*					
AMS001_big_028	- 5.4	2.2	17	y	66
AMS001_big_035	- 16.7	1.9	75	n	85
AMS001_015	- 15.2	1.7	71	n	103
AMS001_016	- 10.8	1.6	18	y	63
AMS001_005a	- 21.3	4.6	1.0	n	79
AMS001_005b	- 9.4	4.2	1.7	y	67
Biotite inclusions in zircon*					
AMS001_009	- 5.7	1.3	80	y	76
AMS001_011	- 6.5	1.4	64	y	59
AMS001_012	- 6.3	1.5	41	y	69
AMS001_013	- 8.8	1.9	30	y	77
AMS027_037	- 21.9	1.8	11	n	97
AMS030A-A_002	- 19.6	1.5	21	n	80
AMS030A-A_081	- 24.1	1.8	25	n	92
AMS030A-A_020	- 17.2	1.6	33	n	83
AMS030C_065	- 13.6	2.9	15	y	82
AMS031A_025	- 16.1	1.8	17	n	99
AMS039_big_006	- 16.3	3.9	6.7	n	87
Matrix biotite (altered)					
AMS001_017	- 5.03	1.4	111	y	---
AMS001_010	+ 1.95	1.1	116	y	---
AMS030A-A_001	- 9.17	1.2	121	y	---
AMS030A-A_003	+ 5.02	1.2	124	y	---
Bulk analysis (MC-ICPMS, FIRST Stony Brook)[§]					
Isua Greenstone Belt					
070026	- 2.52	0.55	1.36	---	---
070026 (biotite)	- 7.78	0.16	1.94	---	---
070027	- 7.63	0.21	1.16	---	---
070027 (biotite)	- 6.05	0.26	1.44	---	---
Bastar Craton					
AMA01(1)	- 7.45	0.17	1.97	---	---
AMA01(2)	- 7.12	0.14	"	---	---
AMA03C	- 15.24	1.04	3.37	---	---
AMA04	- 10.99	0.22	2.08	---	---
Tartôq Greenstone Belt					
Pristine					
518001	-9.46	0.13	2.79	---	---
518006	- 2.95	0.20	1.17	---	---
518008	- 5.16	0.14	1.35	---	---
468623	- 8.83	0.17	2.12	---	---
Overprinted					
508281	+ 2.12	0.24	1.75	---	---

*Biotite analyses prior to application of fractionation factor to calculate whole-rock $\delta^{11}B$.
[†]Semi-quantitative estimate from comparing ion beam intensity of unknowns to that of bracketing drift-corrected NIST *SRM 610* and *MVJ84-29-1*.
[‡]Spongy or porous appearance and no preserved igneous zoning in CL.
[§]Bulk rock unless noted otherwise (biotite).

form a suspension. In this suspension, most of the cationic species precipitated as hydroxides, whereas a few water-soluble hydroxides, including $B(OH)_3$ and NaOH, remained in solution. This solution was centrifuged and only the supernatant was processed for B concentration. Boron was separated using Amberlite boron-specific ion-exchange resin following procedures modified from Hemming and Hanson (1994) at the Department of Geosciences, Stony Brook University. The B solutions were analysed by MC-ICPMS using a Nu Instruments *Plasma II* at the Facilities for Isotope Research and Student Training (FIRST), Stony Brook University. International rock reference materials were also processed, yielding values that correspond to those published (Table S-6). Generally, less than 1 ppm Na remained in the B solution after chemistry. Doping with up to 480 ppm Na in purified seawater show no deviation from expected values (Table S-6). All data for TTG whole rocks are included in Table S-5.

Table S-6 Boron isotope data for reference materials analyzed by MC-ICPMS.

Sample Name	$\delta^{11}B$ (‰)	2σ
Reference materials (MC-ICPMS, Stony Brook)		
GSJ JCp-1 (coral powder; +24.24 ‰; Brandt et al., 2014)		
Coral (1)	+ 23.64	0.06
Coral (2)	+ 24.16	0.16
Coral (3)	+ 24.25	0.09
Coral (4)	+ 24.41	0.06
Coral (5)	+ 24.51	0.04
Coral (6)	+ 24.94	0.07
Coral (7)	+ 24.67	0.18
$Coral_{+mannitol}$ (1)	+ 24.37	0.09
$Coral_{+mannitol}$ (2)	+ 23.61	0.11
$Coral_{+mannitol}$ (3)	+ 24.28	0.06
Average (2 s.d.)	+ 24.3 (0.8)	
GSJ JB-2 (basalt powder; +7.24 ‰; Brandt et al., 2014)		
JB2 (1; 12/16)	+ 7.68	0.42
JB2 (2; 12/16)	+ 6.30	0.27
JB2 (3; 26-02-2017)	+ 7.73	0.09
JB2 (4; 26-02-2017)	+ 6.79	0.09
Average (2 s.d.)	+ 7.1 (1.4)	
GSJ JR-2 (rhyolite powder; +3.07 ‰; *Rosner et al., 2004*)		
JR2 (1)	+ 3.57	0.07
JR2 (2)	+ 3.53	0.07
JR2 (3)	+ 4.28	0.08
JR2 (4)	+ 2.99	0.04
JR2 (5)	+ 3.48	0.08
JR2 (6)	+ 3.06	0.12
JR2 (7)	+ 2.21	0.08
JR2 (8)	+ 3.81	0.07
JR2 (9)	+ 3.56	0.11
JR2 (10)	+ 3.56	0.13
JR2 (11)	+ 3.05	0.08
JR2 (12)	+ 3.50	0.08
Average (2 s.d.)	+ 3.4 (1.0)	
NRC NASS-5 (seawater; +39.89 ‰; Brandt et al., 2014)		
SW (1)	+ 40.87	0.10
SW (2)	+ 39.73	0.07
SW (3)	+ 40.02	0.15
SW (4)	+ 39.32	0.16
SW (5)	+ 39.30	0.06
SW (6)	+ 40.79	0.05
SW (7)	+ 39.85	0.09
SW (8)	+ 39.82	0.04
SW (9)	+ 39.91	0.08
SW (10)	+ 40.20	0.07
SW (11)	+ 40.99	0.12
$SW_{+mannitol(10ppb)}$	+ 39.69	0.06

Sample Name	$\delta^{11}B$ (‰)	2σ
$SW_{+mannitol(120ppm)}$	+ 41.71	0.21
$SW_{+mannitol(240ppm)}$	+ 39.76	0.21
$SW_{+mannitol(480ppm)}$	+ 40.69	0.30
$SW_{+Na(120ppm)}$	+ 40.81	0.07
$SW_{+Na(360ppm)}$	+ 40.56	0.06
$SW_{+Na(480ppm)}$	+ 39.60	0.09
$SW_{+Na(9ppm)}$	+ 40.40	0.06
$SW_{+Na(50ppm)}$	+ 40.98	0.07
$SW_{+Na(10ppm)}$	+ 40.12	0.06
$SW_{+Na(50ppm)}$	+ 40.51	0.07
$SW_{+Na(100ppm)}$	+ 39.50	0.07
$SW_{+Na(200ppm)}$	+ 38.95	0.07
$SW_{+Na(400ppm)}$ (1)	+ 40.08	0.07
$SW_{+Na(400ppm)}$ (2)	+ 40.15	0.07
Average (2 s.d.)	+ 40.2 (1.3)	

Boron isotope fractionation between biotite and melt

Reconstructing bulk-rock $\delta^{11}B$ from biotite $\delta^{11}B$ data requires quantification of the isotope fractionation between biotite and remaining melt (Tonarini *et al.*, 2003). Values for the isotope fractionation factor *F*, defined here as $(^{11}B/^{10}B)_{matrix}$ / $(^{11}B/^{10}B)_{biotite}$, were experimentally determined to be 1.0027-1.0065 for melts with compositions similar to, or more evolved than, TTG crystallizing at 750-850°C (Tonarini *et al.*, 2003). In these experiments and in most magmatic rocks, biotite is a minor phase and B partition coefficients for biotite are 0.01 or less. This validates the assumption that, in terms of B concentration and $\delta^{11}B$, the melt was similar to the bulk rock minus biotite. On the basis of this assumption, *F* was quantified for TTG by comparing B isotope data for bulk-rock and multi-grain biotite separates from the IGB tonalite samples, as determined by MC-ICPMS. Assuming a setting of deep crustal melting, the solidus temperature for such rocks, and the temperatures for which this factor would apply, would be *c.* 800 °C (Moyen, 2011). The maximum value of *F* was determined to be 1.0036 ± 0.0006, which is within the range of values determined experimentally at similar crystallization temperatures for rocks that are similarly or more felsic than TTG lithologies (Tonarini *et al.*, 2003). The $\delta^{11}B$ value of biotite thus is equal to, or up to 3.5 ‰ higher than that of the melt.

Trace-element analysis

Boron concentrations were determined by isotope dilution analysis. The samples were pulverised using an agate mortar and pestle. Approximately 200 mg of whole-rock powder (Aliquot *A*) was subjected to flux fusion dissolution by adding approximately 800 mg of Na_2O_2 powder (Sigma Aldrich® reagent grade granular, +140 mesh particle size > 97 % purity) and heating to 490°C in glassy carbon crucibles in a muffle furnace at Stony Brook University. These sintered cakes were allowed to cool down and react completely with de-ionised H_2O. Any precipitated Fe-hydroxides were re-dissolved by adding concentrated HCl in small amounts until all the precipitate was dissolved and NaCl salts began forming (modified from Meisel *et al.*, 2001). A small amount of de-ionised H_2O was then added to the solution to dissolve those salts. Once the solution was completely clear, it was centrifuged and an aliquot was processed for B concentration analysis. Each aliquot of sample solution was spiked with a weighed quantity of *NBS-952*, which has a known non-natural $^{10}B/^{11}B$ value of 0.0532. These solutions were then agitated for several hours prior to B separation chemistry to ensure sample-spike equilibration. The purified spiked B solutions were also analysed for isotope compositions on a *Nu Plasma II* multi-collector inductively coupled plasma mass spectrometry (MC-ICPMS) instrument. Reference materials *BCR-1* (3.3 ± 0.2 ppm; Makashima *et al.*, 1997) and *JB-3* (20.9 ± 0.4 ppm, Makashima *et al.*, 1997) were analysed to monitor accuracy, yielding 3.6 ± 0.6 ppm and 20.2 ± 1.7 ppm, respectively.

Concentrations of other trace-elements were measured separately. Trace-element data for the Isua, Acasta and Bastar samples were presented previously (Næraa *et al.*, 2012; Sprung *et al.*, 2016; Maltese *et al.*, 2017). For trace-element analysis of the TTG samples from the Tartôq Greenstone Belt, approximately 100 mg of rock powder (Aliquot *B*) was digested with HF-HNO_3 (5:2) in screw-top PFA® beakers placed in Teflon© inside a steel-jacketed Parr digestion vessel and kept at 180 °C for 5 days. The equilibrated solutions were dried down, dissolved in 10 mL 6N HCl, diluted 5,000×, and analysed using a ThermoFinnigan *Element2* ICPMS instrument. Admixed ^{115}In was used as internal standard. External normalization was done on the basis of analyses of the *BHVO-1* basalt reference material bracketing each group of 3 samples. The data were normalised to Primitive Mantle (Hofmann, 1988). All data are provided in Figs. 1 and S-1, and in Table S-7.

Table S-7 Trace element data for the whole-rock samples.

	Isua Supracrustal Belt		Acasta Gneiss Complex					Bastar Craton		Tartôq Greenstone Belt				
Element	**070026**	**070027**	**AMS 030A-A**	**AMS 030C**	**AMS 031A**	**AMS 001**	**AMA01A**	**AMA03C**	**AMA04**	**518001**	**518006**	**518008**	**508281A**	**468623A**
Boron														
B	1.36	1.16	---	---	---	---	1.97	3.37	2.08	2.79	1.17	1.35	1.75	2.12
2 s.d.	0.08	0.06	---	---	---	---	0.18	0.12	0.1	0.16	0.04	0.02	0.02	0.16
Other														
K	7430	7679	12535	9713	13199	13199	7471	6682	5852	8343	6308	12950	5271	20089
Ti	1858	1918	1139	1559	6894	2997	1696	2709	1642	6173	1278	479	1978	1319
Rb	71.1	72.4	18.3	19.9	20.7	44.1	47	59	37	71.5	97.3	90.5	80.3	146.9
Sr	327.7	316.1	354	341	258	121	356	406	396	466.6	420	182.3	429.6	105.4
Y	6.5	7	3.7	4.1	35.8	25.8	4.7	6.7	3.6	20.8	18	2.4	5	18.8
Zr	132.2	137.4	141	170	419	513	146	303	112	224.9	252	80.4	121.8	183.8
Nb	4.1	4.3	2.4	4.22	15.4	19.9	5.5	6	4.3	10.8	3.98	3.3	5.2	5.6
Cs	2.9	3.1	0.305	0.369	0.416	0.997	0.5	1.8	0.7	1	0.89	0.6	2.3	0.3
Ba	291	276	430	409	460	388	247	491	205	604	802	1399	245	787
La	18.8	18.5	30.9	60.4	38.2	12.3	21.2	68.1	17.3	51	10	25.9	10.2	24.3
Ce	37	41.2	48	85.9	74.8	24.4	38.4	110	28.4	124.5	24.9	48.2	38.5	58.7
Pr	4.11	4.21	4.73	8.29	9.52	3.05	3.93	10.1	2.77	13.15	2.82	4.63	2.6	4.68
Nd	14.9	15.7	15.9	26.2	39.3	12.7	13.6	31.3	9.03	47.8	12.7	15.3	9.5	15
Sm	2.34	2.3	2.3	3.36	8.36	3	2.22	3.82	1.46	8.39	4.29	2.14	1.79	2.59
Eu	0.71	0.64	1.05	1.05	2.16	1.91	0.648	1.08	0.749	1.72	1.56	0.34	0.46	0.64
Gd	1.72	1.69	1.6	2.14	7.73	3.39	1.57	2.33	1.07	6.67	0.68	1.38	1.34	2.74
Tb	0.25	0.25	0.196	0.247	1.22	0.599	0.2	0.27	0.13	0.85	0.084	0.15	0.19	0.5
Dy	1.21	1.26	0.847	1.00	6.98	4.1	0.94	1.29	0.69	4.47	0.40	0.47	1.02	3.22
Ho	0.21	0.22	0.141	0.164	1.36	0.924	0.17	0.24	0.12	0.74	0.074	0.08	0.2	0.67
Er	0.61	0.63	0.346	0.401	3.65	2.85	0.44	0.7	0.36	1.86	0.18	0.18	0.56	2.05
Tm	0.09	0.11	0.0449	0.0496	0.53	0.477	0.063	0.108	0.051	0.26	0.031	0.03	0.07	0.31
Yb	0.55	0.59	0.289	0.325	3.44	3.54	0.4	0.67	0.32	1.64	1.6	0.24	0.51	1.99
Lu	0.08	0.09	0.0495	0.0534	0.521	0.607	0.061	0.109	0.049	0.23	0.026	0.05	0.07	0.31
Hf	3.7	4.3	3.61	4.41	8.27	11.9	3.1	5.2	2.4	5.1	9.97	2.6	3	5.2
Ta	0.3	0.4	0.075	0.124	0.802	1.12	0.52	0.44	0.45	0.6	0.28	0.2	0.6	0.3
Th	3.8	4.4	3.51	12.0	2.49	6.45	4.21	17.2	1.93	13.4	6.57	11.4	4.2	11.2
U	0.6	0.6	0.331	0.426	0.879	1.16	0.52	0.87	0.45	1.1	1.59	1.0	1.1	0.5

Zircon U-Pb chronology

Zircon U-Pb dating was done on samples from the Acasta Gneiss Complex and the Tartôq Greenstone Belt; zircon U-Pb data for the samples from Isua and the Bastar Craton were previously published (Sprung *et al.*, 2016; Maltese *et al.*, 2017). Zircon grains were separated from the rocks through crushing, followed by heavy liquid (CH_3I) and magnetic separation. Selected grains were mounted in epoxy, polished carefully, and subjected to cathodoluminescence (CL) imaging using a Philips *XL30* scanning electron microscope equipped with a Robinson CL detector. For Acasta Gneiss samples, special care was taken to expose inclusions and leave these intact upon removal of surface carbon. Zircon grains or grain domains were then subjected to U-Pb dating by laser ablation inductively coupled plasma mass spectrometry (LA-ICPMS) at the Pacific Centre for Isotopic and Geochemical Research, University of British Columbia, using an ESI *NWR193UC* ArF excimer laser ablation system coupled to a Thermo Finnigan *Element2* ICPMS instrument. Spots of 25 µm were ablated for 30 s using a laser fluence of approximately 4.5 J/cm^2 and a pulse rate of 6 Hz. The zircon reference material *GJ-1* (Jackson *et al.*, 2004) was used as a primary reference material. All data were reduced following a protocol outlined by Kooijman *et al.* (2012), which employs intercept-based corrections for time-dependent Pb/U fractionation during analysis (Sylvester and Ghaderi, 1997). Corrections for inherited Pb were done using the Pb-evolution model of Stacey and Kramers (1975). Accuracy was monitored through repeated analyses of the *FC-1* zircon (1,099.0 ± 0.6 Ma; Paces and Miller, 1993). We obtained 1,107 ± 17 Ma (MSWD = 1.05, n = 21; data provided in Table S-8) for this reference material through the course of our analytical sessions, demonstrating accuracy within acceptable levels of 1 %RSD or better. Analytical uncertainty equivalent to the external reproducibility of repeated analyses of the primary reference material *GJ-1* was propagated. Concordia diagrams and weighted mean ages were obtained using *ISOPLOT v*. 3.27 (Ludwig, 2003). All U-Pb data are provided in the Figures S-4 and S-5, and in Table S-9.

Table S-8 U-Pb data for the *FC-1* zircon reference. Outlier in grey.

Analysis	[U]*	Common Pb	Ratios						ρ†	Ages (Ma)						Concordance‡
	(ppm)	$^{206}Pb/^{204}Pb$	$^{207}Pb/^{235}U$	±2σ	$^{206}Pb/^{238}U$	±2σ	$^{207}Pb/^{206}Pb$	±2σ		$^{206}Pb/^{238}U$	±2σ	$^{207}Pb/^{235}U$	±2σ	$^{207}Pb/^{206}Pb$	±2σ	(%)
FC-1-01	278	^{204}Pb < DL	1.89	0.45	0.183	0.043	0.075	0.0026	0.99	1083	233	1078	158	1069	71	101
FC-1-02	321	^{204}Pb < DL	1.80	0.10	0.164	0.006	0.080	0.0032	0.67	976	32	1046	35	1194	78	82
FC-1-03	319	5195	1.90	0.21	0.181	0.018	0.076	0.0038	0.89	1075	96	1081	73	1094	100	98
FC-1-04	185	^{204}Pb < DL	1.95	0.11	0.178	0.006	0.079	0.0036	0.58	1058	31	1100	37	1183	89	89
FC-1-05	202	1583	2.02	0.14	0.192	0.008	0.076	0.0044	0.57	1134	42	1123	48	1101	115	103
FC-1-06	181	^{204}Pb < DL	1.93	0.09	0.183	0.004	0.076	0.0033	0.48	1086	23	1093	33	1107	86	98
FC-1-07	364	^{204}Pb < DL	1.88	0.14	0.178	0.010	0.077	0.0036	0.78	1057	57	1076	50	1112	94	95
FC-1-08	230	^{204}Pb < DL	1.63	0.09	0.159	0.005	0.074	0.0034	0.58	952	29	983	36	1051	92	91
FC-1-09	233	2185	2.03	0.10	0.189	0.006	0.078	0.0031	0.60	1115	31	1126	34	1147	80	97
FC-1-10	238	^{204}Pb < DL	2.05	0.08	0.195	0.004	0.076	0.0026	0.53	1149	23	1133	28	1101	69	104
FC-1-11	182	^{204}Pb < DL	2.08	0.16	0.189	0.010	0.080	0.0044	0.68	1117	53	1143	52	1192	110	94
FC-1-12	116	^{204}Pb < DL	1.90	0.19	0.181	0.013	0.076	0.0053	0.71	1071	69	1082	66	1103	139	97
FC-1-13	127	2436	1.87	0.13	0.176	0.004	0.077	0.0049	0.34	1044	22	1072	44	1130	125	92
FC-1-14	157	1270	1.77	0.14	0.166	0.006	0.077	0.0053	0.49	989	35	1033	51	1128	138	88
FC-1-15	153	1756	2.08	0.16	0.205	0.014	0.074	0.0028	0.87	1200	73	1142	53	1033	76	116
FC-1-16	150	^{204}Pb < DL	2.06	0.12	0.197	0.007	0.076	0.0035	0.59	1157	36	1136	39	1097	92	105
FC-1-17	259	2181	1.94	0.10	0.182	0.004	0.077	0.0036	0.42	1080	22	1093	35	1121	93	96
FC-1-18	*140*	*^{204}Pb < DL*	*2.66*	*0.23*	*0.258*	*0.014*	*0.075*	*0.0050*	*0.64*	*1479*	*74*	*1316*	*64*	*1060*	*135*	*140*
FC-1-19	155	^{204}Pb < DL	2.31	0.15	0.212	0.008	0.079	0.0041	0.57	1241	40	1216	45	1172	102	106
FC-1-20	188	^{204}Pb < DL	1.78	0.19	0.173	0.014	0.075	0.0048	0.79	1031	79	1038	68	1055	131	98
FC-1-21	194	2233	1.98	0.14	0.189	0.011	0.076	0.0029	0.83	1116	58	1109	46	1096	77	102

*Concentration uncertainty ca. 5%.

†Correlation coefficient.

‡The ratio of the $^{206}Pb/^{238}U$ age over the ^{207}Pb-^{206}Pb age.

Table S-9 U-Pb data for zircon from the Tartôq Greenstone Belt and Acasta Gneiss Complex. [1]Concentration uncertainty ca. 5%; [2]Correlation coefficient; [3]the ratio of the $^{206}Pb/^{238}U$ age over the ^{207}Pb-^{206}Pb age; outlier in grey.

Analysis	[U]*	Common Pb	Ratios						ρ†	Ages (Ma)						Concordance‡
	(ppm)	$^{206}Pb/^{204}Pb$	$^{207}Pb/^{235}U$	±2σ	$^{206}Pb/^{238}U$	±2σ	$^{207}Pb/^{206}Pb$	±2σ		$^{206}Pb/^{238}U$	±2σ	$^{207}Pb/^{235}U$	±2σ	$^{207}Pb/^{206}Pb$	±2σ	(%)
Tartôq Greenstone Belt																
468623																
GLZ1-468623_01	652	^{204}Pb < DL	17.22	0.58	0.609	0.016	0.206	0.0035	0.53	2864	27	3061	65	2943	32	107
GLZ1-468623_02	654	^{204}Pb < DL	10.30	0.36	0.321	0.009	0.233	0.0044	0.51	3062	31	1793	43	2459	32	59
GLZ1-468623_03	244	^{204}Pb < DL	16.31	0.56	0.572	0.015	0.206	0.0035	0.70	2864	28	2915	65	2894	33	102
GLZ1-468623_04	641	^{204}Pb < DL	8.17	0.34	0.290	0.011	0.202	0.0036	0.87	2840	30	1643	51	2246	37	58
GLZ1-468623_06	205	^{204}Pb < DL	16.49	0.56	0.579	0.015	0.205	0.0033	0.67	2861	26	2942	60	2901	33	103
GLZ1-468623_07	368	^{204}Pb < DL	16.14	0.54	0.580	0.015	0.201	0.0031	0.73	2829	25	2943	61	2881	32	104
GLZ1-468623_08	285	^{204}Pb < DL	13.13	0.47	0.467	0.014	0.203	0.0033	0.84	2849	26	2464	63	2682	34	86
GLZ1-468623_09b	294	^{204}Pb < DL	13.62	0.45	0.487	0.012	0.202	0.0031	0.68	2839	26	2554	52	2722	32	90
GLZ1-468623_13	458	^{204}Pb < DL	16.31	0.55	0.589	0.015	0.200	0.0032	0.70	2826	26	2987	63	2891	32	106
GLZ1-468623_14	252	^{204}Pb < DL	16.30	0.54	0.576	0.015	0.205	0.0034	0.57	2865	28	2929	61	2891	31	102
GLZ1-468623_15	241	^{204}Pb < DL	14.23	0.48	0.547	0.014	0.189	0.0031	0.69	2728	27	2810	59	2761	31	103
GLZ1-468623_16	540	^{204}Pb < DL	14.53	0.50	0.540	0.014	0.196	0.0033	0.65	2785	27	2778	60	2780	33	100
GLZ2-468623_01	190	^{204}Pb < DL	15.56	0.59	0.556	0.016	0.205	0.0044	0.60	2860	35	2844	66	2840	36	99
GLZ2-468623_02	226	^{204}Pb < DL	16.34	0.59	0.582	0.017	0.204	0.0039	0.67	2855	32	2956	67	2892	35	104
GLZ2-468623_03	393	^{204}Pb < DL	15.64	0.56	0.560	0.016	0.203	0.0040	0.64	2843	32	2868	65	2851	34	101
GLZ2-468623_04	675	^{204}Pb < DL	15.52	0.54	0.553	0.015	0.204	0.0036	0.59	2856	28	2835	61	2845	34	99
518001																
GLZ1-518001_01	946	^{204}Pb < DL	10.94	0.42	0.416	0.015	0.192	0.0052	0.68	2756	35	2239	69	2514	40	81
GLZ1-518001_02	318	^{204}Pb < DL	16.05	0.53	0.585	0.015	0.199	0.0033	0.66	2812	27	2970	63	2876	32	106
GLZ1-518001_03	376	^{204}Pb < DL	12.92	0.50	0.488	0.016	0.193	0.0033	0.84	2761	27	2558	67	2669	35	93
GLZ2-518001_01	302	^{204}Pb < DL	17.15	0.61	0.606	0.017	0.206	0.0042	0.60	2873	34	3055	69	2938	34	106
GLZ2-518001_02	261	^{204}Pb < DL	16.53	0.59	0.589	0.016	0.205	0.0041	0.43	2857	33	2987	64	2908	33	105
GLZ2-518001_03-1	196	^{204}Pb < DL	15.46	0.53	0.561	0.015	0.201	0.0041	0.31	2823	32	2870	61	2839	33	102
GLZ2-518001_03-2	258	^{204}Pb < DL	15.42	0.56	0.546	0.016	0.205	0.0041	0.58	2861	32	2807	65	2839	33	98
GLZ2-518001_04	299	^{204}Pb < DL	16.03	0.55	0.576	0.015	0.202	0.0035	0.63	2836	28	2929	64	2878	31	103
GLZ2-518001_06	144	^{204}Pb < DL	16.22	0.57	0.583	0.016	0.202	0.0037	0.63	2834	30	2955	65	2883	34	104
GLZ2-518001_07	201	^{204}Pb < DL	16.04	0.55	0.566	0.014	0.206	0.0036	0.56	2870	28	2889	59	2876	33	101
GLZ2-518001_08	195	^{204}Pb < DL	14.12	0.49	0.508	0.013	0.201	0.0037	0.57	2825	31	2647	59	2752	33	94
GLZ2-518001_09	303	^{204}Pb < DL	16.17	0.55	0.574	0.015	0.204	0.0038	0.51	2855	30	2922	62	2882	32	102

Analysis	[U]*	Common Pb	Ratios						ρ†	Ages (Ma)						Concordance‡
	(ppm)	$^{206}Pb/^{204}Pb$	$^{207}Pb/^{235}U$	±2σ	$^{206}Pb/^{238}U$	±2σ	$^{207}Pb/^{206}Pb$	±2σ		$^{206}Pb/^{238}U$	±2σ	$^{207}Pb/^{235}U$	±2σ	$^{207}Pb/^{206}Pb$	±2σ	(%)
GLZ2-518001_10	318	^{204}Pb < DL	16.15	0.54	0.568	0.015	0.206	0.0038	0.52	2868	30	2900	60	2882	32	101
GLZ2-518001_11	263	^{204}Pb < DL	17.22	0.60	0.615	0.017	0.203	0.0036	0.65	2846	30	3083	68	2944	33	108
GLZ1-518006_01	552	^{204}Pb < DL	15.63	0.54	0.559	0.015	0.204	0.0035	0.64	2858	29	2863	60	2851	34	100
GLZ1-518006_02	331	^{204}Pb < DL	15.34	0.79	0.568	0.024	0.196	0.0063	0.68	2791	53	2902	91	2829	41	104
GLZ1-518006_04	339	^{204}Pb < DL	15.15	0.53	0.564	0.016	0.198	0.0037	0.63	2796	31	2880	64	2821	36	103
GLZ1-518006_05	312	^{204}Pb < DL	16.20	0.57	0.595	0.017	0.200	0.0047	0.28	2809	33	3005	68	2886	32	107
GLZ1-518006_06a	437	^{204}Pb < DL	14.52	0.47	0.561	0.014	0.189	0.0028	0.63	2725	25	2870	57	2782	31	105
GLZ2-518006_01	231	^{204}Pb < DL	15.25	0.53	0.557	0.015	0.199	0.0038	0.60	2819	31	2850	63	2829	34	101
GLZ2-518006_02	191	^{204}Pb < DL	14.86	0.51	0.550	0.015	0.197	0.0041	0.47	2786	34	2819	64	2803	32	101
GLZ2-518006_03	237	^{204}Pb < DL	15.39	0.54	0.562	0.016	0.199	0.0038	0.61	2821	33	2873	67	2838	34	102
GLZ2-518006_06	1376	^{204}Pb < DL	10.76	0.38	0.394	0.013	0.207	0.0091	0.36	2842	49	2133	61	2501	34	75
GLZ2-518006_07	280	^{204}Pb < DL	13.65	0.53	0.497	0.016	0.200	0.0042	0.75	2813	34	2593	69	2714	38	92
GLZ2-518006_09	366	^{204}Pb < DL	15.89	0.55	0.580	0.016	0.200	0.0037	0.70	2819	29	2941	67	2864	34	104
GLZ2-518006_10	506	^{204}Pb < DL	15.83	0.55	0.568	0.015	0.203	0.0039	0.61	2843	31	2901	65	2863	34	102
GLZ2-518006_11	434	^{204}Pb < DL	14.91	0.50	0.538	0.014	0.202	0.0036	0.51	2830	29	2774	57	2806	32	98
GLZ2-518006_13	182	^{204}Pb < DL	15.97	0.58	0.569	0.016	0.204	0.0044	0.45	2843	35	2897	65	2868	34	102
GLZ2-518006_14	447	^{204}Pb < DL	15.78	0.56	0.578	0.016	0.198	0.0038	0.63	2807	32	2936	66	2857	35	105
GLZ2-518008_01	983	^{204}Pb < DL	12.68	0.45	0.485	0.014	0.473	0.1892	0.53	2545	29	2653	75	2746	34	93
GLZ2-518008_02	998	^{204}Pb < DL	11.07	0.39	0.443	0.012	0.373	0.1493	0.63	2355	32	2511	96	2628	47	90
GLZ2-518008_02	998	^{204}Pb < DL	11.69	0.41	0.457	0.013	0.472	0.1889	0.53	2416	30	2566	87	2693	50	90
GLZ2-518008_03	865	^{204}Pb < DL	14.99	0.53	0.557	0.016	0.514	0.2055	0.49	2850	31	2811	61	2778	35	103
GLZ2-518008_04	920	^{204}Pb < DL	13.99	0.49	0.517	0.014	0.312	0.1246	0.69	2681	29	2744	65	2798	25	96
GLZ2-518008_05	860	^{204}Pb < DL	14.77	0.52	0.541	0.015	0.241	0.0963	0.76	2783	29	2795	62	2807	27	99
GLZ2-518008_06	635	^{204}Pb < DL	13.04	0.46	0.490	0.014	0.348	0.1393	0.65	2568	29	2677	72	2758	47	93
GLZ2-518008_07	915	^{204}Pb < DL	15.76	0.56	0.584	0.016	0.496	0.1983	0.50	2960	31	2860	61	2786	19	106
GLZ2-518008_07	950	^{204}Pb < DL	12.53	0.44	0.467	0.013	0.129	0.0516	0.87	2465	30	2642	77	2780	18	89
GLZ2-518008_08	875	^{204}Pb < DL	15.53	0.55	0.574	0.016	0.438	0.1752	0.56	2918	31	2842	61	2804	42	104
GLZ2-518008_08	660	^{204}Pb < DL	15.89	0.56	0.588	0.016	0.205	0.0819	0.80	2994	31	2873	61	2795	31	107
508281																
GLZ1-508281_01	157	^{204}Pb < DL	16.42	0.55	0.585	0.015	0.205	0.0036	0.58	2861	28	2963	62	2898	33	104
GLZ1-508281_02	99	^{204}Pb < DL	18.30	0.63	0.637	0.017	0.209	0.0038	0.57	2890	30	3174	68	3000	34	110
GLZ1-508281_03	251	^{204}Pb < DL	17.58	0.59	0.623	0.016	0.205	0.0035	0.58	2864	27	3118	64	2967	31	109
GLZ1-508281_04	185	^{204}Pb < DL	17.47	0.59	0.608	0.016	0.210	0.0039	0.53	2900	32	3056	65	2958	33	105
GLZ1-508281_05	545	^{204}Pb < DL	15.85	0.54	0.566	0.015	0.205	0.0038	0.37	2857	30	2887	60	2865	31	101
GLZ1-508281_06	534	^{204}Pb < DL	18.29	0.62	0.627	0.016	0.213	0.0035	0.65	2925	27	3135	65	3001	33	107

Analysis	[U]*	Common Pb	Ratios						ρ†	Ages (Ma)						Concordance‡
	(ppm)	$^{206}Pb/^{204}Pb$	$^{207}Pb/^{235}U$	±2σ	$^{206}Pb/^{238}U$	±2σ	$^{207}Pb/^{206}Pb$	±2σ		$^{206}Pb/^{238}U$	±2σ	$^{207}Pb/^{235}U$	±2σ	$^{207}Pb/^{206}Pb$	±2σ	(%)
GLZ1-508281_08	391	^{204}Pb < DL	16.39	0.55	0.595	0.015	0.201	0.0034	0.61	2830	28	3008	60	2897	33	106
GLZ1-508281_02	314	^{204}Pb < DL	17.13	0.62	0.583	0.017	0.213	0.0046	0.57	2916	35	2954	69	2935	35	101
GLZ1-508281_03	436	^{204}Pb < DL	17.94	0.65	0.624	0.019	0.208	0.0045	0.62	2880	34	3119	75	2981	35	108
GLZ1-508281_04	224	^{204}Pb < DL	17.28	0.58	0.591	0.016	0.212	0.0041	0.48	2914	32	2991	64	2950	34	103
GLZ1-508281_05	240	^{204}Pb < DL	16.72	0.58	0.581	0.016	0.208	0.0039	0.62	2886	31	2946	67	2915	35	102
GLZ1-508281_06-1	313	^{204}Pb < DL	17.57	0.62	0.607	0.017	0.210	0.0041	0.57	2895	32	3051	67	2962	33	105
GLZ1-508281_06-2	266	^{204}Pb < DL	16.21	0.58	0.564	0.016	0.208	0.0046	0.38	2879	36	2880	66	2883	34	100
GLZ2-508281_07	352	^{204}Pb < DL	18.40	0.69	0.646	0.022	0.208	0.0140	0.60	2877	60	3211	95	3009	42	112
GLZ2-508281_08	611	^{204}Pb < DL	15.79	0.53	0.562	0.014	0.203	0.0036	0.43	2845	28	2873	60	2862	32	101
GLZ2-508281_09	183	^{204}Pb < DL	16.60	0.55	0.587	0.015	0.206	0.0034	0.46	2868	27	2976	60	2909	32	104
GLZ2-508281_11	231	^{204}Pb < DL	17.37	0.59	0.599	0.015	0.211	0.0038	0.48	2906	29	3022	63	2953	32	104
GLZ2-508281_12	294	^{204}Pb < DL	15.82	0.54	0.548	0.015	0.210	0.0039	0.56	2895	30	2819	60	2863	32	97
GLZ2-508281_13	150	^{204}Pb < DL	17.05	0.59	0.591	0.016	0.210	0.0043	0.44	2902	35	2989	66	2934	33	103
GLZ2-508281_14	166	^{204}Pb < DL	16.18	0.59	0.571	0.016	0.206	0.0043	0.62	2864	35	2910	69	2882	35	102
Acasta Gneiss Complex																
AMS001																
AMS001Big_BG2_001	820	41721	25.2	1.3	0.557	0.024	0.328	0.009	0.85	2854	101	3315	50	3607	41	79
AMS001Big_BG2_002	551	^{204}Pb < DL	27.9	1.6	0.556	0.029	0.364	0.010	0.89	2850	121	3415	58	3766	40	76
AMS001Big_BG2_003	400	4375	29.4	1.5	0.557	0.025	0.383	0.009	0.89	2853	102	3468	49	3845	34	74
AMS001Big_BG2_004	967	23387	12.4	2.9	0.360	0.084	0.250	0.007	0.99	1984	401	2638	225	3187	44	62
AMS001Big_BG2_005	687	147993	22.5	5.3	0.524	0.123	0.311	0.010	0.99	2716	520	3205	234	3528	50	77
AMS001Big_BG2_006	1972	20553	6.9	1.7	0.229	0.054	0.219	0.007	0.99	1327	286	2100	216	2976	50	45
AMS001Big_BG2_008	1454	9598	8.9	2.1	0.284	0.067	0.228	0.007	0.99	1611	337	2331	221	3039	48	53
AMS001Big_BG2_009	1067	^{204}Pb < DL	13.3	2.2	0.349	0.058	0.276	0.007	0.99	1931	277	2699	160	3339	43	58
AMS001Big_BG2_012	368	1575	32.4	5.4	0.575	0.095	0.408	0.011	0.99	2929	391	3562	167	3941	40	74
AMS001Big_BG2_013	1042	16377	19.8	3.3	0.447	0.075	0.322	0.008	0.99	2381	333	3082	165	3578	39	67
AMS001Big_BG2_014	466	2354	20.7	3.5	0.442	0.073	0.340	0.010	0.99	2358	328	3126	164	3664	43	64
AMS001Big_BG2_015	472	13447	22.3	3.8	0.485	0.082	0.333	0.010	0.98	2551	358	3195	169	3629	48	70
AMS001Big_BG2_016	1195	24509	18.3	1.0	0.472	0.018	0.282	0.010	0.72	2492	78	3008	50	3373	56	74
AMS001Big_BG2_020	1316	2356	8.4	0.5	0.242	0.011	0.252	0.009	0.79	1397	57	2274	52	3195	57	44
AMS001Big_BG2_021	1247	4189	13.5	0.7	0.420	0.015	0.234	0.008	0.72	2259	69	2718	47	3080	55	73
AMS001Big_BG2_022	1008	20822	12.3	0.7	0.386	0.016	0.231	0.009	0.72	2106	73	2628	53	3058	63	69
AMS001Big_BG2_024	1583	9395	12.9	1.3	0.355	0.029	0.263	0.014	0.85	1960	140	2673	92	3267	82	60
AMS001Big_BG2_025	925	6490	18.0	1.8	0.455	0.038	0.287	0.015	0.85	2417	170	2991	95	3404	81	71
AMS001Big_BG2_029	660	9684	21.2	2.2	0.456	0.039	0.337	0.019	0.84	2422	172	3147	99	3650	85	66

Analysis	[U]*	Common Pb	Ratios						ρ†	Ages (Ma)						Concordance‡
	(ppm)	$^{206}Pb/^{204}Pb$	$^{207}Pb/^{235}U$	±2σ	$^{206}Pb/^{238}U$	±2σ	$^{207}Pb/^{206}Pb$	±2σ		$^{206}Pb/^{238}U$	±2σ	$^{207}Pb/^{235}U$	±2σ	$^{207}Pb/^{206}Pb$	±2σ	(%)
AMS001Big_BG2_030	580	9318	33.0	3.4	0.594	0.052	0.403	0.023	0.84	3007	208	3581	102	3919	85	77
AMS001Big_BG2_031	1257	17645	28.5	2.8	0.619	0.052	0.334	0.018	0.84	3105	206	3436	98	3635	81	85
AMS001Big_BG2_032	371	5164	14.7	1.6	0.436	0.043	0.244	0.012	0.90	2331	195	2794	105	3147	75	74
AMS001Big_BG2_033	668	3171	28.9	3.1	0.620	0.061	0.338	0.015	0.91	3110	242	3448	106	3652	67	85
AMS001Big_BG2_034	979	9824	14.8	1.7	0.367	0.038	0.293	0.013	0.92	2013	180	2802	108	3432	69	59
AMS001Big_BG2_036	1072	9350	16.0	1.7	0.401	0.040	0.290	0.012	0.92	2174	183	2879	103	3418	66	64
AMS001Big_BG2_037	836	8297	15.5	1.2	0.399	0.029	0.283	0.010	0.90	2163	132	2849	76	3378	53	64
AMS001Big_BG2_038	1043	8177	24.9	1.9	0.558	0.039	0.323	0.010	0.92	2859	163	3304	75	3586	47	80
AMS001Big_BG2_039	734	14300	16.4	1.5	0.344	0.027	0.346	0.013	0.90	1907	132	2903	85	3692	58	52
AMS001Big_BG2_040	764	8287	23.2	1.8	0.499	0.035	0.338	0.012	0.90	2609	151	3237	76	3654	53	71
AMS001Big_BG2_042	1674	43889	12.8	1.0	0.356	0.026	0.260	0.008	0.91	1964	122	2665	74	3250	50	60
AMS001Med_P5_001	1013	11160	16.7	0.9	0.409	0.015	0.297	0.011	0.72	2209	69	2918	49	3452	56	64
AMS001Med_P5_002	386	536994	26.0	1.2	0.574	0.016	0.328	0.013	0.58	2925	66	3345	47	3607	60	81
AMS001Med_P5_003	535	793972	32.6	1.4	0.713	0.018	0.332	0.012	0.56	3471	66	3570	43	3626	56	96
AMS001Med_P5_006	612	49200	29.1	1.3	0.629	0.016	0.336	0.013	0.54	3145	62	3459	45	3646	60	86
AMS001Med_P5_008	877	4583	23.2	1.0	0.554	0.014	0.304	0.011	0.57	2840	58	3236	43	3491	57	81
AMS001Med_P5_009	529	15019	35.6	1.6	0.694	0.019	0.371	0.014	0.60	3399	73	3654	45	3798	55	90
AMS001Med_P5_010	804	10270	29.2	1.9	0.625	0.027	0.339	0.016	0.66	3131	107	3461	64	3658	74	86
AMS001Med_P5_023	502	5660	22.2	1.4	0.530	0.023	0.303	0.015	0.67	2743	98	3192	63	3488	74	79
AMS001Med_P5_024	1154	58788	23.6	1.5	0.603	0.025	0.283	0.013	0.66	3043	100	3251	61	3382	74	90
AMS001Med_P5_025	1099	23559	20.2	1.3	0.483	0.021	0.303	0.015	0.66	2541	91	3100	63	3486	75	73
AMS001Med_P5_026	978	6120	20.1	1.0	0.460	0.020	0.316	0.007	0.89	2439	88	3094	47	3553	34	69
AMS001Med_P5_027	1278	5355	19.9	1.0	0.514	0.022	0.281	0.006	0.90	2675	95	3088	47	3370	33	79
AMS001Sm_P5_001	784	1567	38.9	1.9	0.716	0.031	0.394	0.009	0.88	3482	117	3743	49	3886	36	90
AMS001Rou_P5_001	933	^{204}Pb < DL	24.6	1.2	0.589	0.026	0.302	0.006	0.90	2985	104	3291	47	3483	32	86
AMS001Rou_P5_002	1547	32269	19.8	1.0	0.513	0.023	0.280	0.006	0.89	2668	96	3083	48	3366	36	79
AMS001Rou_P5_006	1253	8150	14.9	0.5	0.438	0.011	0.247	0.004	0.83	2342	51	2809	30	3164	27	74
AMS001Rou_P5_015	1099	14065	20.8	0.6	0.545	0.011	0.278	0.005	0.72	2802	46	3131	27	3350	30	84
AMS001Rou_P5_017	617	^{204}Pb < DL	28.6	0.9	0.597	0.012	0.348	0.008	0.67	3017	48	3440	29	3697	34	82
AMS001Rou_P5_021	837	488116	31.9	1.1	0.724	0.014	0.320	0.008	0.59	3510	53	3548	32	3570	41	98
AMS001Rou_P5_023	1211	5521	21.0	0.7	0.559	0.013	0.272	0.007	0.68	2864	55	3139	34	3320	41	86
AMS001Rou_P5_028	779	^{204}Pb < DL	39.1	1.0	0.716	0.014	0.396	0.007	0.75	3481	54	3748	26	3894	27	89
AMS001_bt13a	1013	3000	27.5	2.1	0.562	0.034	0.354	0.016	0.80	2876	141	3400	75	3725	70	77
AMS001_bt13b	1101	15581	37.2	2.5	0.846	0.045	0.319	0.013	0.79	3951	158	3700	67	3567	65	111
AMS001_bt13c	1407	979	21.0	1.5	0.415	0.024	0.367	0.015	0.81	2235	109	3139	69	3781	64	59
AMS001_bt13d	635	2894	40.4	3.0	0.745	0.044	0.394	0.017	0.81	3587	164	3782	73	3887	65	92

Analysis	[U]*	Common Pb	Ratios						ρ†	Ages (Ma)						Concordance‡
	(ppm)	$^{206}Pb/^{204}Pb$	$^{207}Pb/^{235}U$	±2σ	$^{206}Pb/^{238}U$	±2σ	$^{207}Pb/^{206}Pb$	±2σ		$^{206}Pb/^{238}U$	±2σ	$^{207}Pb/^{235}U$	±2σ	$^{207}Pb/^{206}Pb$	±2σ	(%)
AMS001_bt12a	358	5123	32.1	2.6	0.599	0.040	0.388	0.017	0.83	3026	162	3553	79	3865	67	78
AMS001_bt12b	1261	6622	29.6	2.0	0.695	0.036	0.309	0.013	0.78	3400	138	3474	66	3517	64	97
AMS001_bt12c	1369	12503	25.1	2.0	0.495	0.032	0.367	0.016	0.83	2592	139	3311	76	3780	65	69
AMS001_bt12d	799	1817	35.5	2.4	0.660	0.036	0.390	0.016	0.81	3265	139	3653	67	3872	60	84
AMS001_bt11a	921	^{204}Pb < DL	23.6	1.6	0.557	0.030	0.307	0.013	0.79	2856	123	3253	66	3508	64	81
AMS001_bt11b	275	1469	33.5	2.1	0.547	0.027	0.443	0.017	0.80	2814	114	3594	62	4063	56	69
AMS001_bt11c	393	2514	21.8	1.4	0.420	0.023	0.376	0.013	0.85	2261	105	3174	63	3817	53	59
AMS001_bt10a	421	1214	29.2	1.7	0.562	0.027	0.377	0.013	0.80	2873	110	3460	59	3820	54	75
AMS001_bt10b	492	1234	18.3	1.0	0.425	0.020	0.313	0.010	0.81	2281	89	3008	55	3537	51	64
AMS001_bt10c	764	341	19.8	1.2	0.492	0.023	0.292	0.011	0.78	2581	99	3081	58	3426	58	75
AMS001_bt10d	786	712	19.7	1.1	0.479	0.021	0.299	0.010	0.79	2522	91	3079	54	3465	53	73
AMS001_bt09a	743	^{204}Pb < DL	25.4	1.5	0.543	0.026	0.340	0.011	0.82	2797	108	3325	57	3661	51	76
AMS001_bt09b	866	22013	25.8	1.5	0.576	0.026	0.325	0.012	0.79	2932	108	3338	57	3592	56	82
AMS001_bt09c	279	16408	30.5	1.7	0.596	0.027	0.371	0.011	0.84	3013	110	3503	54	3796	45	79
AMS001_bt05a	605	108529	20.2	1.0	0.513	0.021	0.286	0.009	0.79	2668	89	3102	50	3397	49	79
AMS001_bt05b	578	23058	26.8	1.8	0.496	0.025	0.392	0.017	0.77	2595	110	3375	65	3878	64	67
AMS001_bt15a	918	1720	11.8	0.9	0.325	0.018	0.262	0.015	0.69	1816	87	2586	74	3260	90	56
AMS001_bt15b	214	2414	31.8	1.9	0.753	0.026	0.307	0.015	0.58	3617	96	3545	59	3505	75	103
AMS001_bt15c	235	6362	28.3	1.8	0.558	0.026	0.368	0.015	0.74	2858	107	3429	61	3782	63	76
AMS001_bt16a	612	9960	13.6	0.8	0.383	0.015	0.257	0.011	0.67	2091	69	2721	55	3229	68	65
AMS001_bt16b	1790	40790	11.2	0.6	0.351	0.013	0.232	0.009	0.70	1938	63	2541	50	3066	62	63
AMS030A-A																
AMS030AA_001	317	2187	36.3	1.8	0.772	0.035	0.341	0.008	0.88	3689	126	3676	50	3669	37	101
AMS030AA_003	1151	10552	29.6	1.5	0.703	0.032	0.305	0.007	0.89	3433	122	3473	51	3496	36	98
AMS030AA_004	1221	536	25.9	1.3	0.603	0.027	0.312	0.007	0.89	3040	108	3344	49	3531	35	86
AMS030AA_005	1036	^{204}Pb < DL	36.3	2.0	0.847	0.030	0.311	0.013	0.63	3956	105	3675	55	3525	67	112
AMS030AA_007	1437	20597	26.3	1.5	0.700	0.025	0.272	0.012	0.61	3420	93	3358	56	3320	71	103
AMS030AA_008	1715	16185	15.3	0.9	0.543	0.020	0.205	0.010	0.63	2794	85	2835	57	2865	76	98
AMS030AA_012	1520	13037	24.9	1.5	0.665	0.025	0.272	0.012	0.65	3285	98	3306	58	3319	70	99
AMS030AA_013	2165	7732	36.8	3.3	0.772	0.047	0.346	0.023	0.66	3689	169	3689	90	3688	104	100
AMS030AA_014	1183	49135	25.8	3.0	0.595	0.056	0.314	0.021	0.81	3011	225	3337	114	3540	105	85
AMS030AA_021	2223	2397	23.1	2.2	0.641	0.039	0.262	0.019	0.65	3194	152	3232	91	3256	112	98
AMS030AA_024	1389	98955	22.3	1.5	0.640	0.029	0.252	0.013	0.67	3190	114	3196	66	3200	80	100
AMS030AA_025	1435	2826	20.1	1.4	0.612	0.029	0.238	0.012	0.68	3080	117	3098	68	3110	81	99
AMS030AA_026a	1857	7482	19.2	1.4	0.536	0.027	0.259	0.014	0.69	2767	112	3051	70	3244	83	85

Analysis	[U]*	Common Pb	Ratios						ρ†	Ages (Ma)						Concordance‡
	(ppm)	$^{206}Pb/^{204}Pb$	$^{207}Pb/^{235}U$	±2σ	$^{206}Pb/^{238}U$	±2σ	$^{207}Pb/^{206}Pb$	±2σ		$^{206}Pb/^{238}U$	±2σ	$^{207}Pb/^{235}U$	±2σ	$^{207}Pb/^{206}Pb$	±2σ	(%)
AMS030AA_026b	390	2402	33.3	2.3	0.708	0.034	0.341	0.018	0.68	3451	127	3591	69	3669	78	94
AMS030AA_028a	1489	635	15.7	1.0	0.483	0.020	0.235	0.012	0.65	2540	88	2856	62	3088	79	82
AMS030AA_028b	137	2544	27.3	1.8	0.624	0.026	0.318	0.016	0.65	3125	105	3396	64	3560	76	88
AMS030AA_030a	1216	^{204}Pb < DL	27.3	2.9	0.595	0.046	0.333	0.024	0.73	3011	187	3396	104	3631	111	83
AMS030AA_030b	346	9775	26.3	1.4	0.653	0.019	0.292	0.013	0.56	3240	76	3358	52	3430	69	94
AMS030AA_031	1152	23645	34.8	4.0	0.706	0.041	0.358	0.036	0.51	3442	156	3633	115	3740	153	92
AMS030AA_032	973	683	32.5	1.4	0.729	0.020	0.323	0.011	0.62	3528	73	3565	43	3586	53	98
AMS030AA_033	1118	2087	12.3	0.7	0.373	0.017	0.240	0.009	0.79	2043	81	2631	55	3120	57	65
AMS030AA_034	1235	38212	34.3	2.9	0.723	0.032	0.344	0.024	0.53	3507	121	3619	83	3682	108	95
AMS030AA_037	1004	9937	27.0	1.6	0.639	0.022	0.306	0.014	0.60	3186	88	3383	57	3503	72	91
AMS030AA_038	1955	4584	15.0	1.0	0.522	0.018	0.209	0.012	0.52	2706	76	2818	63	2899	92	93
AMS030AA_040	825	3317	35.7	2.1	0.786	0.027	0.330	0.015	0.59	3738	97	3658	57	3615	71	103
AMS030AA_041	1755	5790	16.4	1.2	0.471	0.024	0.253	0.014	0.67	2490	104	2902	72	3202	89	78
AMS030AA_042	1829	3581	14.8	1.5	0.426	0.027	0.251	0.019	0.63	2289	122	2799	95	3191	122	72
AMS030AA_043	632	8470	38.7	2.8	0.745	0.038	0.377	0.019	0.71	3590	142	3739	72	3819	77	94
AMS030AA_044	1360	729	12.1	0.9	0.350	0.020	0.250	0.014	0.72	1937	94	2612	73	3187	86	61
AMS030AA_045	699	83034	38.8	3.0	0.815	0.044	0.345	0.019	0.70	3844	155	3741	76	3686	84	104
AMS030AA_046	1560	^{204}Pb < DL	30.0	2.5	0.626	0.044	0.348	0.017	0.83	3133	174	3488	83	3699	73	85
AMS030AA_049	593	51732	36.4	3.0	0.734	0.049	0.360	0.017	0.81	3548	181	3678	81	3749	73	95
AMS030AA_051	2129	6404	14.3	1.1	0.451	0.029	0.231	0.011	0.80	2398	127	2773	75	3058	76	78
AMS030AA_052	1817	17499	17.8	1.4	0.517	0.032	0.250	0.011	0.81	2687	136	2981	74	3187	72	84
AMS030AA_055a	558	129	14.4	1.1	0.390	0.026	0.267	0.010	0.87	2124	120	2774	72	3289	58	65
AMS030AA_055b	259	6503	26.0	1.9	0.585	0.037	0.322	0.010	0.89	2970	152	3346	70	3580	49	83
AMS030AA_056	954	9696	34.4	2.4	0.723	0.045	0.345	0.011	0.89	3509	168	3623	69	3687	49	95
AMS030AA_059	688	7698	31.3	2.1	0.662	0.040	0.342	0.010	0.90	3276	155	3527	66	3673	45	89
AMS030AA_063	376	4382	33.8	2.3	0.699	0.042	0.351	0.011	0.89	3415	158	3604	66	3711	47	92
AMS030AA_068	394	^{204}Pb < DL	32.1	2.1	0.717	0.033	0.325	0.016	0.69	3483	125	3554	66	3595	74	97
AMS030AA_071	646	1607	37.9	2.5	0.770	0.036	0.357	0.016	0.71	3682	131	3717	65	3736	70	99
AMS030AA_074	236	808	37.9	2.5	0.752	0.034	0.366	0.018	0.68	3616	123	3718	65	3774	74	96
AMS030AA_086	1627	14306	13.0	0.9	0.394	0.019	0.239	0.011	0.71	2141	86	2678	62	3112	74	69
AMS030AA_088	268	1441675	36.5	2.5	0.687	0.019	0.385	0.024	0.42	3372	74	3680	67	3852	92	88
AMS030AA_093	465	9056	23.5	1.6	0.567	0.018	0.300	0.018	0.47	2896	74	3247	66	3471	92	83
AMS030AA_097	626	2006	32.0	2.1	0.687	0.019	0.338	0.020	0.41	3372	71	3551	65	3655	93	92
AMS030AA_098	453	400	29.7	2.2	0.616	0.024	0.349	0.022	0.52	3095	94	3476	72	3704	95	84
AMS030AA_099	202	^{204}Pb < DL	36.6	2.5	0.730	0.023	0.364	0.022	0.46	3534	87	3683	68	3766	93	94
AMS030AA_102	379	2230	32.5	2.7	0.673	0.040	0.351	0.020	0.72	3317	155	3567	82	3710	88	89

Analysis	[U]*	Common Pb	Ratios						ρ†	Ages (Ma)						Concordance‡
	(ppm)	$^{206}Pb/^{204}Pb$	$^{207}Pb/^{235}U$	±2σ	$^{206}Pb/^{238}U$	±2σ	$^{207}Pb/^{206}Pb$	±2σ		$^{206}Pb/^{238}U$	±2σ	$^{207}Pb/^{235}U$	±2σ	$^{207}Pb/^{206}Pb$	±2σ	(%)
AMS030AA_108	75	^{204}Pb < DL	47.7	4.2	0.828	0.054	0.418	0.025	0.74	3889	191	3945	89	3974	91	98
AMS030AA_bt01a	1017	2097	16.2	1.1	0.389	0.021	0.303	0.013	0.78	2117	99	2891	67	3486	68	61
AMS030AA_bt01b	908	15336	23.1	1.5	0.591	0.026	0.283	0.013	0.69	2993	103	3231	61	3381	71	89
AMS030AA_bt02a	717	846	9.1	0.5	0.275	0.011	0.239	0.009	0.73	1568	57	2345	51	3113	61	50
AMS030AA_bt02b	138	757	20.6	1.8	0.525	0.031	0.285	0.019	0.68	2718	132	3120	86	3389	102	80
AMS030AA_bt02c	190	2453	17.6	1.3	0.439	0.018	0.291	0.017	0.56	2347	80	2968	69	3422	93	69
AMS030AA_bt03a	725	1008	12.4	1.0	0.370	0.016	0.244	0.015	0.57	2029	77	2638	72	3145	100	65
AMS030AA_bt03b	309	1591	29.0	2.0	0.643	0.025	0.326	0.019	0.56	3202	98	3452	68	3601	87	89
AMS030AA_bt03c	276	2360	21.2	1.6	0.477	0.023	0.322	0.019	0.63	2513	100	3146	75	3579	92	70
AMS030AA_bt81a	367	2211	31.3	1.8	0.663	0.028	0.343	0.013	0.74	3278	110	3530	57	3676	59	89
AMS030AA_bt81b	429	2100	38.9	2.4	0.734	0.035	0.384	0.015	0.76	3549	129	3743	61	3848	61	92
AMS030AA_bt20a	1353	9080	20.9	0.9	0.539	0.016	0.281	0.008	0.72	2779	66	3133	40	3368	45	83
AMS030AA_bt20b	767	3846	15.0	0.6	0.401	0.011	0.272	0.007	0.75	2173	52	2817	36	3316	39	66
AMS030AA_bt20c	1579	2888	13.1	0.6	0.367	0.014	0.259	0.007	0.81	2013	66	2685	45	3239	44	62
Pk8_AMS030AA_Ap03a	807	^{204}Pb < DL	32.4	1.9	0.690	0.033	0.340	0.012	0.80	3383	125	3562	58	3665	54	92
Pk8_AMS030AA_Ap03b	199	481	14.6	0.9	0.365	0.019	0.291	0.011	0.80	2004	88	2791	61	3423	60	59
Pk8_AMS030AA_Ap04a	569	48784	23.5	1.0	0.569	0.016	0.300	0.010	0.66	2904	66	3249	42	3469	49	84
Pk8_AMS030AA_Ap04b	537	5792	30.0	1.3	0.633	0.018	0.344	0.011	0.65	3162	69	3486	42	3679	49	86
AMS030C																
AMS030C_002	680	107517	30.5	2.0	0.708	0.031	0.312	0.016	0.66	3449	118	3502	66	3532	78	98
AMS030C_004	432	3622	25.0	1.3	0.537	0.017	0.338	0.014	0.60	2771	70	3308	51	3653	63	76
AMS030C_005	935	^{204}Pb < DL	22.3	1.1	0.561	0.016	0.288	0.012	0.56	2872	64	3198	48	3409	64	84
AMS030C_006	553	9501	28.0	1.4	0.643	0.019	0.316	0.013	0.60	3200	75	3419	49	3549	61	90
AMS030C_012	1887	6322	12.5	0.7	0.434	0.013	0.208	0.009	0.56	2323	57	2640	50	2892	71	80
AMS030C_013	754	3600	29.6	1.5	0.636	0.022	0.338	0.012	0.71	3174	88	3474	49	3652	53	87
AMS030C_014	1316	^{204}Pb < DL	21.8	1.0	0.561	0.015	0.282	0.011	0.55	2870	61	3176	46	3376	62	85
AMS030C_015	508	2913	22.8	1.1	0.586	0.020	0.282	0.010	0.70	2972	83	3218	48	3376	56	88
AMS030C_016	1564	37064	28.4	1.5	0.680	0.026	0.303	0.010	0.75	3343	102	3431	51	3484	53	96
AMS030C_018	780	23009	26.4	1.3	0.624	0.020	0.307	0.011	0.66	3127	79	3363	47	3507	56	89
AMS030C_020	691	5388	22.1	1.8	0.628	0.037	0.255	0.014	0.74	3142	147	3188	78	3217	86	98
AMS030C_021	303	5317	34.3	2.8	0.772	0.047	0.322	0.017	0.76	3687	171	3618	80	3580	81	103
AMS030C_022	447	11870	31.2	2.5	0.704	0.042	0.321	0.017	0.75	3436	158	3525	78	3576	80	96
AMS030C_024	1433	108838	27.3	2.1	0.759	0.044	0.261	0.013	0.75	3639	160	3393	76	3251	81	112
AMS030C_025	386	6495	31.6	1.8	0.719	0.026	0.319	0.013	0.65	3491	98	3538	55	3564	65	98
AMS030C_026	563	^{204}Pb < DL	30.6	1.6	0.697	0.022	0.318	0.014	0.60	3410	85	3506	53	3561	67	96

Analysis	[U]*	Common Pb	Ratios						ρ†	Ages (Ma)						Concordance‡
	(ppm)	$^{206}Pb/^{204}Pb$	$^{207}Pb/^{235}U$	±2σ	$^{206}Pb/^{238}U$	±2σ	$^{207}Pb/^{206}Pb$	±2σ		$^{206}Pb/^{238}U$	±2σ	$^{207}Pb/^{235}U$	±2σ	$^{207}Pb/^{206}Pb$	±2σ	(%)
AMS030C_027	698	4222	29.3	1.4	0.716	0.019	0.297	0.011	0.57	3479	72	3463	46	3454	59	101
AMS030C_029	1782	9580	26.6	2.0	0.716	0.034	0.269	0.016	0.63	3480	128	3367	74	3301	93	105
AMS030C_032	435	6390	30.5	1.4	0.697	0.018	0.318	0.012	0.56	3408	69	3503	46	3558	60	96
AMS030C_033	243	7055	30.2	1.7	0.689	0.027	0.318	0.013	0.69	3377	103	3495	56	3562	63	95
AMS030C_034	1031	4144	20.3	1.1	0.582	0.022	0.253	0.010	0.69	2958	92	3105	54	3201	64	92
AMS030C_035	1270	54567	22.0	1.3	0.562	0.026	0.284	0.011	0.75	2876	106	3183	59	3383	62	85
AMS030C_037	1950	15777	21.0	1.5	0.575	0.032	0.264	0.012	0.77	2930	130	3136	69	3271	71	90
AMS030C_038a	548	^{204}Pb < DL	22.3	1.4	0.547	0.024	0.296	0.014	0.68	2814	99	3199	62	3450	73	82
AMS030C_038b	77	602	23.9	2.0	0.547	0.030	0.317	0.019	0.68	2811	126	3263	80	3555	93	79
AMS030C_039	2080	20840	10.6	0.8	0.382	0.021	0.200	0.012	0.68	2088	96	2485	73	2829	94	74
AMS030C_041	571	5832	30.3	1.9	0.639	0.027	0.344	0.016	0.68	3186	106	3497	61	3681	70	87
AMS030C_045	292	7114	34.5	2.1	0.741	0.029	0.338	0.016	0.64	3574	107	3625	60	3653	71	98
AMS030C_046	2740	26005	16.3	1.2	0.517	0.026	0.228	0.012	0.70	2686	112	2892	69	3039	82	88
AMS030C_056	89	1531	22.5	2.3	0.368	0.032	0.443	0.022	0.86	2022	151	3207	98	4063	75	50
AMS030C_061	646	^{204}Pb < DL	23.3	2.3	0.580	0.044	0.292	0.019	0.76	2947	181	3241	98	3428	101	86
AMS030C_067	236	^{204}Pb < DL	37.8	2.8	0.683	0.037	0.401	0.020	0.74	3357	143	3715	74	3915	76	86
AMS030C_069	357	3473	26.1	1.8	0.632	0.033	0.299	0.014	0.74	3159	131	3349	69	3464	73	91
AMS030C_070	145	^{204}Pb < DL	44.3	3.0	0.769	0.040	0.418	0.019	0.75	3679	144	3872	68	3974	67	93
AMS030C_071	226	61089	35.1	2.5	0.676	0.037	0.376	0.017	0.77	3330	141	3640	70	3816	69	87
AMS030C_076	268	20631	30.2	2.1	0.576	0.032	0.380	0.017	0.78	2931	131	3492	70	3832	67	76
AMS030C_077	296	31879	34.0	2.4	0.725	0.040	0.340	0.015	0.78	3514	149	3610	70	3663	68	96
AMS030C_080	569	5323	30.8	3.2	0.635	0.054	0.352	0.021	0.82	3168	211	3514	101	3717	89	85
AMS030C_081	475	7754	25.5	2.6	0.618	0.053	0.299	0.017	0.83	3100	211	3327	102	3467	90	89
AMS030C_083	232	4874	39.5	4.1	0.714	0.061	0.402	0.023	0.82	3472	228	3759	102	3916	88	89
AMS030C_084	566	5529	30.2	3.1	0.657	0.056	0.334	0.019	0.83	3255	218	3494	102	3634	89	90
AMS030C_085	824	2487	30.4	2.1	0.647	0.036	0.341	0.014	0.81	3215	142	3500	68	3667	61	88
AMS030C_090	345	5114240	41.0	2.8	0.782	0.044	0.380	0.014	0.83	3725	160	3795	68	3832	58	97
AMS030C_091	426	10293	29.5	2.0	0.648	0.037	0.330	0.013	0.83	3221	143	3470	67	3617	58	89
AMS030C_092	287	21821	33.4	2.3	0.708	0.040	0.342	0.013	0.83	3451	152	3591	68	3671	58	94
AMS030C_095	589	113484	41.8	2.8	0.777	0.043	0.391	0.014	0.84	3706	157	3815	66	3873	54	96
AMS030C_097a	483	40	10.3	0.8	0.317	0.019	0.236	0.011	0.79	1774	93	2461	70	3091	75	57
AMS030C_097b	146	551	24.9	1.6	0.608	0.035	0.297	0.007	0.92	3062	141	3305	61	3456	37	89
AMS030C_099	485	69921	30.2	2.0	0.678	0.041	0.323	0.009	0.91	3338	157	3493	65	3584	41	93
AMS030C_101	290	5317	35.5	2.3	0.726	0.043	0.355	0.009	0.91	3520	160	3653	64	3727	41	94
AMS030C_104	231	^{204}Pb < DL	32.7	2.2	0.696	0.042	0.341	0.010	0.91	3406	160	3572	66	3666	43	93
AMS030C_105	460	^{204}Pb < DL	40.0	2.5	0.877	0.051	0.330	0.006	0.95	4059	176	3770	61	3619	30	112

Analysis	[U]*	Common Pb	Ratios						ρ†	Ages (Ma)						Concordance‡
	(ppm)	$^{206}Pb/^{204}Pb$	$^{207}Pb/^{235}U$	±2σ	$^{206}Pb/^{238}U$	±2σ	$^{207}Pb/^{206}Pb$	±2σ		$^{206}Pb/^{238}U$	±2σ	$^{207}Pb/^{235}U$	±2σ	$^{207}Pb/^{206}Pb$	±2σ	(%)
AMS030c_bt65a	203	70666	37.5	2.9	0.658	0.028	0.414	0.026	0.55	3258	107	3707	76	3960	96	82
AMS030c_bt65b	329	^{204}Pb < DL	38.5	3.0	0.686	0.028	0.408	0.027	0.53	3365	108	3734	77	3938	98	85
AMS031A																
AMS031A4Bpris_BG2_029	397	^{204}Pb < DL	37.8	2.0	0.811	0.028	0.338	0.014	0.65	3828	101	3715	53	3654	62	105
AMS031A4Bpris_BG2_031	436	^{204}Pb < DL	32.4	1.7	0.688	0.025	0.341	0.012	0.71	3377	97	3562	51	3668	55	92
AMS031A4Bpris_BG2_032	556	43862	30.5	1.7	0.630	0.025	0.352	0.014	0.71	3148	99	3504	55	3715	60	85
AMS031A4Bpris_BG2_033	518	10759	32.6	1.9	0.655	0.028	0.361	0.015	0.72	3248	108	3569	58	3754	61	87
AMS031A4Bpris_BG2_036	589	18901	26.5	1.6	0.564	0.025	0.341	0.013	0.76	2883	104	3366	58	3667	58	79
AMS031A4Bpris_BG2_037	577	^{204}Pb < DL	28.1	1.7	0.566	0.026	0.360	0.014	0.75	2892	106	3422	59	3749	60	77
AMS031A4Brou_BG2_003	69	^{204}Pb < DL	28.6	2.3	0.580	0.033	0.358	0.021	0.70	2948	135	3441	80	3742	88	79
AMS031A4Brou_BG2_004	111	1953	22.1	1.4	0.490	0.022	0.328	0.014	0.73	2569	96	3190	60	3608	64	71
AMS031A4Brou_BG2_005a	45	^{204}Pb < DL	22.0	1.4	0.443	0.021	0.360	0.015	0.74	2364	93	3183	62	3750	65	63
AMS031A4Brou_BG2_005b	243	12113	16.8	1.4	0.374	0.026	0.325	0.014	0.84	2050	120	2923	78	3595	67	57
AMS031A4Brou_BG2_010a	544	17550	24.5	1.2	0.523	0.019	0.340	0.012	0.72	2713	79	3289	48	3661	53	74
AMS031A4Brou_BG2_010b	62	2726	25.9	1.6	0.511	0.023	0.367	0.015	0.76	2662	99	3342	59	3779	60	70
AMS031A4Brou_BG2_011	371	17540	14.7	0.8	0.404	0.018	0.263	0.009	0.78	2188	83	2794	55	3266	56	67
AMS031A4Brou_BG2_012	604	63808	21.1	1.4	0.442	0.019	0.346	0.017	0.68	2358	87	3141	63	3689	73	64
AMS031A4Brou_BG2_015	392	112286	21.8	1.6	0.443	0.025	0.357	0.018	0.74	2363	110	3175	73	3738	77	63
AMS031A4Brou_BG2_016	51	^{204}Pb < DL	25.6	1.7	0.528	0.024	0.352	0.017	0.68	2735	99	3332	64	3715	73	74
AMS031A4Brou_BG2_020	68	5535	22.5	1.4	0.536	0.019	0.304	0.015	0.57	2767	78	3205	59	3492	77	79
AMS031A4Brou_BG2_021	682	^{204}Pb < DL	20.6	1.4	0.447	0.019	0.334	0.017	0.66	2381	86	3119	64	3636	76	65
AMS031A4Brou_BG2_023	60	2413	23.6	2.0	0.481	0.033	0.356	0.019	0.79	2533	143	3252	85	3732	81	68
AMS031A4Brou_BG2_034	54	1027	25.7	1.8	0.525	0.026	0.356	0.018	0.71	2719	111	3337	69	3732	76	73
AMS031A4Brou_BG2_035	200	10288	12.6	0.9	0.407	0.022	0.224	0.011	0.75	2202	101	2647	68	3007	78	73
AMS031A4Brou_BG2_039	54	^{204}Pb < DL	21.9	1.8	0.444	0.029	0.357	0.019	0.78	2370	130	3180	81	3739	79	63
AMS031A4Brou_BG2_040	683	^{204}Pb < DL	27.1	1.5	0.551	0.027	0.356	0.009	0.90	2829	113	3386	54	3735	37	76
AMS031A4Brou_BG2_045	65	^{204}Pb < DL	23.3	1.3	0.469	0.023	0.360	0.008	0.90	2481	100	3240	53	3750	36	66
AMS031A8Med_P5_001	542	78838	38.6	2.8	0.805	0.044	0.347	0.016	0.75	3809	156	3735	72	3695	72	103
AMS031A8Med_P5_002	483	^{204}Pb < DL	35.8	2.5	0.761	0.041	0.342	0.015	0.77	3647	150	3662	69	3670	69	99
AMS031A8Med_P5_004	415	9185	39.5	2.8	0.832	0.045	0.344	0.016	0.77	3902	159	3758	70	3682	70	106
AMS031A8Med_P5_006	126	1943	37.7	2.7	0.793	0.043	0.345	0.016	0.76	3764	154	3712	70	3685	70	102
AMS031A8Med_P5_008	594	129423	31.7	2.3	0.679	0.039	0.339	0.015	0.78	3339	149	3542	72	3659	70	91
AMS031A8Med_P5_014	612	6390	37.7	1.6	0.768	0.024	0.356	0.011	0.72	3673	89	3712	43	3733	46	98
AMS031A8Med_P5_020	359	12485	36.3	1.4	0.755	0.022	0.349	0.009	0.74	3625	80	3675	38	3703	40	98
AMS031A8Med_P5_021	398	7435	34.4	1.3	0.713	0.020	0.350	0.009	0.73	3468	77	3621	39	3706	41	94

Analysis	[U]*	Common Pb	Ratios						ρ†	Ages (Ma)						Concordance‡
	(ppm)	$^{206}Pb/^{204}Pb$	$^{207}Pb/^{235}U$	±2σ	$^{206}Pb/^{238}U$	±2σ	$^{207}Pb/^{206}Pb$	±2σ		$^{206}Pb/^{238}U$	±2σ	$^{207}Pb/^{235}U$	±2σ	$^{207}Pb/^{206}Pb$	±2σ	(%)
AMS031A8_bt25a	467	^{204}Pb < DL	28.6	1.7	0.649	0.030	0.319	0.012	0.78	3224	116	3439	58	3567	57	90
AMS031A8_bt25b	464	^{204}Pb < DL	31.1	2.1	0.720	0.022	0.313	0.019	0.44	3497	81	3521	66	3535	93	99
AMS031A8Brou_BG1_002	162	^{204}Pb < DL	28.0	2.1	0.618	0.035	0.328	0.015	0.77	3104	141	3419	73	3610	72	86
AMS031A8Brou_BG1_003	300	122375	27.7	2.0	0.635	0.035	0.316	0.014	0.77	3168	140	3407	71	3551	70	89
AMS031A8Brou_BG1_007	57	^{204}Pb < DL	28.1	2.1	0.614	0.036	0.332	0.016	0.78	3086	145	3421	74	3624	72	85
AMS031A8Brou_BG1_008	424	31048	32.2	2.0	0.685	0.028	0.342	0.016	0.66	3362	105	3558	60	3670	70	92
AMS031A8Brou_BG1_009	919	5692	32.5	2.1	0.737	0.030	0.319	0.016	0.62	3560	113	3564	65	3567	79	100
AMS031A8Brou_BG1_013	238	^{204}Pb < DL	26.6	1.7	0.637	0.026	0.303	0.014	0.65	3177	101	3370	61	3487	73	91
AMS031A8Brou_BG1_014	47	1208	30.8	2.0	0.659	0.029	0.339	0.016	0.67	3264	111	3512	64	3657	74	89
AMS031A8Brou_BG1_017	168	7019	28.5	1.9	0.611	0.028	0.339	0.017	0.69	3073	114	3438	67	3658	75	84
AMS031A8Brou_BG1_022	265	^{204}Pb < DL	28.2	2.6	0.612	0.043	0.334	0.020	0.76	3077	173	3425	91	3635	93	85
AMS031A8Brou_BG1_023	85	^{204}Pb < DL	22.9	2.1	0.544	0.038	0.306	0.019	0.76	2800	160	3223	91	3499	94	80
AMS031A8Brou_BG1_026a	876	20503	26.6	2.5	0.626	0.044	0.308	0.019	0.75	3133	174	3368	91	3511	94	89
AMS031A8Brou_BG1_026b	61	^{204}Pb < DL	24.7	2.3	0.578	0.040	0.310	0.019	0.75	2939	166	3297	92	3522	97	83
AMS031A8Brou_BG1_027	563	^{204}Pb < DL	30.9	3.0	0.666	0.052	0.337	0.020	0.80	3290	201	3516	97	3648	91	90
AMS031A8Brou_BG1_028	131	^{204}Pb < DL	28.6	2.7	0.636	0.048	0.326	0.019	0.80	3172	191	3440	94	3599	89	88
AMS031A8Brou_BG1_030	165	2868	28.2	2.8	0.607	0.048	0.337	0.020	0.80	3059	191	3427	96	3650	89	84
AMS031A8Brou_BG1_032	46	1466	30.5	2.9	0.647	0.049	0.342	0.020	0.79	3215	193	3502	95	3671	89	88
AMS031A8Brou_BG1_033	172	4596	30.0	2.9	0.648	0.050	0.335	0.020	0.80	3222	197	3486	96	3642	89	88
AMS031A8Pr_BG1_001	438	20423	25.0	1.6	0.545	0.019	0.333	0.018	0.53	2805	78	3309	63	3630	84	77
AMS031A8Pr_BG1_003	405	16665	30.8	2.0	0.645	0.018	0.347	0.020	0.45	3209	72	3514	63	3692	87	87
AMS031A8Pr_BG1_005	453	17640	26.5	1.7	0.578	0.017	0.332	0.019	0.46	2939	69	3364	62	3627	86	81
AMS031A8Pr_BG1_006	482	115039	35.9	2.4	0.756	0.026	0.345	0.019	0.52	3629	94	3665	65	3685	86	98
AMS031A8Pr_BG1_007	40	12433	28.2	2.2	0.574	0.037	0.356	0.016	0.83	2924	151	3427	76	3735	67	78
AMS031A8Pr_BG1_008	478	^{204}Pb < DL	29.8	2.2	0.605	0.038	0.357	0.015	0.84	3050	153	3479	74	3736	62	82
AMS031A8Pr_BG1_010	72	^{204}Pb < DL	31.6	2.4	0.654	0.042	0.351	0.014	0.85	3245	163	3539	75	3710	62	87
AMS031A8Pr_BG1_011	467	42639	23.7	1.7	0.554	0.034	0.311	0.012	0.85	2842	143	3258	72	3525	60	81
AMS031A8Pr_BG1_014	544	30877	28.9	2.2	0.669	0.041	0.313	0.013	0.83	3303	160	3451	73	3537	64	93
AMS031A8Pr_BG1_014	81	^{204}Pb < DL	29.3	2.0	0.604	0.020	0.352	0.021	0.49	3045	82	3465	67	3718	91	82
AMS031A8Pr_BG1_015	619	^{204}Pb < DL	36.4	2.4	0.787	0.027	0.335	0.019	0.51	3742	97	3677	66	3642	88	103
AMS031A8Pr_BG1_019	44	1942	30.3	2.1	0.658	0.021	0.334	0.020	0.47	3259	82	3497	67	3637	92	90
AMS031A8Pr_BG1_020	692	22588	33.0	2.1	0.715	0.022	0.335	0.019	0.48	3479	84	3581	64	3638	87	96
AMS031A8Pr_BG1_021	452	4807	30.9	2.3	0.660	0.040	0.340	0.015	0.81	3265	155	3516	73	3662	66	89
AMS031A8Pr_BG1_022	377	^{204}Pb < DL	32.5	2.6	0.679	0.044	0.347	0.016	0.81	3342	168	3564	79	3692	72	91
AMS031A8Pr_BG1_026	541	6209165	33.4	2.5	0.732	0.045	0.331	0.015	0.81	3541	168	3593	75	3622	68	98
AMS031A8Pr_BG1_027	426	^{204}Pb < DL	23.3	1.8	0.582	0.036	0.291	0.013	0.81	2956	146	3241	74	3423	70	86

Analysis	[U]*	Common Pb	Ratios						ρ†	Ages (Ma)						Concordance‡
	(ppm)	$^{206}Pb/^{204}Pb$	$^{207}Pb/^{235}U$	±2σ	$^{206}Pb/^{238}U$	±2σ	$^{207}Pb/^{206}Pb$	±2σ		$^{206}Pb/^{238}U$	±2σ	$^{207}Pb/^{235}U$	±2σ	$^{207}Pb/^{206}Pb$	±2σ	(%)
AMS031A8Pr_BG1_029	458	21835	32.7	2.4	0.711	0.043	0.334	0.014	0.81	3462	163	3573	74	3636	66	95
AMS031A8Pr_BG1_030	552	^{204}Pb < DL	33.3	2.4	0.726	0.050	0.332	0.007	0.95	3519	187	3589	71	3628	34	97
AMS031A4Pr_BG2_001	660	29231	34.1	2.4	0.732	0.050	0.338	0.006	0.97	3541	187	3613	70	3653	26	97
AMS031A4Pr_BG2_002	642	12029	34.3	2.4	0.728	0.050	0.342	0.006	0.97	3528	186	3620	69	3671	25	96
AMS031A4Pr_BG2_004	774	^{204}Pb < DL	34.4	2.5	0.745	0.051	0.335	0.007	0.96	3589	189	3622	71	3640	31	99
AMS031A4Pr_BG2_005	592	73065	36.2	2.0	0.769	0.038	0.341	0.008	0.89	3679	137	3673	54	3669	37	100
AMS031A4Pr_BG2_006	206	82691	32.6	1.9	0.673	0.035	0.351	0.010	0.88	3318	133	3568	58	3712	43	89
AMS031A4Pr_BG2_007	606	320423	38.6	2.1	0.830	0.041	0.338	0.008	0.90	3896	144	3737	55	3652	38	107
AMS031A4Pr_BG2_009	516	15944	34.3	1.8	0.775	0.038	0.321	0.007	0.90	3700	137	3619	53	3575	35	103
AMS031A4Pr_BG2_010	82	^{204}Pb < DL	34.7	2.1	0.728	0.037	0.346	0.010	0.86	3524	139	3629	59	3688	46	96
AMS031A4Pr_BG2_012	647	41137	32.2	1.5	0.695	0.022	0.336	0.011	0.71	3402	85	3556	45	3644	49	93
AMS031A4Pr_BG2_015	615	23411	35.7	1.7	0.766	0.025	0.338	0.011	0.70	3665	91	3657	46	3652	51	100
AMS031A4Pr_BG2_017	704	30778	35.1	1.7	0.781	0.026	0.326	0.011	0.70	3721	93	3642	47	3598	52	103
AMS031A4Pr_BG2_018	545	^{204}Pb < DL	39.5	1.8	0.834	0.026	0.343	0.011	0.69	3909	92	3758	45	3678	49	106
AMS031A4Pr_BG2_019	547	10931	27.4	1.8	0.670	0.030	0.296	0.015	0.67	3305	115	3396	65	3451	76	96
AMS031A4Pr_BG2_024	618	^{204}Pb < DL	35.8	2.5	0.759	0.036	0.342	0.017	0.68	3640	130	3662	68	3673	77	99
AMS031A4Pr_BG2_026	971	127796	38.2	2.7	0.811	0.040	0.341	0.017	0.70	3830	141	3725	69	3669	77	104
AMS031A4Pr_BG2_027	447	^{204}Pb < DL	34.6	2.4	0.711	0.036	0.353	0.017	0.71	3463	134	3627	69	3718	75	93
AMS031A4Pr_BG2_028	421	^{204}Pb < DL	24.1	1.7	0.593	0.028	0.295	0.015	0.68	3003	113	3273	68	3444	79	87
AMS031A8Med_P5_014	612	6390	37.7	1.6	0.768	0.024	0.356	0.011	0.72	3673	89	3712	43	3733	46	98
AMS031A8Med_P5_020	359	12485	36.3	1.4	0.755	0.022	0.349	0.009	0.74	3625	80	3675	38	3703	40	98
AMS031A8Med_P5_021	398	7435	34.4	1.3	0.713	0.020	0.350	0.009	0.73	3468	77	3621	39	3706	41	94

*Concentration uncertainty ca. 5%.

†Correlation coefficient.

‡The ratio of the $^{206}Pb/^{238}U$ age over the ^{207}Pb-^{206}Pb age.

Supplementary Information References

Aignertorres, M., Blundy, J., Ulmer, P., Pettke, T. (2007) Laser Ablation ICPMS study of trace element partitioning between plagioclase and basaltic melts: an experimental approach. *Contributions to Mineralogy and Petrology* 153, 647-667.

Amelin, Y., Kamo, S.L., Lee, D.C. (2011) Evolution of early crust in chondritic or nonchondritic Earth inferred from U–Pb and Lu–Hf data for chemically abraded zircon from the Itsaq Gneiss Complex, West Greenland. *Canadian Journal of Earth Sciences* 48, 141–160.

Bacon, C.R., Druitt, T.H. (1988) Compositional Evolution of the Zoned Calcalkaline Magma Chamber of Mount-Mazama, Crater Lake, Oregon. *Contributions to Mineralogy and Petrology* 98, 224-256.

Bast, R., Scherer, E.E., Mezger, K., Austrheim, H., Ludwig, T., Marschall, H.R., Putnis, A., Löwen, K. (2014) Boron isotopes in tourmaline as a tracer of metasomatic processes in the Bamble sector of Southern Norway. *Contributions to Mineralogy and Petrology* 168, 1069.

Bennett, V.C., Nutman, A.P., McCulloch, M.T. (1993) Nd isotopic evidence for transient, highly depleted mantle reservoirs in the early history of the Earth. *Earth and Planetary Science Letters* 119, 299-317.

Bindeman, I.N., Davis, A.M., Drake, M.J. (1998) Ion microprobe study of plagioclase-basalt partition experiments at natural concentration levels of trace elements. *Geochimica et Cosmochimica Acta* 62, 1175-1193.

Bindeman, I., Davis, A. (2000) Trace element partitioning between plagioclase and melt: Investigation of dopant influence on partition behavior. *Geochimica et Cosmochimica Acta* 64, 2863-2878.

Bindemann, I.N., Eiler, J., Yogodzinski, G.M., Tatsumi, Y., Stern, C.R., Grove, T.L., Portnyagin, M., Hoernle, K., Danyushevsky, L.V. (2001) Oxygen isotope evidence for slab melting in modern and ancient subduction zones. *Earth and Planetary Science Letters* 235, 480-496.

Bowring, S.A., Williams, I.S., Compston, W. (1989) 3.96 Ga gneisses from the Slave Province, Northwest Territories, Canada. *Geology* 17, 971-975.

Bowring, S.A., Williams, I.S. (1999) Priscoan (4.00–4.03 Ga) orthogneisses from northwestern Canada. *Contributions to Mineralogy and Petrology* 134, 3-16.

Brandt, W.A., Coplen, T.B., Vogl, J., Rosner, M., Prohaska, T. (2014) Assessment of international reference materials for isotope-ratio analysis (IUPAC Technical Report). *Pure and Applied Chemistry* 86, 425-467.

Brenan, J.M., Shaw, H.F., Ryerson, F.J., Phinney, D.L. (1995) Experimental-Determination of Trace-Element Partitioning between Pargasite and a Synthetic Hydrous Andesitic Melt. *Earth and Planetary Science Letters* 135, 1-11.

Brenan, J.M., Neroda, E., Lundstrom, C.C., Shaw, H.F., Ryerson, F.J. and Phinney, D.L. (1998). Behaviour of boron, beryllium, and lithium during melting and crystallization: Constraints from mineral-melt partitioning experiments. *Geochimica et Cosmochimica Acta* 62, 2129-2141.

Cai, Y., Rasbury, T.E., Hemming, N.G., Chemical procedures for B-Sr-Nd-Pb-Hf isotopes and HFSE content analyses with a single rock dissolution using Na_2O_2. In preparation.

Chaussidon, M., Uitterdijk Appel, P.W. (1997) Boron isotopic composition of tourmalines from the 3.8 Ga-old Isua supracrustals, West Greenland: implications on the δ11B value of early Archean seawater. *Chemical Geology* 136, 171-180.

Deegan, F.M., Troll, V.R., Whitehouse, M.J., Jolis, E.M., Freda, C. (2016) Boron isotope fractionation in magma via crustal carbonate dissolution. *Scientific Reports* 6, 30774.

de Hoog, J.C.M., Savov, I.P. (2018) Boron isotopes as a tracer of subduction zone processes. In: Marschall, H.R., Foster, G.L. (Eds.) *Boron Isotopes – The Fifth Element, Advances in Isotope Geochemistry 6*. Springer, Heidelberg, 217-247.

Dunn, T. (1987) Partitioning of Hf, Lu, Ti, and Mn between olivine, clinopyroxene and basaltic liquid. *Contributions to Mineralogy and Petrology* 96, 476-484.

Elkins, L., Gaetani, G., Sims, K. (2008) Partitioning of U and Th during garnet pyroxenite partial melting: Constraints on the source of alkaline ocean island basalts. *Earth and Planetary Science Letters* 265, 270-286.

Emo, R.B., Smit, M.A., Schmitt, M., Kooijman, E., Scherer, E.E., Sprung, P., Bleeker, W., Mezger, K. (2018) Evidence for evolved Hadean crust from Sr isotopes in apatite within Eoarchean zircon from the Acasta Gneiss Complex. *Geochimica et Cosmochimica Acta* 235, 450-462.

Foley, S.F., Jackson, S.E., Fryer, B.J., Greenough, J.D., Jenner, G.A. (1996). Trace element partition coefficients for clinopyroxene and phlogopite in an alkaline lamprophyre from Newfoundland by LAM-ICP-MS. *Geochimica et Cosmochimica Acta* 60, 629-638.

Forsythe, L.M., Nielsen, R.L., Fisk, M.R. (1994) High-Field-Strength Element Partitioning between Pyroxene and Basaltic to Dacitic Magmas. *Chemical Geology* 117, 107-125.

Fujimaki, H., Tatsumoto, M., Aoki, K.-i. (1984) Partition coefficients of Hf, Zr, and REE between phenocrysts and groundmasses. *Journal of Geophysical Research* 89, 662-672.

Ghosh, J.G. (2004) 3.5 Ga tonalite in the central part of the Bastar craton, India: oldest Indian date. *Journal of Asian Earth Sciences* 23, 359-364.

Green, T.H., Sie, S.H., Ryan, C.G., Cousens, D.R. (1989) Proton microprobe-determined partitioning of Nb, Ta, Zr, Sr and Y between garnet, clinopyroxene and basaltic magma at high pressure and temperature. *Chemical Geology* 74: 201-216.

Green, T.H., Adam, J., Site, S.H. (1993) Proton microprobe determined trace element partition coefficients between pargasite, augite and silicate or carbonatitic melts. *EOS, Transactions of the American Geophysical Union* 74, 340.

Grove, T.L., Parman, S.W., Bowring, S.A., Price, R.C., Baker, M.B. (2002 The role of an H_2O-rich fluid component in the generation of primitive basaltic andesites and andesites from the Mt. Shasta region, N. California. *Contributions to Mineralogy and Petrology* 142, 375-396.

Harlow, G.E. (1994) Jadeitites, albitites and related rocks from the Motagua Fault Zone, Guatemala. *Journal of Metamorphic Geology* 12, 49-68.

Hart, S.R., Dunn, T. (1993) Experimental cpx/melt partitioning of 24 trace elements. *Contributions to Mineralogy and Petrology* 113: 1-8.

Hauri, E.H., Wagner, T.P., Grove, T.L. (1994) Experimental and natural partitioning of Th, U, Pb and other trace elements between garnet, clinopyroxene and basaltic melts. *Chemical Geology* 117: 149-166.

Hemming, N.G., Hanson, G.N. (1994) A procedure for the isotopic analysis of boron by negative thermal ionization mass spectrometry. *Chemical Geology* 114, 147-156.

Hervig, R.L., Moore, G.M., Williams, L.B., Peacock, S.M., Holloway, J.R., Roggensack, K., (2002) Isotopic and elemental partitioning of boron between hydrous fluid and silicate melt. *American Mineralogist* 87, 769-774.

Hofmann, A.W. (1988) Chemical differentiation of the Earth: the relationship between mantle, continental crust, and oceanic crust. *Earth and Planetary Science Letters* 90, 297-314.

Iizuka, T., Horie, K., Moniya, T., Maruyama, S., Hirata, T., Hidaka, H., Windley, B.F. (2006) 4.2 Ga zircon xenocryst in an Acasta gneiss from northwestern Canada: Evidence for early continental crust. *Geology* 34, 245-248.

Jackson, S.E., Pearson, N.J., Griffin, W.L., Belousova, E.A. (2004) The application of laser ablation-inductively coupled plasma-mass spectrometry to in situ U–Pb zircon

geochronology. *Chemical Geology* 211, 47-69.

Jenner, G.A., Foley, S.F., Jackson, S.E., Green, T.H., Fryer, B.J., Longerich, H.P. (1994) Determination of partition coefficients for trace elements in high pressure-temperature experimental run products by laser ablation microprobe-inductively coupled plasma-mass spectrometry (LAM-ICP-MS). *Geochimica et Cosmochimica Acta* 57, 5099-5103.

Johnson, K.T.M., Kinzler, R.J. (1989) Partitioning of REE, Ti, Zr, Hf, and Nb between clinopyroxene and basaltic liquid: an ion microprobe study. *EOS, Transactions of the American Geophysical Union* 70, 1388.

Johnson, K.T.M. (1994) Experimental cpx/ and garnet/melt partitioning of REE and other trace elements at high pressures; petrogenetic implications. *Mineralogical Magazine* 58, 454-455.

Johnson, K.T.M. (1998) Experimental determination of partition coefficients for rare earth and high-field-strength elements between clinopyroxene, garnet, and basaltic melt at high pressures. *Contributions to Mineralogy and Petrology* 133, 60-68.

Johnson, T.E., Brown, M., Gardiner, N.J., Kirkland, C.L., Smithies, R.H. (2017) Earth's first stable continents did not form by subduction. *Nature* 543, 239-242.

Kamber, B.S., Collerson, K.D., Moorbath, S., Whitehouse, M.J. (2003) Inheritance of early Archaean Pb-isotope variability from long-lived Hadean protocrust. *Contributions to Mineralogy and Petrology* 145, 25-46.

Kamber, B.S., Whitehouse, M.J., Bolhar, R., Moorbath, S. (2005) Volcanic resurfacing and the early terrestrial crust: zircon U–Pb and REE constraints from the Isua Greenstone Belt, southern West Greenland. *Earth and Planetary Science Letters* 240, 276–290.

Kasemann, S., Erzinger, J., Franz, G. (2000) Boron recycling in the continental crust of the central Andes from the Paleozoic to Mesozoic, NW Argentina. *Contributions to Mineralogy and Petrology* 140, 328–343

Kato, T., Ringwood, A.E., Irifune, T. (1988) Experimental-Determination of Element Partitioning between Silicate Pervoskites, Garnets and Liquids - Constraints on Early Differentiation of the Mantle. *Earth and Planetary Science Letters* 89, 123-145.

Kelemen, P.B., Dunn, J.T. (1992) Depletion of Nb relative to other highly incompatible elements by melt/rock reaction in the upper mantle. *EOS, Transactions of the American Geophysical Union* 73, 656-657.

Kisters, A.F.M., van Hinsberg, V.J., Szilas, K. (2012) Geology of an Archaean accretionary complex - The structural record of burial and return flow in the Tartoq Group of South West Greenland. *Precambrian Research* 220, 107-122.

Klein, M., Stosch, H.G., Seck, H.A. (1997) Partitioning of high field-strength and rare-earth elements between amphibole and quartz-dioritic to tonalitic melts: An experimental study. *Chemical Geology* 138, 257-271.

Kleinhanns, I.C.K.K., Kamber, B.S., Meisel, T., Combined chemical separation of Lu, Hf, Sm, Nd, and REEs from a single rock digest: precise and accurate isotope determinations of Lu-Hf and Sm-Nd using multicollector-ICPMS. *Analytical Chemistry* 74, 67-73.

Konrad-Schmolke, M., Halama, R. (2014) Combined thermodynamic–geochemical modeling in metamorphic geology: Boron as tracer of fluid–rock interaction. *Lithos* 208-209, 393-414.

Konrad-Schmolke, M., Halama, R., Manea, V. (2016) Slab mantle dehydrates beneath Kamchatka: yet recycles water into the deep mantle. *Geochemistry Geophysics Geosystems* 17, 2987-3007.

Kooijman, E., Berndt, J., Mezger, K. (2012) U-Pb dating of zircon by laser ablation ICP-MS: recent improvements and new insights. *European Journal of Mineralogy* 24, 15-21.

Kowalski, P.M., Wunder., B (2018) Boron Isotope Fractionation Among Vapor–Liquids–Solids–Melts: Experiments and Atomistic Modeling. In: Marschall, H.R., Foster, G.L. (Eds.) *Boron Isotopes – The Fifth Element, Advances in Isotope Geochemistry 6*. Springer, Heidelberg, 33-69.

Latourrette, T., Hervig, R.L., Holloway, J.R. (1995) Trace-element partitioning between amphibole, phlogopite, and basanite Melt. *Earth and Planetary Science Letters* 135, 13-30.

Leeman, W.P., Sisson, V.B., Reid, M.R. (1992) Boron geochemistry of the lower crust: Evidence from granulite terranes and deep crustal xenoliths. *Geochimica et Cosmochimica Acta* 56, 775-788.

Leeman, W.P., Tonarini, S., Chan, L.H., Borg, L.E. (2004) Boron and lithium isotopic variations in a hot subduction zone—the southern Washington Cascades. *Chemical Geology* 212, 101-124.

Lemarchand, D., Jeambrun, M., van Bergen, M.J., van Cappellen, P. (2009) Boron isotopes in Archean cherts: investigating early Earth marine conditions. *AGU Fall Meeting, San Francisco* Abs.: PP11C-1335.

Le Voyer, M., Rose-Koga, E.F., Shimizu, N., Grove, T.L., Schiano, P. (2010) Two Contrasting H_2O-rich Components in Primary Melt Inclusions from Mount Shasta. *Journal of Petrology* 51, 1571-1595.

Ludwig, K.R. (2003) ISOPLOT; a plotting and regression program for radiogenic-isotope data, version 3.27, Berkeley *Geochronology Center Open-File* Report nr. 91-445.

Makashima, A., Nakamura, E., Nakano, T. (1997) Determination of boron in silicate samples by direct aspiration of sample HF solutions into ICPMS. *Analytical Chemistry* 69, 3754-3759.

Maltese, A., Mezger, K., Upadhyay, D. (2017) Relics of pristine Paleoarchean continental crust: granitoids from the Bastar Craton, India. *Goldschmidt Abstracts* 2017, 2548.

Marschall, H.R. (2018) Boron isotopes in the ocean floor realm and the mantle. In: Marschall, H.R., Foster, G.L. (Eds.) *Boron Isotopes – The Fifth Element, Advances in Isotope Geochemistry 6*. Springer, Heidelberg, 189-215.

Marschall, H.R., Wanless, V.D., Shimizu, N., Pogge von Strandmann, P.A.E., Elliott, T., Monteleone, B.D. (2017) The boron and lithium isotopic composition of mid-ocean ridge basalts and the mantle. *Geochimica et Cosmochimica Acta* 207, 102–138.

Martin, C., Emmanuel, P., Harlow, G.E., In situ lithium and boron isotope determinations in mica, pyroxene, and serpentine by LA-MC-ICP-MS. *Chemical Geology* 412, 107-116.

Martin, C., Flores, K.E., Harlow, G.E. (2016) Boron isotopic discrimination for subduction-related serpentinites. *Geology* 44, 899-902.

Martin, H., Smithies, R.H., Rapp, R.P., Moyen, J.-F., Champion, D. (2005) An overview of adakite, tonalite trondhjemite granodiorite (TTG), and sanukitoid: relationships and some implications for crustal evolution. *Lithos* 79, 1-24.

McKenzie, D., O'Nions, R.K. (1991) Partial melt distributions from inversion of rare Earth element concentrations. *Journal of Petrology* 32, 1021-1091.

Meisel, T., Moser, J., Fellmer, N., Wegscheider, W., Schoenberg, R. (2001) Simplified method for the determination of Ru, Pd, Re, Os, Ir and Pt in chromitites and other geological materials by isotope dilution ICP-MS and acid digestion. *The Analyst* 126, 322-328.

Mohan, M.R., Kamber, B.S., Piercey, S.J. (2008) Boron and arsenic in highly evolved Archean felsic rocks: Implications for Archean subduction processes. *Earth and Planetary Science Letters* 274, 479-488.

Moorbath, S., O'Nions, R.K., Pankhurst, R.J. (1973) Early Archaean age for the Isua Iron Formation, West Greenland. *Nature* 245, 138-139.

Moyen, J.-F. (2011) The composite Archaean grey gneisses: Petrological significance, and evidence for a non-unique tectonic setting for Archaean crustal growth. *Lithos* 123, 21-36.

Moyen, J.-F., Martin, H. (2012) Forty years of TTG research. *Lithos* 148, 312-336.

Naqvi, S.M. (2005) *Geology and Evolution of the Indian Plate*. Capital Publishing Company, New Delhi.

Nutman, A.P., Kalsbeek, F.A. (1994) A minimum age of 2944 ± 7 Ma for the Tartoq Group, South-West Greenland. *Rapport - Grønlands Geologiske Undersøgelse* 161, 35-38.

Nutman A.P., McGregor, V.R., Friend, C.R.L., Bennett, V.C., Kinny, P.D. (1996) The Itsaq Gneiss Complex of southern West Greenland: The world's most extensive record of early crustal evolution (3900-3600 Ma). *Precambrian Research* 78, 1-39.

Nutman, A.P., Friend, C.R.L., Horie, K., Hidaka, H. (2007) The Itsaq Gneiss Complex of Southern West Greenland and the construction of Eoarchaean crust at convergent plate boundaries. In: van Kranendonk, M., Smithies R.H., Bennett, V.C. (Eds.) *Earth's oldest rocks*. Elsevier, Amsterdam, 187-218.

Næraa, T., Scherstén, A., Rosing, M.T., Kemp, A.I.S., Hoffmann, J.E., Kokfelt, T.F., Whitehouse, M.J. (2012) Hafnium isotope evidence for a transition in the dynamics of continental growth 3.2 Gyr ago. *Nature* 485, 627-630.

Oberti, R., Vannucci, R., Zanetti, A., Tiepolo, M., Brumm, R. (2000) A crystal chemical re-evaluation of amphibole/clinopyroxene D_{Ti} values in pertogenetic studies. *American Mineralogist* 85, 407-419.

Okamoto, K. (1979) Geochemical study on magmatic differentiation of Asama Volcano, central Japan. *Journal of the Geological Society of Japan* 85, 525-535.

Pabst, S., Zack, T., Savov, I.P., Ludwig, T., Rost, D., Tonarini, S., Vicenzi, E. P. (2012) The fate of subducted oceanic slabs in the shallow mantle: Insights from boron isotopes and light element composition of metasomatized blueschists from the Mariana forearc. *Lithos* 132-133, 162-179.

Paces, J.B., Miller, J.D., Precise U-Pb ages of Duluth Complex and related mafic intrusions, northeastern Minnesota: Geochronological insights to physical, petrogenetic, paleomagnetic, and tectonomagmatic processes associated with the 1.1 Ga Midcontinent Rift System. *Journal of Geophysical Research* 98, 13997–14013.

Piercey, S.J., Chaloux, E.C., Péloquin, A.S., Hamilton, M.A., Creaser, R.A. (2008) Synvolcanic and younger plutonic rocks from the Blake River Group: implications for regional metallogenesis. *Economic Geology* 103, 1243-1268.

Polat, A., Wang, L., Appel, P.W.U. (2015) A review of structural patterns and melting processes in the Archean craton of West Greenland: Evidence for crustal growth at convergent plate margins as opposed to non-uniformitarian models. *Tectonophysics* 662, 67-94.

Polat, A., Kokfelt, T.F., Burke, K.C., Kusky, T.M., Bradley, D.C., Dziggel, A., Kolb, J. (2016) Lithological, structural, and geochemical characteristics of the Mesoarchean Tårtoq greenstone belt, southern West Greenland, and the Chugach – Prince William accretionary complex, southern Alaska: evidence for uniformitarian plate-tectonic processes. *Canadian Journal of Earth Sciences* 53, 1336-1371.

Putnis, A., John, T. (2010) Replacement processes in the Earth's crust. *Elements* 6, 159-164.

Rajesh, H.M., Mukhopadhyay, J., Beukes, N.J., Gutzmer, J., Belyanin, G.A., Armstrong, R.A., Evidence for an early Archaean granite from Bastar craton, India. *Journal of the Geological Society, London* 166, 193-196.

Ramakrishnan M. (1990) Crustal Development in Southern Bastar, Central Indian Craton. *Geological Survey of India Special Publications* 28, 44-66.

Reimink, J.R., Chacko, T., Stern, R.A., Heaman, L. (2014) Earth's earliest evolved crust generated in an Iceland-like setting. *Nature Geoscience* 7, 529-533.

Ronov, A.B., Yaroshevskiy, A.A. (1976) A new model for the chemical structure of the Earth's crust. *Geochemistry International* 13, 89-121.

Rose, E.F., Shimizu, N., Layne, G.D., Grove, T.L. (2001) Melt production beneath Mt. Shasta from boron data in primitive melt inclusions. *Science* 293, 281-283.

Rosner, M., Meixner, A. (2004) Boron isotopic composition and concentration of ten geological reference materials. *Geostandandards and Geoanalytical Research* 28, 431-441.

Ryan, J.G., Langmuir, C.H. (1993) The systematics of boron abundances in young volcanic rocks. *Geochimica et Cosmochimica Acta* 57, 1489-1498.

Salters, V. and Longhi, J. (1999) Trace element partitioning during the initial stages of melting beneath mid-ocean ridges. *Earth and Planetary Science Letters* 166, 15-30.

Sarkar, G., Corfu, F., Paul, D.K., McNaughton, N.J., Gupta, S.N., Bishui, P.K. (1993) Archaean crust in Bastar craton, central India—a geochemical and isotopic study. *Precambrian Research* 62, 127-137.

Sharma, R.S. (2009) Cratons and Fold Belts of India. *Lecture Notes in Earth Sciences* 127, 41-115.

Sisson, T.W. (1994) Hornblende-Melt Trace-Element Partitioning Measured by Ion Microprobe. *Chemical Geology* 117, 331-344.

Smithies, R.H. (2000) The Archaean tonalite–trondhjemite–granodiorite (TTG) series is not an analogue of Cenozoic adakite. *Earth and Planetary Science Letters* 182, 115-125.

Sobolev, A.V., Asafov, E.V., Gurenko, A.A., Arndt, N.T., Batanova, V.G., Portnyagin, M.V., Garbe-Schönberg, D., Krasheninnikov, S.P. (2016) Komatiites reveal a hydrous Archaean deep-mantle reservoir. *Nature* 531, 628-632.

Sprung, P., Scherer, E.E., Maltese, A., Bast, R., Bleeker, W., Mezger, K. (2016) The Acasta Gneiss - a Hadean cratonic nucleus. *AGU Fall Meeting Abstracts*, V11D-08.

Stacey, J.S., Kramers, J.D. (1975) Approximation of terrestrial lead isotope evolution by a two-stage model. *Earth and Planetary Science Letters* 26, 207–221.

Stern, R.A., Bleeker, W. (1998) Age of the world's oldest rocks refined using Canada's SHRIMP: The Acasta Gneiss Complex, Northwest Territories, Canada. *Geoscience Canada* 25, 27-31.

Sylvester, P., Ghaderi, M. (1997) Trace element analysis of scheelite by excimer laser ablation-inductively coupled plasma-mass spectrometry (ELA-ICP-MS) using a synthetic silicate glass standard. *Chemical Geology* 141, 49-65.

Syracuse, E.M., van Keken, P.E., Abers, G.A. (2010) The global range of subduction zone thermal models. *Physics of Earth and Planetary Interiors* 183, 73-90.

Szilas, K., van Hinsberg, V.J., Kisters, A.F.M., Hoffmann, J.E., Windley, B.F., Kokfelt, T.F., Scherstén, A., Frei, R., Rosing, M.T., Münker, C. (2013) Remnants of arc-related Mesoarchaean oceanic crust in the Tartoq Group of SW Greenland. *Gondwana Research* 23, 436-451.

Tonarini, S., Forte, C., Petrini, R., Ferrara, G. (2003) Melt/biotite $^{11}B/^{10}B$ isotopic fractionation and the boron local environment in the structure of volcanic glasses. *Geochimica et Cosmochimica Acta* 67, 1863-1873.

Tonarini, S., Leeman, W.P., Leat, P.T. (2011). Subduction erosion of forearc mantle wedge implicated in the genesis ofo the South Sandwich Island (SSI) arc: evidence from boron isotope systematics. *Earth and Planetary Science Letters* 301, pp. 275-284.

Vannucci, R., Bottazzi, P., Wulff-Pedersen, E., Neumann, E. (1998) Partitioning of REE, Y, Sr, Zr and Ti between clinopyroxene and silicate melts in the mantle under La Palma (Canary Islands): implications for the nature of the metasomatic agents. *Earth and Planetary Science Letters* 158, 39-51.

Villemant, B. (1988) Trace-Element Evolution in the Phlegrean Fields (Central-Italy) - Fractional Crystallization and Selective Enrichment. *Contributions to Mineralogy and Petrology* 98, 169-183.

Walowski, K.J., Wallaca, P.J., Hauri, E.H., Clynne, M.A. (2015) Slab melting beneath the Cascade Arc driven by dehydration of altered oceanic peridotite. *Nature Geoscience* 8, 404-408.

Weyer, S., Münker, C., Rehkämper, M., Mezger, K. (2002) Determination of ultra-low Nb, Ta, Zr and Hf concentrations and the chondritic Zr/Hf and Nb/Ta ratios by

isotope dilution analyses with multiple collector ICP-MS. *Chemical Geology* 187, 295-313.

Whitehouse, M.J., Kamber, B.S., Moorbath, S. (1999) Age significance of U–Th–Pb zircon data from early Archaean rocks of west Greenland—a reassessment based on combined ion-microprobe and imaging studies. *Chemical Geology* 160, 201-224.

Windley, B.F., Garde, A.A. (2009) Arc-generated blocks with crustal sections in the North Atlantic craton of West Greenland: crustal growth in the Archean with modern analogues. *Earth Science Reviews* 93, 1-30.